FERMILAB-
FN-0744

COUPLING IMPEDANCES OF LAMINATED MAGNETS

K.Y. Ng

Fermi National Accelerator Laboratory, P.O. Box 500, Batavia, IL 60510*

(April, 2004)

Abstract

Coupling impedances, both longitudinal and transverse, are derived for a beam exposed to the laminations of magnets. The method consists of first deriving the impedances in terms of the surface impedance per square, which is defined as the ratio of the longitudinal electric field and the transverse magnetic field at the laminated pole surfaces, and second deriving the surface impedance per square according to the configuration of the laminations. A combined-function magnet is approximated by laminations having two parallel faces. A Lambertson magnet is approximated by an annular ring of laminations. Instead of diverging to infinity at zero frequency, the existence of the bypass inductance for a dipole particle beam requires the real part of the transverse impedance to bend around and go to zero instead, so that laminated magnet will drive head-tail instabilities at nonzero chromaticity but not transverse coupled-bunch instabilities. Applications are made to the laminated magnets of the Fermilab Booster and the Lambertson magnets of the Fermilab Tevatron and Main Injector.

*Operated by the Universities Research Association, Inc., under contract with the U.S. Department of Energy.

Contents

1 INTRODUCTION **1**

2 RESISTIVE WALL IMPEDANCE **3**

2.1 PARALLEL PLATES 3

2.1.1 ON-CENTER BEAM 3

2.1.2 IMAGE CHARGES AND CURRENT DENSITIES 12

2.1.3 OFFSET BEAM 13

2.1.4 IMPEDANCES OF CENTERED BEAM 15

2.1.5 EFFECTIVE SURFACE IMPEDANCES PER SQUARE 22

2.2 CYLINDRICAL BEAM PIPE 23

2.2.1 ON-AXIS BEAM 23

2.2.2 BYPASS INDUCTANCE 30

2.2.3 OFF-AXIS BEAM 37

3 CRACK IMPEDANCE **40**

3.1 PARALLEL-FACE MAGNET 40

3.1.1 LOW-FREQUENCY BEHAVIOR 46

3.1.2 HIGH-FREQUENCY BEHAVIOR 47

3.1.3 LAMINATIONS VERSUS CRACKS 47

3.2 ANNULAR-RING MAGNET 49

3.2.1 LOW-FREQUENCY BEHAVIOR 51

3.2.2 HIGH-FREQUENCY BEHAVIOR 52

4 APPLICATIONS **53**

4.1 FERMILAB BOOSTER 53

4.1.1 Microwave Instability 55

4.1.2 Transverse Coupled-Bunch Instabilities 56

4.1.3 Transverse Head-Tail Instabilities 59

4.2 FERMILAB TEVATRON 66

4.2.1 Lambertson Magnets 66

4.2.2 Transverse Head-Tail Instabilities 70

4.2.3 Measurements by Invanov, Burov, and Tan 72

4.3 FERMILAB MAIN INJECTOR 76

5 CONCLUSIONS **80**

1 INTRODUCTION

A beam exposed to metallic laminations entails tremendous coupling impedances, both longitudinal and transverse. The laminated elements can be Lambertson magnets or parallel-face dipoles. The beam can be at the central axis of the magnet or at an offset close to the laminated surfaces of the magnets. The coupling impedances can be derived in two steps. [1] First, the resistive-wall impedances are derived assuming an effective surface impedance per square $\mathcal{R}$ of the laminated surface, defined as the ratio of the electric field component in the direction of the beam and the magnetic field transverse to the beam at the surface. For a resistive metallic beam pipe, this surface impedance per square is just†

$$\mathcal{R} = \frac{1+j}{\delta_c \sigma_c} \ , \tag{1.1}$$

where σ_c is the conductivity of the beam pipe and

$$\delta_c = \sqrt{\frac{2}{|\omega| \mu \sigma_c}} \tag{1.2}$$

is the corresponding skin-depth into the walls of the beam pipe at the angular frequency ω with μ being the magnetic permeability. The second step is to compute the effective surface impedance per square of a laminated magnet by including the effect of the electromagnetic waves going into and out of the cracks of the laminations.

It has been pointed out that the transverse dipole impedance $Z_1^\perp$ does not follow the $\omega^{-1/2}$ behavior at low frequencies. [2] In fact, the dipole image current sees a *bypass inductance* $Z_0/(4\pi c)$ in parallel with the resistive-wall impedance, where $Z_0 \approx 377\ \Omega$ is the impedance of free space and c is the velocity of light. [3] Thus, when the frequency is low enough, the image current will flow through the bypass inductance instead. In other words, $\mathcal{I}m\, Z_1^\perp$ approaches a constant inductive reactance at zero frequency, while $\mathcal{R}e\, Z_1^\perp$ bends around and goes to zero linearly. As a result, the bend-around frequency is determined roughly by the equality of the bypass inductive reactance and the wall impedance, or

$$\frac{\omega Z_0}{4\pi c} \approx \frac{|\mathcal{R}|}{2\pi b} \ , \tag{1.3}$$

which reduces to

$$\frac{\sqrt{2} b}{\delta_c} \sim 1 \ , \tag{1.4}$$

†When both positive and negative frequencies are addressed, $1+j$ should be replaced by $1 + j\,\mathrm{sgn}(\omega)$. However, or the sake of convenience, sgn(*omega*) is omitted most of the time in below.

for a cylindrical beam pipe of radius b with smooth resistive wall. Or the bend-around frequency is

$$f_{\rm bend} = \frac{c}{2\pi Z_0 \sigma_c \mu_r b^2} \ . \tag{1.5}$$

With a beam pipe of radius $b = 5$ cm, wall conductivity $\sigma_c = 0.5 \times 10^7$ $(\Omega\text{-m})^{-1}$, and relative magnetic permeability $\mu_r \sim 1$, the bend-around frequency is roughly 10 Hz, which is very much less than the revolution frequency for nearly all accelerator rings. As a result, this bend-around of $\mathcal{R}e\, Z_1^\perp$ plays no role in the discussion of collective instabilities of the particle beam. For a laminated magnet, however, the surface impedance per square is very much larger, and the bend-around frequency becomes much larger. The bend-around frequency of a laminated magnet of annular cross-section is estimated to be roughly

$$f_{\rm bend} = \frac{8c\mu_r}{Z_0 \sigma_c \tau} \left(\ln \frac{d}{b} \right)^2 \ , \tag{1.6}$$

where b and d are, respectively, the inner and outer radii of the magnet, τ is the thickness of a lamination with relative magnetic permeability μ_r and skin-depth δ_c. As an example, with $\tau = 0.025''$, and $\mu_r = 100$ for the lamination, and $b = 1.25''$ and $d = 6''$ for the radii, the bend-around frequency becomes $\sim$ 250 MHz (actual computation gives $\sim$ 100 MHz). The implication is that the laminated magnets do not contribute to the $\omega^{-1/2}$ behavior of the transverse impedance at low frequencies. In other words, laminated magnets will not drive transverse coupled-bunch instabilities. However, the broad peak of $\mathcal{R}e\, Z_1^\perp$ at 100 to 200 MHz does drive head-tail instabilities at nonzero chromaticities.

This paper is organized as follows. In Sec. 2, the longitudinal and transverse impedances of a beam in a parallel-face laminated magnet or annular laminated magnet are derived. The physical concept behind bypass inductance is studied in detail. The bend-around frequency as given by Eq. (1.3) or Eq. (1.4) is derived. In Sec. 3, the impedance of the cracks in the laminated magnet is derived, and the effective surface impedance per square of a laminated magnet as seen by a particle beam is given for both the parallel-face cross-section and annular cross-section. The bend-around frequency for a laminated magnet wall as given by Eq. (1.6) is derived. Applications are made in Sec. 5 for the Fermilab Booster, Tevatron, and Main Injector. Their wall impedances are computed, and their nonzero chromaticity head-tail instabilities are discussed. Finally, conclusions are given in Sec. 6. Some of the derivations and formulas in this paper are not original. They are included here for comparison and for the sake of completeness.

2 RESISTIVE WALL IMPEDANCE

In this section, we are going to solve the Maxwell's equations for a particle beam first traveling between two infinite parallel plates and later inside a cylindrical beam pipe. The resistivity of the walls give rise to the longitudinal and transverse coupling impedances experienced by the beam. Special attention is given to the behavior of the impedances at low frequencies. For the sake of simplicity, the thickness of plates or the walls of the beam pipe is considered to be infinite throughout this paper.

2.1 PARALLEL PLATES

2.1.1 ON-CENTER BEAM

Let us consider a beam flowing in the z-direction between two infinite plates $y = \pm b$, as illustrated in Fig. 1. The charge density is

$$\rho(x, y, z, t) = \rho_1 \sigma(x) e^{j(\omega t - kz)} \delta(y) \ , \tag{2.1}$$

where $\sigma(x) = \sigma(-x)$, ρ_1 is the linear charge density, and

$$\int_{-\infty}^{\infty} \sigma(x) dx = 1 \ . \tag{2.2}$$

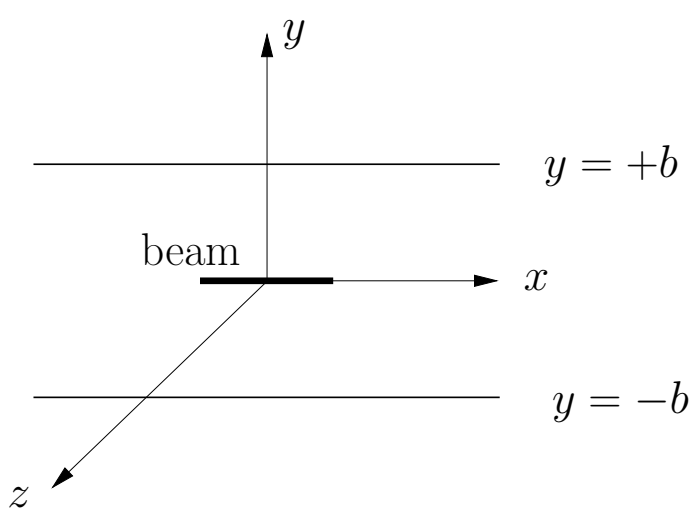

Figure 1: The two parallel plates are at $y = \pm b$. The beam at $y = 0$, flowing in the z-direction, has a horizontal distribution $\sigma(x)$, but has no vertical spread.

The current density of the beam is

$$\vec{J}(x,y,z,t) = \rho(x,y,z,t)\beta c = \hat{z}\rho_1\sigma(x)\beta c e^{j(\omega t - kz)}\delta(y) \ , \tag{2.3}$$

where $\beta c = \omega/k$ is the beam velocity. The total current is given by

$$I(z,t) = \int J_z(x,y,z,t)dxdy = \rho_1\beta c e^{j(\omega t - kz)} \ . \tag{2.4}$$

For convenience, the factor $e^{j(\omega t - kz)}$ will be omitted in below most of the time. The horizontal beam distribution can be Fourier analyzed according to

$$\sigma(x) = \int_{-\infty}^{\infty} \tilde{\sigma}_\eta \cos \eta x d\eta \ , \tag{2.5}$$

and we can always work with one of the Fourier component $\tilde{\sigma}_\eta$ and recover the whole beam at the end by superposition.

In the absence of source, the longitudinal electric E_z and magnetic field H_z satisfy the Laplace equation, which after taking into account of the z and t dependency in Eq. (2.1),

$$\left(\nabla_\perp^2 - q^2\right)\begin{pmatrix} E_z \\ H_z \end{pmatrix} = 0 \ , \tag{2.6}$$

where

$$q^2 = k^2 - \frac{\omega^2}{c^2} = k^2(1-\beta^2) \ . \tag{2.7}$$

The transverse fields can be determined from the longitudinal fields via

$$\begin{aligned} E_x &= \frac{jk}{q^2}\left(\beta\frac{\partial Z_0 H_z}{\partial y} + \frac{\partial E_z}{\partial x}\right) \ , \\ E_y &= \frac{jk}{q^2}\left(-\beta\frac{\partial Z_0 H_z}{\partial x} + \frac{\partial E_z}{\partial y}\right) \ , \\ Z_0 H_x &= \frac{jk}{q^2}\left(-\beta\frac{\partial E_z}{\partial y} + \frac{\partial Z_0 H_z}{\partial x}\right) \ , \\ Z_0 H_y &= \frac{jk}{q^2}\left(\beta\frac{\partial E_z}{\partial x} + \frac{\partial Z_0 H_z}{\partial y}\right) \ , \end{aligned} \tag{2.8}$$

where $Z_0 = \sqrt{\mu_0/\epsilon_0}$ is the free-space impedance, with μ_0 and ϵ_0 denoting, respectively, the magnetic permeability and electric permittivity of vacuum.

Notice that in the limit $\beta \to 1$, $q \to 0$. The transverse fields can no longer be derived via Eq. (2.8). However, the limit of $\beta \to 1$ does simplify the problem, because Eq. (2.8)

indicates that E_z and H_z are no longer independent as $q \to 0$. Let us start from the Maxwell's equations and write the field components in terms of Fourier transforms,

$$\begin{cases} \big(E_z,\ E_y,\ H_x\big) = \displaystyle\int_{-\infty}^{\infty} d\eta\, \cos\eta x \big(\tilde{E}_z,\ \tilde{E}_y,\ \tilde{H}_x\big)\ , \\ \big(H_z,\ H_y,\ E_x\big) = \displaystyle\int_{-\infty}^{\infty} d\eta\, \sin\eta x \big(\tilde{H}_z,\ \tilde{H}_y,\ \tilde{E}_x\big)\ , \end{cases} \tag{2.9}$$

where the choice of $\cos\eta x$ and $\sin\eta x$ is obvious following the left-right symmetry of the beam. The Maxwell's equations are now expressed as:

$$\begin{cases} \eta\tilde{E}_x + \dfrac{\partial\tilde{E}_y}{\partial y} - jk\tilde{E}_z = \dfrac{\rho_1\tilde{\sigma}_\eta}{\epsilon_0}\,\delta(y)\ , \\ -\eta\tilde{H}_x + \dfrac{\partial\tilde{H}_y}{\partial y} - jk\tilde{H}_z = 0\ , \\ \dfrac{\partial\tilde{E}_z}{\partial y} + jk\tilde{E}_y + jkZ_0\tilde{H}_x = 0\ , \\ -jk\tilde{E}_x + \eta\tilde{E}_z + jkZ_0\tilde{H}_y = 0\ , \\ -\eta\tilde{E}_y - \dfrac{\partial\tilde{E}_x}{\partial y} + jkZ_0\tilde{H}_z = 0\ , \\ \dfrac{\partial Z_0\tilde{H}_z}{\partial y} + jkZ_0\tilde{H}_y - jk\tilde{E}_x = 0\ , \\ -jkZ_0\tilde{H}_x - \eta Z_0\tilde{H}_z - jk\tilde{E}_y = 0\ , \\ \eta Z_0\tilde{H}_y - \dfrac{\partial Z_0\tilde{H}_x}{\partial y} - jk\tilde{E}_z = Z_0\rho_1\tilde{\sigma}_\eta c\,\delta(y)\ . \end{cases} \tag{2.10}$$

In above, the first two are Gauss's laws for electric and magnetic fields, the 3rd to 6th correspond to Faraday's law, and the last three correspond to Ampere's law. From the 2nd, 3rd, 4th, and 7th lines, we get the equations for the longitudinal fields:

$$\begin{cases} \dfrac{\partial\tilde{E}_z}{\partial y} = \eta Z_0\tilde{H}_z\ , \\ \dfrac{\partial Z_0\tilde{H}_z}{\partial y} = \eta\tilde{E}_z\ . \end{cases} \tag{2.11}$$

Knowing that $\tilde{E}_z$ is symmetric in y and $\tilde{H}_y$ odd in y, we obtain immediately

$$\begin{cases} \tilde{E}_z = A_\eta \cosh\eta y\ , \\ Z_0\tilde{H}_z = A_\eta \sinh\eta y\ . \end{cases} \tag{2.12}$$

We next write the transverse fields in terms of the longitudinal fields:

$$\begin{cases} \dfrac{\partial \tilde{E}_y}{\partial y} + \eta Z_0 \tilde{H}_y = \left(jk + \dfrac{j\eta^2}{k} \right) \tilde{E}_z + \dfrac{\rho_1 \tilde{\sigma}_\eta}{\epsilon_0} \, \delta(y) \ , \\ \dfrac{\partial Z_0 \tilde{H}_y}{\partial y} + \eta \tilde{E}_y = \left(jk + \dfrac{j\eta^2}{k} \right) Z_0 \tilde{H}_z \ , \\ \tilde{E}_x = Z_0 \tilde{H}_y - \dfrac{j\eta}{k} \tilde{E}_z \ , \\ Z_0 \tilde{H}_x = -\tilde{E}_y + \dfrac{j\eta}{k} Z_0 \tilde{H}_z \ . \end{cases} \tag{2.13}$$

Obviously, the transverse fields must be $\cosh \eta y$ and/or $\sinh \eta y$, leading to the solution,

$$\begin{cases} \tilde{E}_y = \left[\dfrac{j}{2} \left(\dfrac{k}{\eta} + \dfrac{\eta}{k} \right) A_\eta + B_\eta \right] \sinh \eta y \pm \dfrac{\rho_1 \tilde{\sigma}_\eta}{2\epsilon_0} \cosh \eta y \ , \\ Z_0 \tilde{H}_y = \left[\dfrac{j}{2} \left(\dfrac{k}{\eta} + \dfrac{\eta}{k} \right) A_\eta - B_\eta \right] \cosh \eta y \mp \dfrac{\rho_1 \tilde{\sigma}_\eta}{2\epsilon_0} \sinh \eta y \ , \end{cases} \tag{2.14}$$

Some comments are in order. The first two lines of Eq. (2.13) are redundant giving only the sum of the coefficients of $\tilde{E}_y$ and $Z_0 \tilde{H}_y$. Thus another constant B_η has been inserted into Eq. (2.14) to account for their difference. With only the $\sinh \eta y$ term, $\tilde{E}_y$ vanishes at $y = 0$. To account for the charge of the beam, the other term $\pm \cosh \eta y$ (for $y \gtrless 0$), which is also odd in y, has been added.

Inside the metallic plates, Maxwell's equations are the same as Eq. (2.10), with the exception of having no charge and the additional current density $\vec{J} = \sigma_c \vec{E}$ inside the metallic plates, where σ_c is the conductivity. This is equivalent to transforming the electric permittivity to

$$\epsilon \to \epsilon_0 \left(\epsilon_r - \frac{\sigma_c}{j\omega\mu\epsilon_0} \right) \ , \tag{2.15}$$

where ϵ_r is the relative electric permittivity of the metal or the dielectric constant. Maxwell's

equations now take the form:

$$\begin{cases} \eta\tilde{E}_x + \dfrac{\partial\tilde{E}_y}{\partial y} - jk\tilde{E}_z = 0 \ , \\ -\eta\tilde{H}_x + \dfrac{\partial\tilde{H}_y}{\partial y} - jk\tilde{H}_z = 0 \ , \\ \dfrac{\partial\tilde{E}_z}{\partial y} + jk\tilde{E}_y + jk\mu_r Z_0\tilde{H}_x = 0 \ , \\ -jk\tilde{E}_x + \eta\tilde{E}_z + jk\mu_r Z_0\tilde{H}_y = 0 \ , \\ -\eta\tilde{E}_y - \dfrac{\partial\tilde{E}_x}{\partial y} + jk\mu_r Z_0\tilde{H}_z = 0 \ , \\ \dfrac{\partial Z_0\tilde{H}_z}{\partial y} + jkZ_0\tilde{H}_y - (jk\epsilon_r + Z_0\sigma_c)\tilde{E}_x = 0 \ , \\ -jkZ_0\tilde{H}_x - \eta Z_0\tilde{H}_z - (jk\epsilon_r + Z_0\sigma_c)\tilde{E}_y = 0 \ , \\ \eta Z_0\tilde{H}_y - \dfrac{\partial Z_0\tilde{H}_x}{\partial y} - (jk\epsilon_r + Z_0\sigma_c)\tilde{E}_z = 0 \ , \end{cases} \tag{2.16}$$

where μ_r is the relative magnetic permeability of the metal. Again we figure out the equations governing the longitudinal fields first and then express the transverse fields in terms of them. However, with the introduction of the current density inside the metallic plate, Eq. (2.7) is now transformed to

$$q^2 = k^2 - \omega\mu\epsilon \rightarrow k^2 - k^2\beta^2\mu_r\epsilon_r - jk\beta Z_0\mu_r\sigma_c = k^2 - k^2\beta^2\mu_r\epsilon_r - \lambda_c^2 \ , \tag{2.17}$$

with the introduction of

$$\lambda_c^2 = jk\beta Z_0\mu_r\sigma \ , \tag{2.18}$$

which can be expressed in terms of the skin-depth δ_c as

$$\lambda_c = \sqrt{jk\beta Z_0\mu_r\sigma_c} = \frac{1+j}{\delta_c} \ , \tag{2.19}$$

where the square root has been so chosen that that the fields decay into the metal from the surface. Since q^2 does not vanish, the longitudinal electric field and magnetic fields are no

longer related. We therefore have

$$\begin{cases} \dfrac{\partial^2 \tilde{E}_z}{\partial y^2} = \left(\eta^2 + \lambda_c^2\right)\tilde{E}_z \ , \\ \dfrac{\partial^2 \tilde{H}_z}{\partial y^2} = \left(\eta^2 + \lambda_c^2\right)\tilde{H}_z \ , \\ \quad \tilde{E}_x = \dfrac{1}{Z_0\sigma_c}\left(-\eta\tilde{E}_z + \dfrac{\partial Z_0\tilde{H}_z}{\partial y}\right) \ , \\ \quad \tilde{E}_y = \dfrac{1}{Z_0\sigma_c}\left(-\eta Z_0\tilde{H}_z + \dfrac{\partial \tilde{E}_z}{\partial y}\right) \ , \\ Z_0\tilde{H}_x = -\tilde{E}_y + \dfrac{j}{k}\dfrac{\partial \tilde{E}_z}{\partial y} \ , \\ Z_0\tilde{H}_y = \tilde{E}_x + \dfrac{j\eta}{k}\tilde{E}_z \ , \end{cases} \tag{2.20}$$

where, for simplicity, we have let $\mu_r = 1$ and $\epsilon_r = 1$. Note that the displacement current has been included in Eq. (2.16). If not, the coefficient on the right side of the first two equations in Eq. (2.20) will become $(k^2+\eta^2+\lambda_c^2)$ instead. If we denote $\lambda' = \sqrt{\lambda_c^2 + \eta^2}$, the longitudinal fields can be solved exactly, giving[‡]

$$\begin{cases} \tilde{E}_z = A_\eta \cosh \eta b \, e^{\lambda'(b\mp y)} \ , \\ \tilde{H}_z = \pm A_\eta \sinh \eta b \, e^{\lambda'(b\mp y)} \ , \end{cases} \tag{2.21}$$

where the two longitudinal components are related now because of their continuities across the plate surfaces. The transverse fields can then be solved exactly, giving

$$\begin{cases} \quad \tilde{E}_x = \dfrac{A_\eta}{Z_0\sigma}\Big(- \eta \cosh \eta b - \lambda' \sinh \eta b\Big) e^{\lambda'(b\mp y)} \ , \\ \quad \tilde{E}_y = \dfrac{A_\eta}{Z_0\sigma}\Big(\mp \lambda' \cosh \eta b \mp \eta \sinh \eta b\Big) e^{\lambda'(b\mp y)} \ , \\ Z_0\tilde{H}_x = \left[\dfrac{A_\eta}{Z_0\sigma}\Big(\pm \lambda' \cosh \eta b \pm \eta \sinh \eta b\Big) \mp \dfrac{j\lambda' A_\eta}{k}\cosh \eta b\right] e^{\lambda'(b\mp y)} \ , \\ Z_0\tilde{H}_y = \left[\dfrac{A_\eta}{Z_0\sigma}\Big(- \eta \cosh \eta b - \lambda' \sinh \eta b\Big) + \dfrac{j\eta A_\eta}{k}\cosh \eta b\right] e^{\lambda'(b\mp y)} \ . \end{cases} \tag{2.22}$$

Because of the presence of charge at the surfaces of the plates, $\tilde{E}_y$ is discontinuous. However,

[‡]If we set $\tilde{E}_z = A_\eta \cosh \eta b \, e^{\lambda_c(b\mp y)}$ and $\tilde{H}_z = \pm A_\eta \sinh \eta b \, e^{\lambda_c(b\mp y)}$, we are neglecting η^2 as compared to λ_c^2. If we set $\tilde{E}_z = A_\eta \cosh \eta y \, e^{\lambda_c(b\mp y)}$ and $\tilde{H}_z = A_\eta \sinh \eta y \, e^{\lambda_c(b\mp y)}$, we are neglecting η as compared to λ_c.

we still have the continuities of $\tilde{H}_y$ and $\tilde{H}_x$ which translate as

$$\begin{cases} \left[\frac{j}{2}\left(\frac{k}{\eta}+\frac{\eta}{k}\right)A_\eta - B_\eta\right]\cosh\eta b - \frac{\rho_1\tilde{\sigma}_\eta}{2\epsilon_0}\sinh\eta b \\ \qquad\qquad = -\frac{A_\eta}{Z_0\sigma}\Big(\eta\cosh\eta b + \lambda'\sinh\eta b\Big) + \frac{j\eta A_\eta}{k}\cosh\eta b\ , \\ -\left[\frac{j}{2}\left(\frac{k}{\eta}+\frac{\eta}{k}\right)A_\eta + B_\eta\right]\sinh\eta b - \frac{\rho_1\tilde{\sigma}_\eta}{2\epsilon_0}\cosh\eta b + \frac{j\eta A_\eta}{k}\sinh\eta b \\ \qquad\qquad = \frac{A_\eta}{Z_0\sigma}\Big(\lambda'\cosh\eta b + \eta\sinh\eta b\Big) - \frac{j\lambda' A_\eta}{k}\cosh\eta b\ . \end{cases} \tag{2.23}$$

The continuity of $\tilde{E}_x$ gives the same relation as the continuity of $\tilde{H}_x$. We can now solve for

$$A_\eta = \frac{\frac{\rho_1\tilde{\sigma}_\eta}{2\epsilon_0}\big(\coth\eta b - \tanh\eta b\big)}{j\frac{\lambda'}{k}\coth\eta b - j\left(\frac{k}{\eta}-\frac{\eta}{k}\right) - \frac{jk\lambda'}{\lambda_c^2}\big(\tanh\eta b + \coth\eta b\big) - \frac{j2k\eta}{\lambda_c^2}}\ , \tag{2.24}$$

where, as a reminder, $\lambda_c^2 = jkZ_0\sigma$. Notice that the denominator has been written in the order that each term is $\mathcal{O}(|\lambda_c|)$ smaller than its predecessor. Written in term of the surface impedance per square $\mathcal{R} = \lambda_c/\sigma_c$ first defined in Eq. (1.1) and keeping only the next order in $\mathcal{R}/Z_0$, Eq. (2.24) simplifies to

$$A_\eta = -\frac{\frac{\rho_1\tilde{\sigma}_\eta c\mathcal{R}}{2}\operatorname{sech}^2\eta b}{1 + j\frac{\mathcal{R}}{Z_0}\left(\frac{k}{\eta}-\frac{\eta}{k}\right)\tanh\eta b}\ . \tag{2.25}$$

Including all components in η, the longitudinal electric field at the beam is

$$E_z(x) = -\int_{-\infty}^{\infty} d\eta\, A_\eta\cos\eta x\ . \tag{2.26}$$

To derive the impedance, the average longitudinal electric field seen by the beam is desired. For this, we average over x, or do the integration

$$\int_{-\infty}^{\infty} dx\,\sigma(x)E_z(x) = \int_{-\infty}^{\infty} dx\int_{-\infty}^{\infty} d\eta'\tilde{\sigma}_{\eta'}\cos\eta' x E_z(x)\ . \tag{2.27}$$

Using the fact that

$$\int_{-\infty}^{\infty} dx\cos\eta x\cos\eta' x = \pi\left[\delta(\eta-\eta') + \delta(\eta+\eta')\right]\ , \tag{2.28}$$

we arrive at

$$\langle E_z(x)\rangle = -2\pi\rho_1 c\mathcal{R}\int_0^\infty d\eta\,\frac{\tilde{\sigma}_\eta^2\,\mathrm{sech}^2\eta b}{1+j\dfrac{\mathcal{R}}{Z_0}\left(\dfrac{k}{\eta}-\dfrac{\eta}{k}\right)\tanh\eta b}\ . \tag{2.29}$$

For a line beam[§] the horizontal beam distribution is $\sigma(x)=\delta(x)$ and $\tilde{\sigma}_\eta = 1/(2\pi)$. The longitudinal impedance per unit length seen by the beam with current $\rho_1 c$ is

$$\frac{Z_0^\parallel}{L} = -\frac{\langle E_z(x)\rangle}{\rho_1 c} = \frac{\mathcal{R}}{2\pi}\int_0^\infty d\eta\,\frac{\mathrm{sech}^2\eta b}{1+j\dfrac{\mathcal{R}}{Z_0}\left(\dfrac{k}{\eta}-\dfrac{\eta}{k}\right)\tanh\eta b}\ , \tag{2.30}$$

When $|\lambda_c b|\gg 1$, or when the frequency is $f\gg 10$ Hz if the plate separation is $2b=10$ cm and the plates are made of stainless steel with conductivity $\sigma_c = 0.5\times 10^7$ $(\Omega\text{-m})^{-1}$, the η/k term in the denominator of Eq. (2.30) can be neglected. The k/η term will not have any contribution unless $kb\gtrsim 100$ or $f\gtrsim 100$ GHz. Thus in all practical beam pipes with smooth pipe walls, we can write

$$\frac{Z_0^\parallel}{L} = \frac{\mathcal{R}}{2\pi b} = (1+j)\frac{1}{2\pi b\delta_c\sigma_c}\ , \tag{2.31}$$

which is exactly the same longitudinal impedance of a beam inside a cylindrical beam pipe of radius b.

When $|\lambda_c b|\ll 1$ or $f\ll 10$ Hz with the same b and σ_a, the η/k term in the denominator of Eq. (2.30) becomes important.[¶] However, the effect is not big, as is illustrated in the top plot of the impedance in Fig. 2. In the lower plot, we show $Z_0^\parallel/(kb)$, which is proportional to $Z_0^\parallel/n$, Here, we see clearly the deviation from the $(kb)^{-1/2}$-behavior at low frequencies can

[§]For a line beam at $x=0$, the averaging over x is unnecessary. We can just substitute $x=0$ and $\tilde{\sigma}_\eta = 1/(2\pi)$.

[¶]The k/η-term in the denominator is of no importance because we are not interested in very high frequencies. The η/k-term will be dominating at low frequencies. If we pick out this only term, the integrand behaves as η^{-2} which causes it to diverge. However, this procedure is incorrect because we should only take the limit $k\to 0$ after the integral is performed. For a sheet of beam extending uniformly from $x=-\infty$ to ∞, $\tilde{\sigma}_\eta\propto\delta(\eta)$, and therefore this term does not contribute at all. Let us come back to the pencil beam with $\tilde{\sigma}_\eta = 1/(2\pi)$. When k is finite, the denominator is equal to one at $\eta=0$, ensuring the convergence of integral. The integral receives most of its contribution when $\eta b\lesssim 1$ since $\mathrm{sech}^2\eta b$ is roughly equal to one when $\eta b\lesssim 1$ and decays exponentially when $\eta b\gtrsim 1$. For any finite k, $\eta b\tanh\eta b$ behaves as $(\eta b)^2$ when $\eta b\lesssim 1$ and therefore its contribution will be appreciable only when the frequency is extremely low. To see this, let us write $a^2 = jkbZ_0/\mathcal{R}$ and assume it to be real and positive for simplicity. Then

$$\int_0^\infty \frac{\mathrm{sech}^2 x\,dx}{1+\dfrac{x\tanh x}{a^2}} < \int_0^\infty \frac{\mathrm{sech}^2 x\,dx}{1+\dfrac{\tanh^2 x}{a^2}} = a\tan^{-1}\frac{1}{a}\approx\frac{\pi a}{2}\ . \tag{2.32}$$

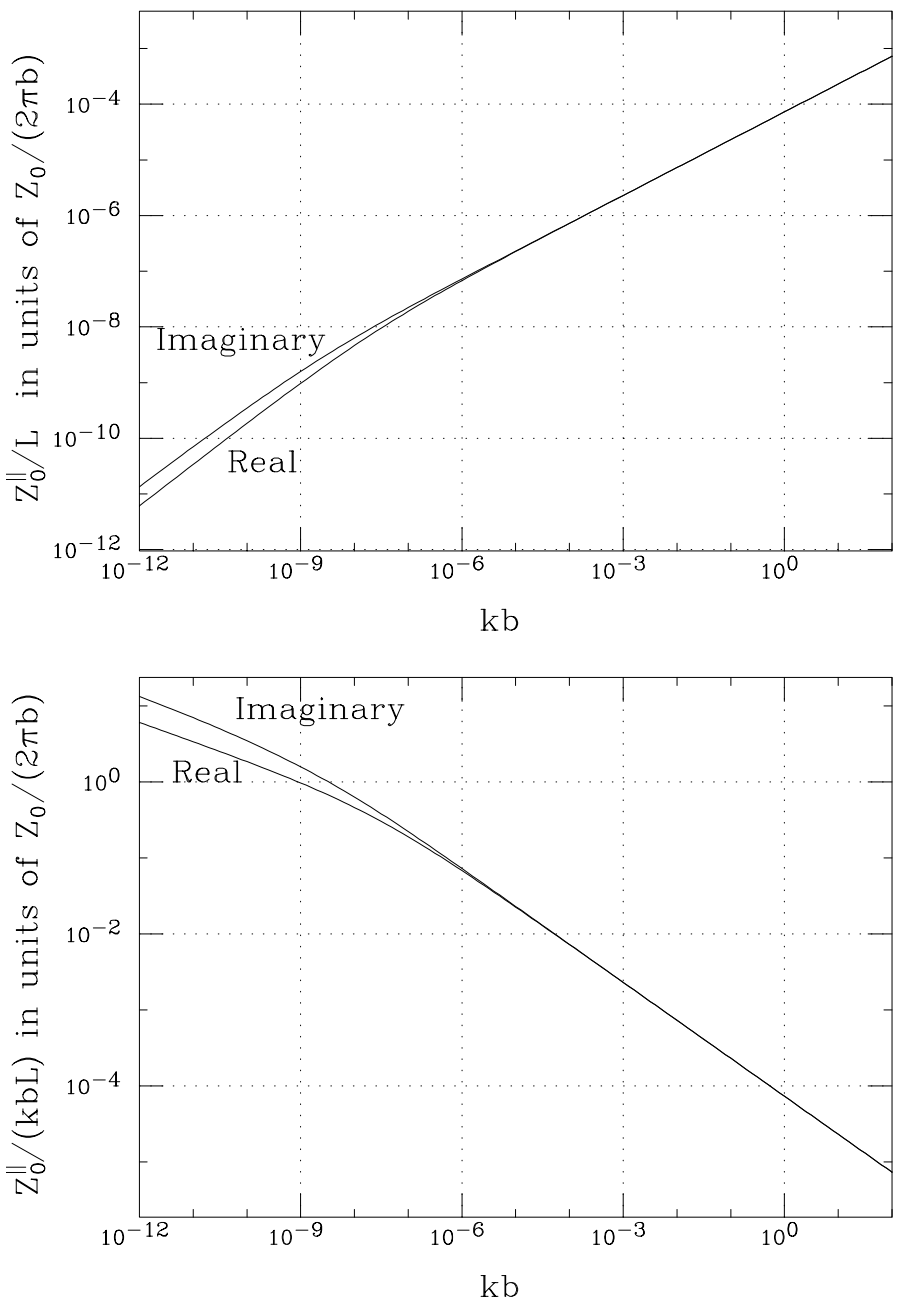

Figure 2: Top: The real and imaginary parts of the longitudinal monopole impedance are shown as functions of kb for a beam pipe with radius $b = 5$ cm and wall conductivity $\sigma_c = 0.5 \times 10^7$ $(\Omega\text{-m})^{-1}$ (stainless steel). While both parts increase with frequency as $\sqrt{kb}$. The deviations from the $\sqrt{kb}$-behavior at low frequencies can be seen. Bottom: The real and imaginary parts of the longitudinal monopole impedance divided by frequency ($\sim Z_0^{\parallel}/n$) are shown. While both parts roll off with frequency as $(kb)^{-1/2}$, deviations from the $(kb)^{-1/2}$-behavior at low frequencies when $kb \lesssim 1 \times 10^{-8}$ or $f \lesssim 10$ Hz.

Table I: Some definite integrals involving hyperbolic functions.

$\displaystyle\int_0^\infty \frac{d\eta}{\cosh^2 \eta b} = \frac{1}{b}$	$\displaystyle\int_0^\infty \frac{d\eta}{\sinh^2 \eta b} = \infty$
$\displaystyle\int_0^\infty d\eta \, \frac{\eta}{\sinh \eta b} = \frac{\pi^2}{4b^2}$	
$\displaystyle\int_0^\infty d\eta \, \frac{\eta^2}{\cosh^2 \eta b} = \frac{\pi^2}{12b^3}$	
$\displaystyle\int_0^\infty d\eta \, \frac{\eta^2}{\sinh^2 \eta b} = \frac{\pi^2}{6b^3}$	

be seen when $kb \lesssim 1 \times 10^{-8}$ or $f \lesssim 10$ Hz.

We close this section by listing in Table I some of the integrals involving hyperbolic functions that we used.

2.1.2 IMAGE CHARGES AND CURRENT DENSITIES

The discontinuity of the vertical electric field across the surface of the plate gives the electric charge density $\sigma_{\rm im}$ at the surface of the plate. With the help of Eqs. (2.13) and (2.22), we obtain for the upper/lower plate,

$$\begin{aligned}
\sigma_{\rm im}^{\pm}(x) &= \epsilon_0 \left[E_y^{\rm plate} - E_y^{\rm vacuum} \right]_{y=\pm b} \\
&= \mp \int_{-\infty}^{\infty} d\eta \left[\frac{j\eta A_\eta}{k} \sinh \eta b + \frac{j\lambda' A_\eta}{k} \cosh \eta b \right] \cos \eta x \\
&= \mp \int_{-\infty}^{\infty} d\eta \left[\frac{j\eta}{k} \tanh \eta b + \frac{j\lambda'}{k} \right] \frac{\dfrac{\rho_1 \tilde{\sigma}_\eta}{2\epsilon_0} \operatorname{sech} \eta b \, \cos \eta x}{\dfrac{j\lambda'}{k} + j \left(\dfrac{\eta}{k} - \dfrac{k}{\eta} \right) \tanh \eta b} \\
&= \mp \int_{-\infty}^{\infty} d\eta \, \frac{\rho_1 \tilde{\sigma}_\eta}{2\epsilon_0} \operatorname{sech} \eta b \, \cos \eta x \left(1 + \frac{k^2}{\eta \lambda_c} \tanh \eta b \right) \ , \qquad (2.33)
\end{aligned}$$

where we have kept up to the second order in λ_c. For a line charge, $\tilde{\sigma}_\eta = 1/(2\pi)$, the surface

Since $\mathcal{R} \sim \sqrt{k}$ at low frequencies, $a \sim k^{1/4}$. The η/k-term in the denominator of Eq. (2.30) just makes the impedance approach zero a bit faster. Since the low frequency end of $Z_0^{\parallel}$ usually does not affect the beam stability, this η/k-term can be omitted.

charge density becomes

$$\sigma_{\rm ch}^{\pm}(x) = \mp\frac{\rho_1}{2\pi}\int_0^\infty d\eta\,\cos\eta x\,\mathrm{sech}\,\eta b = \mp\frac{\rho_1}{4b}\,\mathrm{sech}\,\frac{\pi x}{2b}\ , \tag{2.34}$$

where ρ_1 is the linear charge density and all higher orders of λ_c^{-1} have been dropped. The image surface current density or image current per unit transverse length in the top/bottom plate is given by

$$K_z^{\pm}(x) = H_x\Big|_{y=\pm b} = \mp\frac{\rho_1 c}{4b}\mathrm{sech}\,\frac{\pi x}{2b}\ . \tag{2.35}$$

2.1.3 OFFSET BEAM

Now we offset the beam vertically so that it is at $y = a$. The two regions in between the plates, $a < y < b$ and $-b < y < a$, no longer exhibit up-down symmetry. As a result, instead of Eq. (2.12), we must write

$$\begin{cases} \tilde{E}_z = A_\eta\cosh\eta y + \bar{A}_\eta\sinh\eta y\ , \\ Z_0\tilde{H}_z = A_\eta\sinh\eta y + \bar{A}_\eta\cosh\eta y\ . \end{cases} \tag{2.36}$$

The vertical field components become

$$\begin{cases} \tilde{E}_y = \left[\frac{j}{2}\left(\frac{k}{\eta}+\frac{\eta}{k}\right)A_\eta + B_\eta\right]\sinh\eta y + \left[\frac{j}{2}\left(\frac{k}{\eta}+\frac{\eta}{k}\right)\bar{A}_\eta + \bar{B}_\eta\right]\cosh\eta y \pm \frac{\rho_1\tilde{\sigma}_\eta}{2\epsilon_0}\cosh\eta(y-a)\ , \\ Z_0\tilde{H}_y = \left[\frac{j}{2}\left(\frac{k}{\eta}+\frac{\eta}{k}\right)A_\eta - B_\eta\right]\cosh\eta y + \left[\frac{j}{2}\left(\frac{k}{\eta}+\frac{\eta}{k}\right)\bar{A}_\eta - \bar{B}_\eta\right]\sinh\eta y \mp \frac{\rho_1\tilde{\sigma}_\eta}{2\epsilon_0}\sinh\eta(y-a)\ . \end{cases} \tag{2.37}$$

The horizontal components are obtained from

$$\begin{cases} \tilde{E}_x = Z_0\tilde{H}_y - \frac{j\eta}{k}\tilde{E}_z\ , \\ Z_0\tilde{H}_x = -\tilde{E}_y + \frac{j\eta}{k}Z_0\tilde{H}_z\ . \end{cases} \tag{2.38}$$

Inside the metallic plates, the longitudinal field components are

$$\begin{cases} \tilde{E}_z = \left(A_\eta\cosh\eta b \pm \bar{A}_\eta\sinh\eta b\right)e^{\lambda'(b\mp y)}\ , \\ \tilde{Z}_0 H_z = \left(\pm A_\eta\sinh\eta b \pm \bar{A}_\eta\cosh\eta b\right)e^{\lambda'(b\mp y)}\ , \end{cases} \tag{2.39}$$

and the transverse components are

$$\begin{cases} \tilde{E}_x = \dfrac{1}{Z_0\sigma_c}\Big[-A_\eta\big(\eta\cosh\eta b+\lambda'\sinh\eta b\big)\mp\bar{A}_\eta\big(\eta\sinh\eta b+\lambda'\cosh\eta b\big)\Big]e^{\lambda'(b\mp y)}\ , \\ \tilde{E}_y = \dfrac{1}{Z_0\sigma_c}\Big[\mp A_\eta\big(\eta\sinh\eta b+\lambda'\cosh\eta b\big)-\bar{A}_\eta\big(\eta\cosh\eta b+\lambda'\sinh\eta b\big)\Big]e^{\lambda'(b\mp y)}\ , \\ Z_0\tilde{H}_x = -\tilde{E}_y+\dfrac{j}{k}\dfrac{\partial\tilde{E}_z}{\partial y}\ , \\ Z_0\tilde{H}_y = \tilde{E}_x+\dfrac{j\eta}{k}\tilde{E}_z\ . \end{cases} \tag{2.40}$$

The continuities of $\tilde{E}_x$ and $\tilde{H}_x$ across the plate surfaces at $y=\pm b$ lead to the restrictions:

$$\begin{cases} \Big[\dfrac{j}{2}\Big(\dfrac{k}{\eta}+\dfrac{\eta}{k}\Big)A_\eta-B_\eta\Big]\cosh\eta b\pm\Big[\dfrac{j}{2}\Big(\dfrac{k}{\eta}+\dfrac{\eta}{k}\Big)\bar{A}_\eta-\bar{B}_\eta\Big]\sinh\eta b\mp\dfrac{\rho_1\tilde{\sigma}_\eta}{2\epsilon_0}\sinh\eta(\pm b-a) \\ \qquad -\dfrac{j\eta}{k}\big(A_\eta\cosh\eta b\pm\bar{A}_\eta\sinh\eta b\big) \\ \qquad =\dfrac{1}{Z_0\sigma_c}\Big[-A_\eta\big(\eta\cosh\eta b+\lambda'\sinh\eta b\big)\mp\bar{A}_\eta\big(\eta\sinh\eta b+\lambda'\cosh\eta b\big)\Big]\ , \\ \mp\Big[\dfrac{j}{2}\Big(\dfrac{k}{\eta}+\dfrac{\eta}{k}\Big)A_\eta+B_\eta\Big]\sinh\eta b-\Big[\dfrac{j}{2}\Big(\dfrac{k}{\eta}+\dfrac{\eta}{k}\Big)\bar{A}_\eta+\bar{B}_\eta\Big]\cosh\eta b\mp\dfrac{\rho_1\tilde{\sigma}_\eta}{2\epsilon_0}\cosh\eta(\pm b-a) \\ \qquad +\dfrac{j\eta}{k}\big(\pm A_\eta\sinh\eta b+\bar{A}_\eta\cosh\eta b\big) \\ \qquad =\dfrac{1}{Z_0\sigma_c}\Big[\pm A_\eta\big(\eta\sinh\eta b+\lambda'\cosh\eta b\big)+\bar{A}_\eta\big(\eta\cosh\eta b+\lambda'\sinh\eta b\big)\Big] \\ \qquad \mp\dfrac{j\lambda'}{k}\big(A_\eta\cosh\eta b\pm\bar{A}_\eta\sinh\eta b\big)\ . \end{cases} \tag{2.41}$$

The continuities of $\tilde{H}_y$ give the same restrictions as those of $\tilde{E}_x$. Here, we have four restrictions, from which the four unknowns A_η, $\bar{A}_\eta$, B_η, and $\bar{B}_\eta$ can be solved. It turns out that these four restrictions separate into four relations, two involving only A_η and B_η, and two involving only $\bar{A}_\eta$ and $\bar{B}_\eta$, making their solutions extremely easy. We get

$$\begin{cases} \Big[\dfrac{j}{2}\Big(\dfrac{k}{\eta}-\dfrac{\eta}{k}\Big)A_\eta-B_\eta\Big]\cosh\eta b=\dfrac{\rho_1\tilde{\sigma}_\eta}{2\epsilon_0}\sinh\eta b\cosh\eta a-\dfrac{A_\eta}{Z_0\sigma_c}\big(\eta\cosh\eta b+\lambda'\sinh\eta b\big) \\ -\Big[\dfrac{j}{2}\Big(\dfrac{k}{\eta}-\dfrac{\eta}{k}\Big)A_\eta+B_\eta\Big]\sinh\eta b=\dfrac{\rho_1\tilde{\sigma}_\eta}{2\epsilon_0}\cosh\eta b\cosh\eta a+\dfrac{A_\eta}{Z_0\sigma_c}\big(\eta\sinh\eta b+\lambda'\cosh\eta b\big) \\ \qquad -\dfrac{j\lambda'}{k}A_\eta\cosh\eta b\ . \end{cases} \tag{2.42}$$

$$\begin{cases} \left[\frac{j}{2}\left(\frac{k}{\eta}-\frac{\eta}{k}\right)\bar{A}_\eta-\bar{B}_\eta\right]\sinh\eta b = -\frac{\rho_1\tilde{\sigma}_\eta}{2\epsilon_0}\cosh\eta b\,\sinh\eta a - \frac{\bar{A}_\eta}{Z_0\sigma_c}\big(\eta\sinh\eta b+\lambda'\cosh\eta b\big) \\ -\left[\frac{j}{2}\left(\frac{k}{\eta}-\frac{\eta}{k}\right)\bar{A}_\eta+\bar{B}_\eta\right]\cosh\eta b = -\frac{\rho_1\tilde{\sigma}_\eta}{2\epsilon_0}\sinh\eta b\,\sinh\eta a + \frac{\bar{A}_\eta}{Z_0\sigma_c}\big(\eta\cosh\eta b+\lambda'\sinh\eta b\big) \\ \qquad\qquad - \frac{j\lambda'}{k}\bar{A}_\eta\sinh\eta b\ . \end{cases} \tag{2.43}$$

From these, we can solve for

$$\begin{cases} A_\eta = \dfrac{-\frac{\rho_1\tilde{\sigma}_\eta}{2\epsilon_0}\Big(\coth\eta b-\tanh\eta b\Big)\cosh\eta a}{-\frac{j\lambda'}{k}\coth\eta b + j\left(\frac{k}{\eta}-\frac{\eta}{k}\right)+\frac{jk\lambda'}{\lambda_c^2}\Big(\tanh\eta b+\coth\eta b\Big)+\frac{j2k\eta}{\lambda_c^2}}\ , \\ \bar{A}_\eta = \dfrac{-\frac{\rho_1\tilde{\sigma}_\eta}{2\epsilon_0}\Big(\coth\eta b-\tanh\eta b\Big)\sinh\eta a}{-\frac{j\lambda'}{k}\tanh\eta b + j\left(\frac{k}{\eta}-\frac{\eta}{k}\right)+\frac{jk\lambda'}{\lambda_c^2}\Big(\tanh\eta b+\coth\eta b\Big)+\frac{j2k\eta}{\lambda_c^2}}\ . \end{cases} \tag{2.44}$$

If we keep only up to the second order in $|\lambda_c|$, we obtain the longitudinal field component at a vertical distance y,

$$\tilde{E}_z(y) = -\frac{\rho_1\tilde{\sigma}_\eta c\mathcal{R}}{2}\left[\frac{\operatorname{sech}^2\eta b\,\cosh\eta a\,\cosh\eta y}{1-\frac{k}{\lambda_c}\left(\frac{k}{\eta}-\frac{\eta}{k}\right)\tanh\eta b}+\frac{\operatorname{csch}^2\eta b\,\sinh\eta a\,\sinh\eta y}{1-\frac{k}{\lambda_c}\left(\frac{k}{\eta}-\frac{\eta}{k}\right)\coth\eta b}\right]\ , \tag{2.45}$$

where $\mathcal{R}=\lambda/\sigma$. Including all components of η, the longitudinal electric field at the point (x,y) is

$$E_z(x,y) = -\rho_1 c\mathcal{R}\int_0^\infty d\eta\,\tilde{\sigma}_\eta\cos\eta x\left[\frac{\operatorname{sech}^2\eta b\,\cosh\eta a\,\cosh\eta y}{1+\frac{j\mathcal{R}}{Z_0}\left(\frac{k}{\eta}-\frac{\eta}{k}\right)\tanh\eta b}+\frac{\operatorname{csch}^2\eta b\,\sinh\eta a\,\sinh\eta y}{1+\frac{j\mathcal{R}}{Z_0}\left(\frac{k}{\eta}-\frac{\eta}{k}\right)\coth\eta b}\right]\ . \tag{2.46}$$

2.1.4 IMPEDANCES OF CENTERED BEAM

For convenience, let us consider a pencil beam, $\tilde{\sigma}_\eta = 1/(2\pi)$, at $x=0$ but displaced vertically by a small amount at $y=a$. The longitudinal electric field on a test particle at

$x = 0$ and $y = \xi$ can be written as an expansion in a and ξ from Eq. (2.46):

$$\begin{aligned} E_z = &- \frac{I\mathcal{R}}{2\pi}\int_0^\infty \frac{d\eta}{\cosh^2\eta b} - \frac{I\xi^2\mathcal{R}}{2\pi}\int_0^\infty d\eta\,\frac{\eta^2}{\cosh^2\eta b} \\ &- \frac{Ia\xi\mathcal{R}}{2\pi}\int_0^\infty d\eta\,\frac{\eta^2}{\sinh^2\eta b} - \frac{Ia^2\mathcal{R}}{2\pi}\int_0^\infty d\eta\,\frac{\eta^2}{\cosh^2\eta b} + \cdots\ , \end{aligned} \tag{2.47}$$

where the denominators containing higher-order $\mathcal{R}/Z_0$ have been omitted for the sake of clarity. On the right, the first two terms are the monopole and quadrupole E_z from an on-axis monopole beam current, the third term is dipole E_z from a dipole current Ia, the fourth term is the monopole field from a quadrupole Ia^2 beam. The complication, that a multipole field arises from a different multipole source, occurs because Eq. (2.47) is not an exact multipole expansion.* Nevertheless, the expansion is still useful when only the lowest multipoles for the longitudinal and transverse impedances are desired. Thus, when the frequency is not too low, the longitudinal monopole impedance of a centered beam per unit length is

$$\frac{Z_0^\parallel}{L} = -\frac{E_z}{I}\bigg|_{\substack{a=0\\ \xi=0}} = \frac{\mathcal{R}}{2\pi b}\ , \tag{2.48}$$

agreeing with our former derivation in Eq. (2.31). Although the higher-order term has been shown to be not too important for $Z_0^\parallel$, however, it is important in the dipole mode when $k \to 0$, especially in laminated magnets where the effective surface impedance per square is much larger than the ordinary surface impedance per square of a metallic surface. Picking out the appropriate term in Eq. (2.47), the longitudinal dipole impedance can be expressed

*The expansion is exactly multipole for a beam inside a cylindrical beam pipe. For example, for a monopole ring beam of radius a inside a beam pipe of radius b traveling in the z direction, E_z at $a < r < b$ is independent of r and the azimuthal angle. For a dipole ring beam Ia at radius a, E_z at $r = \xi$ is proportional to $Ia\xi$, and there are no other terms like $Ia\xi^3$ etc. However, for a pencil beam at the original between two parallel plates at $y = \pm b$, E_z depends on both x and y. This explains why we have the second term, proportional to ξ^2, in Eq. (2.47). To obtain a true multipole expansion, i.e., getting rid of terms like the second and fourth in Eq. (2.47), one needs to perform a conformal mapping of the circular beam pipe onto the two parallel plates and map the multipole ring beam of radius a onto two infinite sheets of beam at $y = \pm a$. For this two-parallel-plate system, the true monopole mode consists of two infinite sheets of current at $y = \pm a$ flowing in the z-direction and corresponds to the first term of Eq. (2.46) with $\tilde{\sigma}_\eta = \delta(\eta)/w$, where $w \to \infty$ is the total horizontal width of the beam. The dipole mode consists of having the two current sheets at $y = \pm a$ but flowing in, respectively, the $\pm z$-directions, and corresponds to the second term of Eq. (2.46). Thus for a sheet of current at an offset $y = a$ flowing in the z-direction, $E_z(x, y) = -I\mathcal{R}/2 - Iay\mathcal{R}/(2b^2)$, where I is now the current per unit horizontal width. It appears that the mapping transforms the cylindrical beam pipe into a two-dimensional problem, which can support only two modes.

as

$$\frac{Z_1^{\parallel}}{L} = -\frac{E_z}{Ia\xi}\bigg|_{\substack{a=0\\ \xi=0}} = \frac{\mathcal{R}}{2\pi}\int_0^\infty d\eta\,\frac{\eta^2 \mathrm{csch}^2\eta b}{1-\dfrac{j\mathcal{R}\eta}{Z_0 k}\coth\eta b} \ . \tag{2.49}$$

We therefore have†

$$\frac{Z_1^{\parallel}}{L} = \begin{cases} \dfrac{\pi\mathcal{R}}{12b^3} & |\lambda_c b| \gg 1 \ , \\[2ex] \dfrac{\pi k Z_0}{16b^2}\left(\dfrac{4b}{\pi^2}\sqrt{\dfrac{k}{\chi}}+j\right) & |\lambda_c b| \ll 1 \ , \end{cases} \tag{2.51}$$

where we have used the fact that, at low frequencies,

$$\mathcal{R}/Z_0 = (1+j)\sqrt{k\chi} \ , \tag{2.52}$$

where χ is frequency independent. For the smooth resistive wall surface,

$$\chi = \frac{\mu_r}{2Z_0\sigma_c} \ . \tag{2.53}$$

The change in behavior occurs at

$$|\lambda_c b| \sim 1 \ , \tag{2.54}$$

which is just Eq. (1.4), or

$$kb \sim \frac{1}{Z_0 b\sigma_c\mu_r} = 1\times 10^{-8} \qquad \text{or} \qquad f \sim \frac{c}{2\pi Z_0 b^2\sigma_c\mu_r} = 10 \text{ Hz} \ , \tag{2.55}$$

when the two metallic plates are separated by $2b = 10$ cm and the wall conductivity is $\sigma_c = 0.5\times 10^7$ $(\Omega\text{-m})^{-1}$.

For the vertical dipole impedance, we need to compute the vertical Lorentz force $\tilde{F}_V(y)$ acting on a particle at y. With the help of the Maxwell's law of displacement current,

$$\tilde{F}_V(y) = e(\tilde{E}_y + Z_0\tilde{H}_x) = e\frac{j\eta}{k}Z_0\tilde{H}_z = -\frac{jeI\mathcal{R}\tilde{\sigma}_\eta\eta}{2k}\left[\frac{\cosh\eta a\sinh\eta y}{\{\ \}\cosh^2\eta b} + \frac{\sinh\eta a\cosh\eta y}{\{\ \}\sinh^2\eta b}\right] \tag{2.56}$$

where $\{\ \}$ denotes the denominators involving the next order of $\mathcal{R}$. Notice that although both $\tilde{E}_y$ and $\tilde{H}_x$ are discontinuous across the particle beam, the Lorentz force, which is

†The low-frequency behavior can be derived from

$$\frac{Z_1^{\parallel}}{L} = \frac{Z_0 k}{2\pi}\int_0^\infty d\eta\frac{\eta\,\mathrm{csch}^2\eta b}{\coth\eta b}\frac{1+j}{\dfrac{Z_0 k}{\mathcal{R}\eta\coth\eta b}+1-j} \approx \frac{Z_0 k}{2\pi}\int_0^\infty d\eta\frac{\eta\,\mathrm{csch}^2\eta b}{\coth\eta b}\left(j+\frac{\sqrt{k/\chi}}{2\eta\coth\eta b}\right) \ . \tag{2.50}$$

proportional to $\tilde{H}_z$, is continuous. It is important to realize that[‡] $F_V \sim \tilde{F}_V \cos\eta x$ because it is derived from E_y and H_x. For a pencil beam at $x = 0$ with small offset $y = a \ll b$, this reduces to

$$\left.\frac{F_V}{e}\right|_{\xi=0} = -\frac{jIa\mathcal{R}}{2\pi k}\int_0^\infty d\eta \frac{\eta^2}{\sinh^2\eta b}\frac{1}{1-\dfrac{j\mathcal{R}\eta}{Z_0 k}\coth\eta b} \ . \tag{2.57}$$

Thus the vertical dipole impedance per unit longitudinal length is

$$\frac{Z_1^V}{L} = -\left.\frac{F_V/e}{jIa}\right|_{\substack{a=0\\ \xi=0}} = \begin{cases} \dfrac{\pi\mathcal{R}}{12kb^3} & |\lambda_c b| \gg 1 \ , \\ \dfrac{\pi Z_0}{16b^2}\left(\dfrac{4b}{\pi^2}\sqrt{\dfrac{k}{\chi}} + j\right) & |\lambda_c b| \ll 1 \ . \end{cases} \tag{2.58}$$

We notice that $Z_1^{\|}$ and Z_1^V are related through the Panofsky-Wenzel condition. It is important to note that although Z_1^V increases according to $k^{-1/2}$, however, it does not get to $\pm\infty$ as $k \to 0$. On the other hand, the resistive part of Z_1^V bends around and rolls to zero at zero frequency. The real and imaginary parts of Z_1^V are shown in the top plot of Fig. 3 in the model when the plate separation is $2b = 10$ cm and the wall conductivity is $\sigma_c = 0.5\times 10^7$ $(\Omega\text{-m})^{-1}$. The frequency range is from $f = 0.001$ Hz to 100 GHz (kb from 10^{-12} to 10^2.) We see that both real and imaginary parts of the impedance decrease according to $(kb)^{-1/2}$. However, when the frequency is small enough the inductive part approaches the value $\pi Z_0/(16b^2)$ while the real part bends over and goes to zero according to[§] $\sqrt{kb}$. As pointed out in the previous subsection, $\mathcal{R}e\, Z_1^V$ bends around when $kb = 1\times 10^{-8}$ or $f = 10$ Hz when $b = 5$ cm. Since this frequency is so much less than the typical revolution frequency of any existing accelerator ring, the bend-around will not influence the negative betatron line closest to zero frequency that drives transverse coupled-bunch instabilities. For the 231 km Very Large Hadron Collider (VLHC) under design which has a revolution frequency of 1.29 kHz, the radius of the beam pipe has been proposed to be $b = 1$ cm. [4] Corresponding to $|\lambda_c b| = 1$, the bend-around frequency is $f = 250$ Hz. However, according to Fig. 3 $\mathcal{R}e\, Z_1^V$ begins to deviate from the $\omega^{-1/2}$ behavior when the frequency is below ~ 2.5 kHz ($kb \sim 10^{-7}$). In reality, the wall of the beam pipe has a finite thickness, electromagnetic fields leaking outside will see a much larger resistivity, resulting in a further increase of this bend-around frequency. Thus

[‡]It is incorrect to associate $\tilde{F}_V$ with $\sin\eta x$ just because it is proportional to $\tilde{H}_z$. Actually we have $\tilde{F}_V \propto \eta\tilde{H}_z \propto \partial\tilde{H}_z/\partial x$.

[§]As will be shown in Eq. (2.94) and Fig. 4 below, the behavior of the transverse dipole impedance is very similar for a beam inside a cylindrical beam pipe. However, $\mathcal{R}e\, Z_1^\perp$ for the cylindrical beam pipe goes to zero at low frequencies linearly rather than as $\sqrt{kb}$ here.

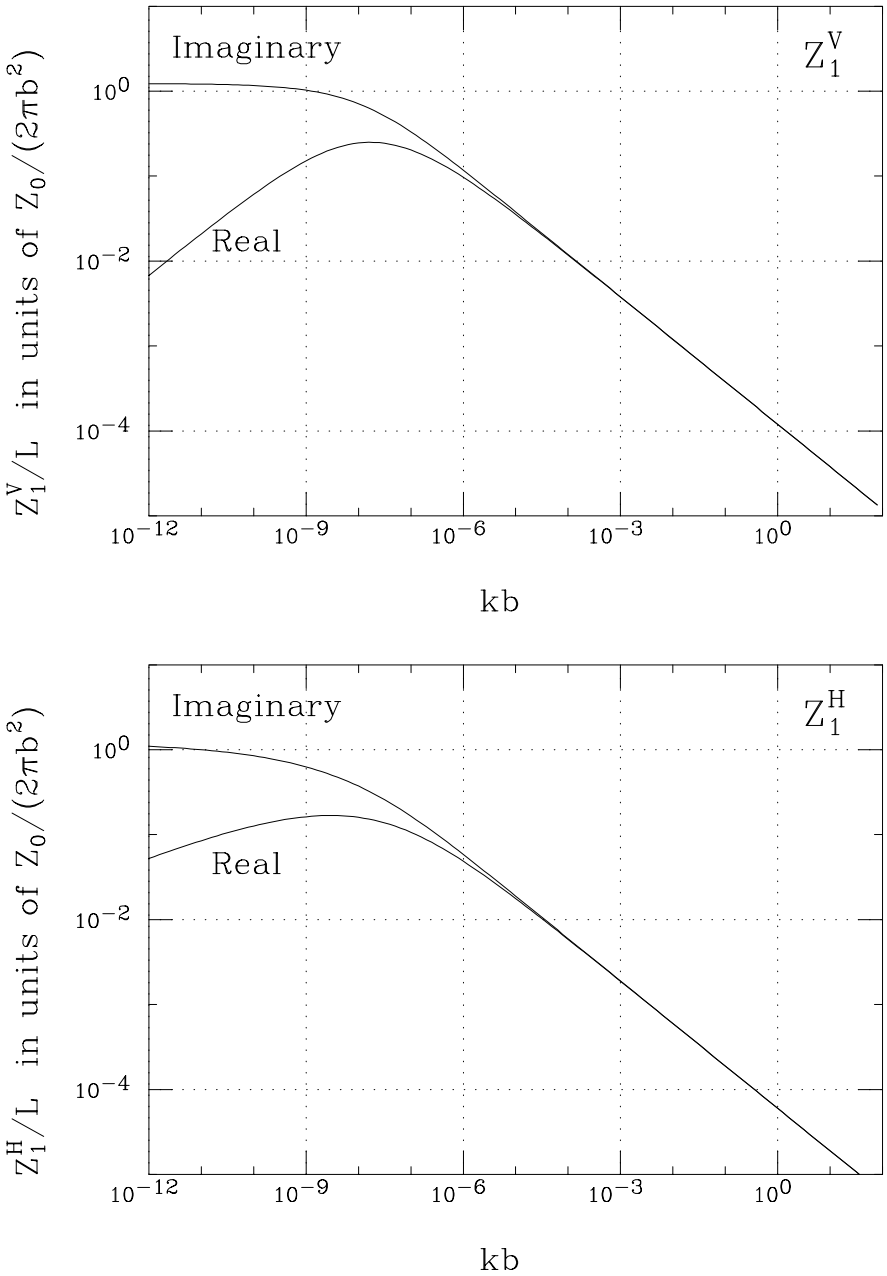

Figure 3: The real and imaginary parts of the vertical dipole impedance (top) and horizontal impedance (bottom) are shown as functions of kb for a beam in between two parallel plates separated by $2b = 10$ cm with wall conductivity $\sigma_c = 0.5 \times 10^7$ $(\Omega\text{-m})^{-1}$ (stainless steel). While both parts decrease with frequency as $(kb)^{-1/2}$, the imaginary parts reach finite values at $kb = 0$ and the real part decreases to zero at zero frequency. $\mathcal{R}e\, Z_1^V$ goes to zero as $\sqrt{kb}$. and $\mathcal{R}e\, Z_1^H$ goes to zero much slower.

this low-energy behavior may be important for the VLHC. [5] The low-frequency limit of the inductance is called *bypass inductance* after Vos. [3] This is a geometric effect of the beam pipe and is determined by the loop of image currents flowing in the walls of the beam pipe in the dipole mode and are referred to as *differential currents*. The bypass inductance just comes from the flux linking this differential current loop. We will go over this concept in Sec. 2.2.2 below.

For the laminated magnets that we are going to discuss later, the effective surface impedance per square is much larger than that of a smooth metallic wall because the image current has to go around each lamination. As we shall see in Sec. 3 below, the effective surface impedance per square does not follow a $\sqrt{k}$-dependency, the bend-around frequency is not given by Eq. (2.55). We shall show that the bend-around takes place at a much higher frequency ($\gtrsim$ 100 MHz) so that the negative betatron lines close to the zero frequency are no longer strong enough to drive any transverse coupled-bunch instabilities.

For the horizontal dipole impedance, we first compute the horizontal Lorentz force acting on a particle at x. The Fourier transform of the force is,[¶] via Faraday's law,

$$\tilde{F}_H = e(\tilde{E}_x - Z_0\tilde{H}_y) = -\frac{je\eta}{k}\tilde{E}_z \ , \tag{2.59}$$

and the horizontal force itself is

$$F_H(x) = -\int_0^\infty 2d\eta \, \sin\eta x \, \frac{je\eta}{k}\tilde{E}_z \ . \tag{2.60}$$

For a dipole beam $I\Delta$, we differentiate with respect to x to get the corresponding horizontal force F'_H acting on the particle[‖]

$$F'_H = -\Delta\frac{\partial F_H}{\partial x}\Big|_{x=0} = -\frac{jeI\Delta\mathcal{R}}{2\pi k}\int_0^\infty d\eta\left(\frac{\eta^2\cosh^2\eta a}{\{\ \}\cosh^2\eta b} + \frac{\eta^2\sinh^2\eta a}{\{\ \}\sinh^2\eta b}\right) \ . \tag{2.61}$$

where the expression for $\tilde{E}_z$ in Eq. (2.45) has been used and $\{\ \}$ denote the denominators involving the next order of $\mathcal{R}/Z_0$. The horizontal dipole impedance per unit longitudinal length is therefore

$$\frac{Z_1^H}{L} = -\frac{F'_H/e}{jI\Delta} = \frac{\mathcal{R}}{2\pi k}\int_0^\infty d\eta\left(\frac{\eta^2\cosh^2\eta a}{\{\ \}\cosh^2\eta b} + \frac{\eta^2\sinh^2\eta a}{\{\ \}\sinh^2\eta b}\right) \ , \tag{2.62}$$

[¶]Here F_H is related to $\sin\eta x$ because it is derived from E_x and H_y and is proportional to $\partial\tilde{E}_z/\partial x$.

[‖]$d\sigma(x)/dx$ gives a positive bump at $x < 0$ and a negative bump at $x > 0$. Thus, to create a dipole beam, we need $I\Delta = -\Delta I d\sigma(x)/dx$. This can also be verified by integrating $-xId\sigma(x)/dx$. Notice that for the vertical dipole impedance, we use $d\sigma(y-a)/da$ in Eq. (2.66) below to create the dipole source, and the same negative sign will be required if we differentiate with respect to y instead.

which reduces to, for a centered beam,

$$\frac{Z_1^H}{L} = \frac{\mathcal{R}}{2\pi k}\int_0^\infty d\eta \frac{\eta^2 \mathrm{sech}^2 \eta b}{1 - \dfrac{j\mathcal{R}\eta}{Z_0 k}\tanh \eta b} \ . \tag{2.63}$$

The result is

$$\frac{Z_1^H}{L} == \begin{cases} \dfrac{\pi\mathcal{R}}{24kb^3} & |\lambda_c b| \gg 1 \ , \\ \dfrac{\pi Z_0}{16b^2}\Big[f(k) + j\Big] & |\lambda_c b| \ll 1 \ , \end{cases} \tag{2.64}$$

where** $\lim_{k\to 0} f(k) = 0$. Here, we also see a bend-over of the inductive part to a constant and the real part to zero, when the frequency is low enough. The real and imaginary parts of Z_1^H are shown in the bottom plot of Fig. 3. We see that they have similar behavior as those of Z_1^V. The bend-over frequencies are also similar. However, at low frequency $\mathcal{R}e\, Z_1^H$ approaches zero much slower than $\mathcal{R}e\, Z_1^H$.

It is not strange to find a nonvanishing horizontal dipole impedance when the infinite plates have horizontal translational symmetry. The horizontal dipole impedance is proportional to the horizontal force acting on a beam particle, which is the witness, due to the dipole motion of the center of the beam, which is the source. We see first that there is no more translational symmetry in the presence of the dipole current and second that this force is independent of the horizontal offset of the witness particle. This also explains why the incoherent horizontal tune shift due to images is nonzero. On the other hand, the coherent tune shift due to images vanishes, because it describes the force acting on the center of the beam by the dipole motion of the center of the beam.

Sometimes, the beam may be at a large offset a from the center of the parallel-plate gap. To derive the vertical dipole impedance of such an offset beam, we try to create a dipole at

**If we just pick out the $\mathcal{R}$-dependent term in the denominator of Eq. (2.63), it is easy to show that $Z_1^H/L = j\pi Z_0/(16b^2)$. Thus the real part goes to zero as $k \to 0$. To compute $f(k)$ or the way $\mathcal{R}e\, Z_1^H$ going to zero is not so simple. We have from Eq. (2.63),

$$\frac{Z_1^H}{L} = \frac{Z_0}{2\pi}\int_0^\infty d\eta\, \frac{\eta\, \mathrm{sech}^2 \eta b}{\tanh \eta b}\, \frac{\dfrac{\sqrt{k}}{\sqrt{\chi}\,\eta \tanh \eta b} + j\left(2 + \dfrac{\sqrt{k}}{\sqrt{\chi}\,\eta \tanh \eta b}\right)}{\left(1 + \dfrac{\sqrt{k}}{\sqrt{\chi}\,\eta \tanh \eta b}\right)^2 + 1} \tag{2.65}$$

If we set $k = 0$ in the denominator, we find the real part of the integral diverges as η^{-2}. This divergence should not occur if we do the integral first before letting $k \to 0$ in the denominator.

$y = a$ by a vertical offset Δ. The vertical force due to the dipole current $I\Delta$ is derived from the vertical force in Eq. (2.56) by

$$\frac{F'_V}{e} = \Delta \frac{\partial F_V}{\partial a}\Big|_{y=a} = -\frac{jeI\Delta\mathcal{R}}{k}\int_0^\infty d\eta\, \tilde{\sigma}_\eta \cos\eta x \left[\frac{\eta^2 \sinh\eta a \sinh\eta y}{\{\ \}\cosh^2\eta b} + \frac{\eta^2\cosh\eta a\cosh\eta y}{\{\ \}\sinh^2\eta b}\right], \tag{2.66}$$

where the higher orders in $\mathcal{R}$ are represented by $\{\ \}$. For a pencil beam at $y = a$, the vertical dipole impedance is therefore

$$\frac{Z_1^V}{L} = -\frac{F'_V/e}{jI\Delta} = \frac{\mathcal{R}}{2\pi k}\int_0^\infty d\eta \left[\frac{\eta^2 \mathrm{sech}^2\eta b \sinh^2\eta a}{1 - \frac{j\mathcal{R}\eta}{Z_0 k}\tanh\eta b} + \frac{\eta^2 \mathrm{csch}^2\eta b\cosh^2\eta a}{1 - \frac{j\mathcal{R}\eta}{Z_0 k}\coth\eta b}\right]. \tag{2.67}$$

which reduces to that of an on-axis dipole in Eq. (2.66). We have the same $k^{-1/2}$ behavior here for low frequencies. After some critical frequency, the inductive part approaches a finite value at zero frequency while the real part rolls off to zero according to $\sqrt{k}$. For such an offset beam, the longitudinal impedance is

$$\frac{Z_0^\parallel}{L} = -\frac{E_z}{I}\Big|_{y=a} = \mathcal{R}\int_0^\infty d\eta \left[\frac{\cosh^2\eta a}{\cosh^2\eta b} + \frac{\sinh^2\eta a}{\sinh^2\eta b}\right]. \tag{2.68}$$

From Eq. (2.56), we learn that the beam m is also experiencing a vertical force and therefore a vertical monopole impedance

$$\frac{Z_0^V}{L} = -\frac{F_V/e}{jI}\Big|_{y=a} = \frac{\mathcal{R}}{2\pi k}\int_0^\infty d\eta \left[\frac{\eta\sinh\eta a\cosh\eta a}{\cosh^2\eta b} + \frac{\eta\sinh\eta a\cosh\eta a}{\sinh^2\eta b}\right]. \tag{2.69}$$

However, in order for the closed orbit to be stable at a large offset, there must be some external force to counteract this vertical force. As a result this vertical monopole impedance will not be important.

2.1.5 EFFECTIVE SURFACE IMPEDANCES PER SQUARE

Instead of going into the detail of a surface, we can define the effective surface impedances per square as

$$E_z = \pm\mathcal{R}_z H_x \qquad \text{and} \qquad E_x = \mp\mathcal{R}_x H_z\ . \tag{2.70}$$

where E_x, E_z, H_x, and H_z are the components of the electric and magnetic fields on the surface of the upper/lower plate. Physically, we can imagine H_x at the upper surface sets up a current per width inside the surface in the z-direction and therefore a E_z at the surface.

Similarly, H_z at the surface sets up a current per width inside the surface in the $-x$-direction and therefore a $-E_x$ at the surface. In this way, the ratios E_z/H_x and $-E_x/H_z$ just give the surface impedances per square $\mathcal{R}_z$ and $\mathcal{R}_x$. We distinguish the surface impedances per square in the z-direction and x-direction, because the surface may have different impedances in different direction. This is especially true for a laminated surface. The impedance is large across the cracks of the laminated surface, and is small in the perpendicular direction.

Let us apply this concept to the offset beam traveling between two resistive metallic plates. The field components, given by Eqs. (2.36) to (2.38), are evaluated at the plate surfaces $y = \pm b$, and then substituted into the boundary conditions in Eq. (2.70). We obtain four equations in four unknowns A_η, $\bar{A}_\eta$, B_η, and $\bar{B}_\eta$. The solution gives

$$\begin{cases} A_\eta = \dfrac{-\dfrac{\rho_1\tilde{\sigma}_\eta}{2\epsilon_0}\Big(\coth\eta b - \tanh\eta b\Big)\cosh\eta a}{\dfrac{Z_0}{\mathcal{R}_z}\coth\eta b + j\left(\dfrac{k}{\eta} - \dfrac{\eta}{k}\right) + \dfrac{\mathcal{R}_x}{Z_0}\tanh\eta b} \ , \\ \bar{A}_\eta = \dfrac{-\dfrac{\rho_1\tilde{\sigma}_\eta}{2\epsilon_0}\Big(\coth\eta b - \tanh\eta b\Big)\sinh\eta a}{\dfrac{Z_0}{\mathcal{R}_z}\tanh\eta b + j\left(\dfrac{k}{\eta} - \dfrac{\eta}{k}\right) + \dfrac{\mathcal{R}_x}{Z_0}\coth\eta b} \ . \end{cases} \tag{2.71}$$

Noting that

$$\frac{j\lambda_c}{k} = -\frac{Z_0}{\mathcal{R}_{x,z}} \ , \tag{2.72}$$

the solution agrees with the exact solution up to the next order in λ_c. We also notice that, up to this order in λ_c, the term involving $\mathcal{R}_x/Z_0$ in Eq. (2.71) can be neglected. Thus only the surface impedance per square in the direction of the beam plays a role in the coupling impedances.

2.2 CYLINDRICAL BEAM PIPE

2.2.1 ON-AXIS BEAM

The resistive wall impedances seen by a beam inside a cylindrical beam pipe have been derived in great detail by Chao.[2] Here, we just repeat the derivation in MKS units with the addition of giving the coupling impedances for a beam with a large offset. A particle beam of linear charge density ρ_1 traveling inside the beam pipe at an offset a at the azimuthal

angle $\theta = 0$ has its charge density and current expanded as azimuthal harmonics

$$\rho(r,\theta,z,t) = \sum_{m=0}^{\infty} \bar{\rho}_m \quad \text{and} \quad \vec{J} = \sum_{m=0}^{\infty} \vec{J}_m \ . \tag{2.73}$$

Here

$$\begin{aligned} \bar{\rho}_m &= \frac{I_m}{\pi a^{m+1}(1+\delta_{m0})} \delta(r-a) \cos m\theta \, e^{j(\omega t - kz)} \ , \\ \vec{J}_m &= \beta c \rho_m \hat{z} \ , \end{aligned} \tag{2.74}$$

where $I_m = \rho_1 a^m$ is the m-multipole of the linear charge density. To simplify the derivation, the particle beam velocity is assumed to be c. The field components are written in terms of their multipole components, with an overhead tilde,

$$\begin{cases} \big(E_r,\ E_z,\ H_\theta\big) = \displaystyle\sum_{m=0}^{\infty} \cos m\theta \big(\tilde{E}_r,\ \tilde{E}_z,\ \tilde{H}_\theta\big) \ , \\ \big(H_r,\ H_z,\ E_\theta\big) = \displaystyle\sum_{m=0}^{\infty} \sin m\theta \big(\tilde{H}_r,\ \tilde{H}_z,\ \tilde{E}_\theta\big) \ , \end{cases} \tag{2.75}$$

where the choice of $\cos m\theta$ and $\sin m\theta$ are chosen according to the charge and current multipoles. The Maxwell's equations inside the beam pipe ($r < b$) are

$$\begin{cases} \dfrac{1}{r}\dfrac{\partial(r\tilde{E}_r)}{\partial r} + \dfrac{m}{r}\tilde{E}_\theta - jk\tilde{E}_z = \dfrac{I_m \delta(r-a)}{\epsilon_0 \pi a^{m+1}(1+\delta_{m0})} \ , \\ \dfrac{1}{r}\dfrac{\partial(r\tilde{H}_r)}{\partial r} - \dfrac{m}{r}\tilde{H}_\theta - jk\tilde{H}_z = 0 \ , \\ -\dfrac{m}{r}\tilde{E}_z + jk\tilde{E}_\theta + jkZ_0\tilde{H}_r = 0 \ , \\ -jk\tilde{E}_r - \dfrac{\partial \tilde{E}_z}{\partial r} + jkZ_0\tilde{H}_\theta = 0 \ , \\ \dfrac{\partial \tilde{E}_\theta}{\partial r} + \dfrac{m}{r}\tilde{E}_r + jkZ_0\tilde{H}_z = 0 \ , \\ \dfrac{m}{r}Z_0\tilde{H}_z + jkZ_0\tilde{H}_\theta - jk\tilde{E}_r = 0 \ , \\ -jkZ_0\tilde{H}_r - \dfrac{\partial Z_0\tilde{H}_z}{\partial r} - jk\tilde{E}_\theta = 0 \ , \\ \dfrac{\partial Z_0\tilde{H}_\theta}{\partial r} - \dfrac{m}{r}Z_0\tilde{H}_r - jk\tilde{E}_z = \dfrac{I_m \delta(r-a)}{\epsilon_0 \pi a^{m+1}(1+\delta_{m0})} \ . \end{cases} \tag{2.76}$$

From these 8 equations, we first obtain two for the longitudinal components followed by two

for the radial components and another two for the azimuthal components:

$$\begin{cases} \dfrac{\partial \tilde{E}_z}{\partial r} = -\dfrac{m}{r} Z_0 \tilde{H}_z \ , \\ \dfrac{\partial Z_0 \tilde{H}_z}{\partial r} = -\dfrac{m}{r} E_z \ , \\ \dfrac{1}{r}\dfrac{\partial (r\tilde{E}_r)}{\partial r} - \dfrac{m}{r} Z_0 \tilde{H}_r = \dfrac{I_m \delta(r-a)}{\epsilon_0 \pi a^{m+1}(1+\delta_{m0})} + jk\left(1+\dfrac{m^2}{k^2 r^2}\right)\tilde{E}_z \ , \\ \dfrac{1}{r}\dfrac{\partial (r Z_0 \tilde{H}_r)}{\partial r} - \dfrac{m}{r}\tilde{E}_r = jk\left(1+\dfrac{m^2}{k^2 r^2}\right) Z_0 \tilde{H}_z \ , \\ Z_0 \tilde{H}_\theta = \tilde{E}_r + \dfrac{jm}{kr} Z_0 H_z \ , \\ \tilde{E}_\theta = -Z_0 \tilde{H}_r - \dfrac{jm}{kr}\tilde{E}_z \ . \end{cases} \tag{2.77}$$

The monopole mode ($m = 0$) is very special and deserves a special treatment. We find that ($\tilde{H}_z$, $\tilde{H}_r$, $\tilde{E}_\theta$) have nothing to do with the beam and are totally separated from ($\tilde{E}_z$, $\tilde{E}_r$, $\tilde{H}_\theta$). As a result, we can set ($\tilde{H}_z$, $\tilde{H}_r$, $\tilde{E}_\theta$) = 0. The solution becomes very simple:

$$\begin{aligned} \tilde{E}_z &= A_0 \ , & r < b \ , \\ \tilde{E}_r = Z_0 \tilde{H}_\theta &= \begin{cases} \dfrac{jkr}{2} A_0 \ , & r < a \ , \\ \dfrac{jkr}{2} A_0 + \dfrac{\rho_1}{2\pi\epsilon_0 r} \ , & a < r < b \ , \end{cases} \end{aligned} \tag{2.78}$$

where A_0 is a parameter dependent on the wave number k. Inside the metallic wall of the beam pipe ($r > b$), the Maxwell's equations become

$$\begin{cases} \dfrac{1}{r}\dfrac{\partial}{\partial r}\left(r\dfrac{\partial \tilde{E}_z}{\partial r}\right) = \left(\lambda_c^2 + \dfrac{m^2}{r^2}\right)\tilde{E}_z \ , \\ \dfrac{1}{r}\dfrac{\partial}{\partial r}\left(r\dfrac{\partial \tilde{H}_z}{\partial r}\right) = \left(\lambda_c^2 + \dfrac{m^2}{r^2}\right)\tilde{H}_z \ , \\ \tilde{E}_r = \dfrac{1}{Z_0\sigma_c}\left(\dfrac{m}{r} Z_0 \tilde{H}_z + \dfrac{\partial \tilde{E}_z}{\partial r}\right) \ , \\ \tilde{E}_\theta = -\dfrac{1}{Z_0\sigma_c}\left(\dfrac{m}{r}\tilde{E}_z + \dfrac{\partial Z_0 \tilde{H}_z}{\partial r}\right) \ , \\ Z_0 \tilde{H}_r = -\tilde{E}_\theta - \dfrac{jm}{kr}\tilde{E}_z \ , \\ Z_0 \tilde{H}_\theta = \tilde{E}_r - \dfrac{j}{k}\dfrac{\partial \tilde{E}_z}{\partial r} \ , \end{cases} \tag{2.79}$$

where $\lambda_c^2 = jkZ_0\sigma_c$. For the monopole mode, we have

$$\begin{cases} \tilde{E}_z = A_0 \dfrac{K_0(\lambda_c r)}{K_0(\lambda_c b)} \ , \\ \tilde{E}_r = A_0 \dfrac{jk}{\lambda_c} \dfrac{K_0'(\lambda_c r)}{K_0(\lambda_c b)} \ , \\ Z_0 \tilde{H}_\theta = A_0 \dfrac{j\lambda_c}{k} \left[-\dfrac{K_0'(\lambda_c r)}{K_0(\lambda_c b)} + \dfrac{k^2}{\lambda_c^2} \dfrac{K_0(\lambda_c r)}{K_0(\lambda_c b)} \right] \ , \end{cases} \tag{2.80}$$

where the continuity of $\tilde{E}_z$ across $r = b$ has been used. In above, K_0 is the modified Bessel function of order zero and the fields decay inside the metallic wall as $e^{\lambda_c(b-r)}$ since $\mathcal{R}e\, \lambda_c > 0$. Continuity of $\tilde{H}_\theta$ gives

$$A_0 = \frac{\dfrac{\rho_1}{2\pi\epsilon_0 b}}{\dfrac{j\lambda_c}{k}\left[-\dfrac{K_0'(\lambda_c b)}{K_0(\lambda_c b)} - \dfrac{k^2 b}{2\lambda_c} - \dfrac{k^2}{\lambda_c^2} \right]} = -\frac{\dfrac{\rho_1 c \mathcal{R}}{2\pi b}}{-\dfrac{K_0'(\lambda_c b)}{K_0(\lambda_c b)} + \dfrac{\mathcal{R}}{Z_0}\dfrac{jkb}{2} + \dfrac{\mathcal{R}^2}{Z_0^2}} \ , \tag{2.81}$$

where the denominator has been written in the order of decreasing importance and the impedance per square, $\mathcal{R} = \lambda_c/\sigma_c$ has been used. Thus the monopole coupling impedance per unit length of beam pipe is

$$\frac{Z_0^{\parallel}}{L} = -\frac{\tilde{E}_z}{\rho_1 c} = \frac{\mathcal{R}}{2\pi b} \frac{1}{-\dfrac{K_0'(\lambda_c b)}{K_0(\lambda_c b)} + \dfrac{\mathcal{R}}{Z_0}\dfrac{jkb}{2} + \dfrac{\mathcal{R}^2}{Z_0^2}} \ , \tag{2.82}$$

When $|\lambda_c b| \gg 1$ or the skin-depth is very much less than beam pipe radius, the asymptotic behavior of the modified Bessel functions can be used, namely, for any order m,

$$-\frac{K_m'(\lambda_c b)}{K_m(\lambda_c b)} = 1 + \frac{1}{2\lambda_c b} + \mathcal{O}(|\lambda_c b|^{-2}) \ . \tag{2.83}$$

The impedance becomes, for $kb \lesssim 1 \ll |\lambda_c| b$,

$$\frac{Z_0^{\parallel}}{L} = -\frac{\tilde{E}_z}{\rho_1 c} = \frac{\mathcal{R}}{2\pi b} \frac{1}{1 - \dfrac{\mathcal{R}}{Z_0}\left(\dfrac{j}{2kb} - \dfrac{jkb}{2} \right)} \ . \tag{2.84}$$

When the frequency is so low that $|\lambda_c b| \ll 1$,

$$\frac{K_0'(\lambda_c b)}{K_0(\lambda_c b)} = \frac{1}{\lambda_c b \ln(\lambda_c b/2)} \ , \tag{2.85}$$

and the impedance becomes

$$\frac{Z_0^{\parallel}}{L} = -j\frac{Z_0 k}{2\pi}\ln\frac{\lambda_c b}{2} \ , \tag{2.86}$$

which goes to zero as $k \to 0$.

Thus, for a smooth metallic wall when the skin-depth is much less than the pipe radius, it is safe to drop all higher order terms in $\mathcal{R}/Z_0$ to obtain $Z_0^{\parallel}/L = \mathcal{R}/(2\pi b)$.

For the higher azimuthal modes ($m > 1$), the longitudinal magnetic field is nonzero and is related to the longitudinal electric field. We write for $r < b$,

$$\begin{cases} \tilde{E}_z = A_m r^m \ , \\ Z_0\tilde{H}_z = -A_m r^m \ , \end{cases} \tag{2.87}$$

where A_m is a coefficient for the mth azimuthal mode depending on the wavenumber k. Now the radial components can be solved by noting that they must behave like r^{m-1}, r^{m+1}, and $r^{-(m+1)}$. The result is*

$$\begin{aligned} \tilde{E}_r &= \begin{cases} \dfrac{jkA_m r^{m+1}}{2(m+1)} + \dfrac{r^{m-1}}{2}\left[\dfrac{jmA_m}{k} + B_m - \dfrac{I_m}{\pi\epsilon_0 a^{2m}}\right] \ , & r < a \ , \\ \dfrac{jkA_m r^{m+1}}{2(m+1)} + \dfrac{r^{m-1}}{2}\left[\dfrac{jmA_m}{k} + B_m\right] + \dfrac{I_m}{2\pi\epsilon_0 r^{m+1}} \ , & a < r < b \ , \end{cases} \\ Z_0\tilde{H}_r &= \begin{cases} -\dfrac{jkA_m r^{m+1}}{2(m+1)} + \dfrac{r^{m-1}}{2}\left[-\dfrac{jmA_m}{k} + B_m - \dfrac{I_m}{\pi\epsilon_0 a^{2m}}\right] \ , & r < a \ , \\ -\dfrac{jkA_m r^{m+1}}{2(m+1)} + \dfrac{r^{m-1}}{2}\left[-\dfrac{jmA_m}{k} + B_m\right] - \dfrac{I_m}{2\pi\epsilon_0 r^{m+1}} \ , & a < r < b \ . \end{cases} \end{aligned} \tag{2.88}$$

*From the two equations for the radial fields in Eq. (2.77), $\tilde{E}_z \sim r^m$ and $\tilde{H}_z \sim r^m$ imply that $\tilde{E}_r$ and $\tilde{H}_r$ must have components in r^{m-1} and r^{m+1}. However, $\tilde{E}_r$ and $\tilde{H}_r$ may also contain other powers of r which cancel each other. The only possibility turns out to be r^{-m-1}. Thus $\tilde{E}_r = e_1 r^{m-1} + e_2 r^{m+1} + e_3 r^{-m-1}$ and $\tilde{Z}_0 H_r = h_1 r^{m-1} + h_2 r^{m+1} - e_3 r^{-m-1}$ when $a < r < b$, while $\tilde{E}_r = \bar{e}_1 r^{m-1} + \bar{e}_2 r^{m+1}$ and $\tilde{Z}_0 H_r = \bar{h}_1 r^{m-1} + \bar{h}_2 r^{m+1}$ when $r < a$. The two equations determine $e_1 = \bar{e}_1 = jkA_m/[2(m+1)]$, $h_1 = \bar{h}_1 = -jkA_m/[2(m+1)]$, and $e_2 - h_2 = \bar{e}_2 - \bar{h}_2 = jmA_m/k$. The continuity of $\tilde{H}_r$ and discontinuity of $\tilde{E}_r$ lead to two conditions, thus leaving one constant undetermined which we denote by B_m.

The azimuthal components are

$$\tilde{E}_\theta = \begin{cases} \dfrac{jkA_m r^{m+1}}{2(m+1)} + \dfrac{r^{m-1}}{2}\left[-\dfrac{jmA_m}{k} - B_m + \dfrac{I_m}{\pi\epsilon_0 a^{2m}}\right] , & r < a , \\ \dfrac{jkA_m r^{m+1}}{2(m+1)} + \dfrac{r^{m-1}}{2}\left[-\dfrac{jmA_m}{k} - B_m\right] + \dfrac{I_m}{2\pi\epsilon_0 r^{m+1}} , & a < r < b , \end{cases}$$

$$Z_0\tilde{H}_\theta = \begin{cases} \dfrac{jkA_m r^{m+1}}{2(m+1)} + \dfrac{r^{m-1}}{2}\left[-\dfrac{jmA_m}{k} + B_m - \dfrac{I_m}{\pi\epsilon_0 a^{2m}}\right] , & r < a , \\ \dfrac{jkA_m r^{m+1}}{2(m+1)} + \dfrac{r^{m-1}}{2}\left[-\dfrac{jmA_m}{k} + B_m\right] + \dfrac{I_m}{2\pi\epsilon_0 r^{m+1}} , & a < r < b . \end{cases} \tag{2.89}$$

In above, B_m is a new parameter to be determined. Inside the metallic wall of the beam pipe ($r > b$), the exact solution of the longitudinal field components is

$$\tilde{E}_z = -Z_0\tilde{H}_z = A_m b^m \frac{K_m(\lambda_c r)}{K_m(\lambda_c b)} , \tag{2.90}$$

where K_m is the modified mth order Bessel function of the second kind. Thus all the fields decay into the wall of the beam pipe as $e^{\lambda_c(b-r)}$. Although $\tilde{E}_z$ and $\tilde{H}_z$ appear to be independent in Eq. (2.79), however, they are connected through their continuities across the metallic surface into the vacuum area. The transverse components are:

$$\begin{cases} \tilde{E}_r = -\tilde{E}_\theta = \dfrac{jk}{\lambda_c}\left[\dfrac{K_m'(\lambda_c r)}{K_m(\lambda_c b)} - \dfrac{m}{\lambda_c r}\dfrac{K_m(\lambda_c r)}{K_m(\lambda_c b)}\right] A_m b^m , \\ Z_0\tilde{H}_\theta = -\left[\left(\dfrac{j\lambda_c}{k} - \dfrac{jk}{\lambda_c}\right)\dfrac{K_m'(\lambda_c r)}{K_m(\lambda_c b)} + \dfrac{jkm}{\lambda_c^2 r}\dfrac{K_m(\lambda_c r)}{K_m(\lambda_c b)}\right] A_m b^m , \\ Z_0\tilde{H}_r = \left[-\left(\dfrac{jkm}{\lambda_c^2 r} + \dfrac{jm}{kr}\right)\dfrac{K_m(\lambda_c r)}{K_m(\lambda_c b)} + \dfrac{jk}{\lambda_c}\dfrac{K_m'(\lambda_c r)}{K_m(\lambda_c b)}\right] A_m b^m . \end{cases} \tag{2.91}$$

Continuities of $\tilde{E}_\theta$ and $\tilde{H}_\theta$ give

$$A_m = \frac{\dfrac{I_m}{\pi\epsilon_0 b^{2m+1}}}{\dfrac{-j\lambda_c}{k}\dfrac{K_m'(\lambda_c b)}{K_m(\lambda_c b)} - \dfrac{jkb}{1+m} + \dfrac{jm}{kb}} . \tag{2.92}$$

The continuity of $\tilde{H}_r$ is redundant. The longitudinal coupling impedance per unit length of the mth azimuthal mode experienced by the beam becomes

$$\frac{Z_m^{\parallel}}{L} = -\frac{\tilde{E}_z(r)}{cI_m r^m} = \frac{\mathcal{R}}{\pi b^{2m+1}}\frac{1}{-\dfrac{K_m'(\lambda_c b)}{K_m(\lambda_c b)} + j\dfrac{\mathcal{R}}{Z_0}\left(\dfrac{kb}{1+m} - \dfrac{m}{kb}\right)} , \tag{2.93}$$

where $cI_m = \rho_1 c a^m$ is the mth multipole of the beam current. From Panofsky-Wenzel theorem, the transverse coupling impedance per unit length is[†] [‡]

$$\frac{Z_m^\perp}{L} = \frac{Z_m^\parallel}{kL} = \frac{\mathcal{R}}{\pi b^{2m+1}} \frac{1}{-\dfrac{K_m'(\lambda_c b)}{K_m(\lambda_c b)} + j\dfrac{\mathcal{R}}{Z_0}\left(\dfrac{kb}{1+m} - \dfrac{m}{kb}\right)} \ . \tag{2.94}$$

For frequencies that are very low or very high,

$$-\frac{K_m'(\lambda_c b)}{K_m(\lambda_c b)} = \begin{cases} \dfrac{m}{\lambda_c b} & |\lambda_c b| \ll 1 \ , \\ 1 & |\lambda_c b| \gg 1 \ . \end{cases} \tag{2.95}$$

We have

$$\frac{Z_m^\perp}{L} = \frac{Z_m^\parallel}{kL} = \begin{cases} \dfrac{Z_0}{2m\pi b^2} & |\lambda_c b| \ll 1 \ , \\ \dfrac{\mathcal{R}}{\pi k b^{2m+1}} & \lambda_c b| \gg 1 \ . \end{cases} \tag{2.96}$$

For the dipole mode ($m = 1$), in which we have special interest, we can work out the behavior of $\mathcal{R}e\, Z_1^\perp$ when the frequency is low. Since

$$-\frac{K_1'(x)}{K_1(x)} = \frac{1 + x^2 \ln x}{x} \ , \qquad |x| \ll 1 \ , \tag{2.97}$$

$$\frac{Z_1^\perp}{L} = \frac{Z_0}{2\pi b^2}\left[j - \frac{1}{2} k b^2 Z_0 \sigma_c \ln(k b^2 Z_0 \sigma_c)\right] \ , \qquad k b^2 Z_0 \sigma_c \ll 1 \ . \tag{2.98}$$

With the stainless steel conductivity $\sigma_c = 0.5 \times 10^7$ (Ω-m)$^{-1}$ and the beam pipe radius $b = 5$ cm, the critical frequency occurs at

$$kb = \frac{1}{Z_0 \sigma_c b} = 1.06 \times 10^{-8} \qquad \text{or} \qquad f_c = 10.1 \text{ Hz} \ . \tag{2.99}$$

The transverse dipole impedance is plotted in Fig. 4 from $kb = 10^{-12}$ to 10^2 or frequency $f = 0.01$ to 101 GHz. At high frequencies, we clearly see the $(kb)^{-1/2}$ behavior. At low frequencies, the imaginary part becomes constant while the real part decreases to zero linearly.

[†]It is clear that the term $kb/(1+m)$ in the denominator can only be important at very high frequencies. We find that it does not affect the plots in Fig. 4 even up to $kb \sim 10$ ($f = 10$ GHz). Thus this term can safely be deleted.

[‡]In Eq. (2.75) of Ref [2], the high-frequency expansion of $K_m'(\lambda_c b)/K_m(\lambda_c b)$ has already been made. Thus it cannot be used in the limit of low frequencies. In fact, if this limit were made blindly, one would obtain instead $Z_1^\perp/L = Z_0/(m\pi b^2)$, which is a factor of 2 too large.

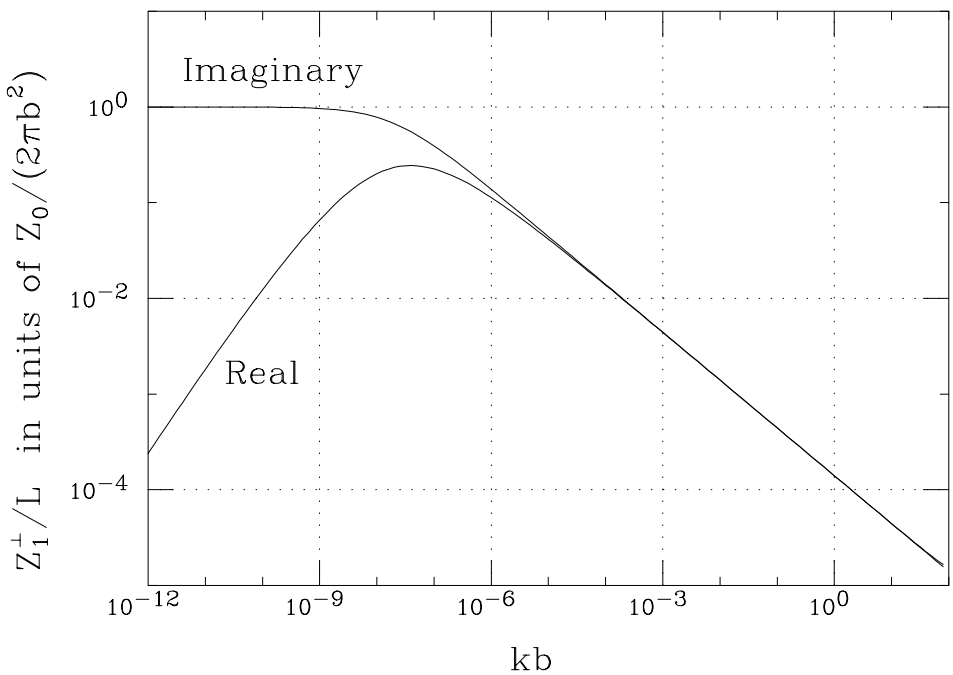

Figure 4: The real and imaginary parts of the transverse dipole impedance are shown as functions of kb for a beam pipe with radius $b = 5$ cm and wall conductivity $\sigma_c = 0.5 \times 10^7$ $(\Omega\text{-m})^{-1}$ (stainless steel). While both parts roll off as $(kb)^{-1/2}$ at high frequencies, the imaginary part approaches a constant at low frequencies and the real part falls to zero linearly.

The change of behavior takes place around $kb \sim 10^{-8}$ and 10^{-7} or $f \sim 10$ to 100 Hz. For a better conducting beam pipe wall, this change will take place at even lower frequencies. For this reason, this change of behavior is unimportant in the presence of a beam pipe with smooth resistive walls.

2.2.2 BYPASS INDUCTANCE

Consider a current I flowing in the z-direction displaced by $x = a$ as illustrated in the left plot of Fig. 5. When the metallic wall of the cylindrical beam pipe is a perfect conductor, the image current in the wall can be computed using the method of images. For a beam current I at an offset a on the x-axis, the magnetic field at the wall of the beam pipe can be made tangential with the positioning of an image current $-I$ on the x-axis b^2/a away from the center, as illustrated in Fig. 6. From the tangential magnetic field, the surface current

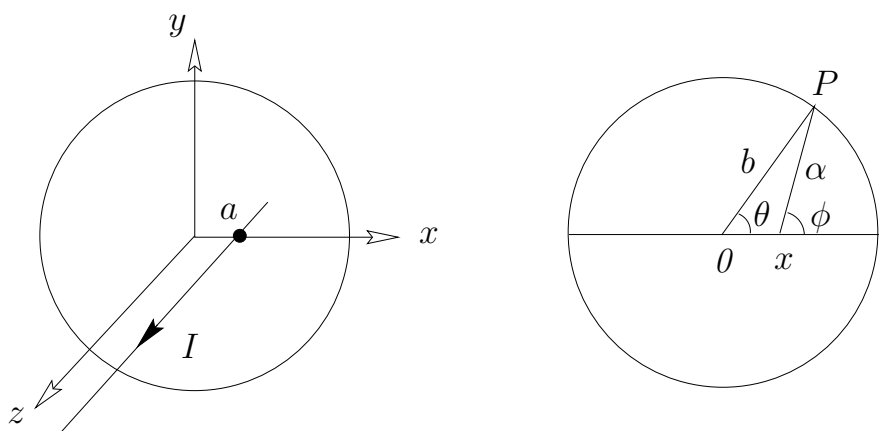

Figure 5: (a) A current I at an offset a on the x-axis of a perfectly conducting cylindrical beam pipe creates surface image current $J(\theta)$ on the inner surface of the beam pipe. For the dipole-mode image current, the uniform monopole image current is subtracted. (b) The image current in an element $\Delta(\theta)bd\theta$ at P produces a magnetic field at a point on the x-axis at a distance x from the origin.

density in the wall is found to be

$$K_z(\theta) = \frac{b^2 - a^2}{b^2 + a^2 - 2ba\cos\theta}\frac{I_b}{2\pi b} \ , \tag{2.100}$$

where $I_b = -I$ is the total image current in the metallic wall of the beam pipe flowing also in the *positive* z-direction. The normalization can be checked easily by integrating over the azimuthal angle θ. Since we are only interested in the dipole part of the image current, the monopole part, i.e., $K_z(\theta)$ with offset $a = 0$, must be subtracted, giving

$$K_z(\theta) - \frac{I_b}{2\pi b} = \frac{I_b}{2\pi b}\frac{2a(b\cos\theta - a)}{b^2 + a^2 - 2ba\cos\theta} \approx \frac{I_b a}{\pi b^2}\cos\theta \ , \tag{2.101}$$

where the last quantity is the dipole image current density and is denoted by $\Delta K_z(\theta)$. The total image current in one side ($-\pi/2 < \theta < \pi/2$) of the beam pipe is

$$I_d = \int_{-\pi/2}^{\pi/2} \Delta K_z(\theta) b d\theta = \frac{2I_b a}{\pi b} \ , \tag{2.102}$$

which is negative flowing in the positive z-direction. Of course, there is also a current $-I_d$ flowing in the positive z-direction between $\pi/2 < \theta < 3\pi/2$. This set of currents forms a dipole loop, and we called them the *differential currents*.

The dipole image current $\Delta K_z(\theta)$ sets up magnetic field inside the beam pipe. We are after this magnetic field on the x-axis ($-b < x < b$). By symmetry, the magnetic field there

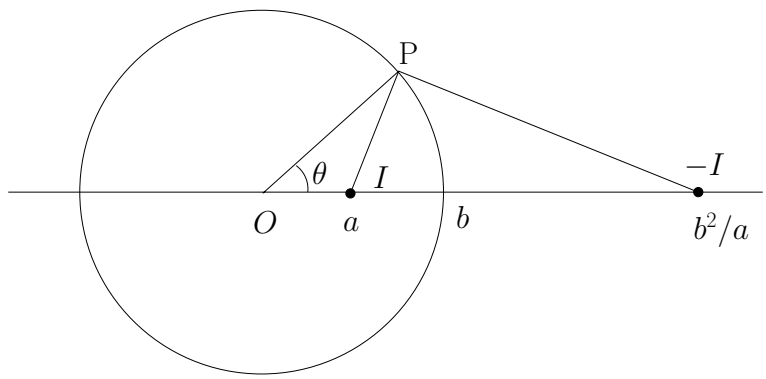

Figure 6: For a current I at an offset a on the x-axis, an image current $-I$ at a distance b^2/a from the center is required so that the magnetic field at any point P is tangential to the wall surface of the cylindrical beam pipe.

is in the vertical direction and is given by

$$H_y(x) = -\int_{-\pi}^{\pi} \frac{\Delta K_z(\theta) b d\theta}{2\pi\alpha} \cos\phi \ , \tag{2.103}$$

where, as illustrated in the right plot of Fig. 5, α is the distance between the point x and the image surface current element $\Delta K_z(\theta) b d\theta$ at Point P, and ϕ is the angle between the vector α and the x-axis. Point P is at a horizontal distance $b\cos\theta - x$ from the point of observation on the x-axis, and $\alpha^2 = b^2\sin^2\theta + (b\cos\theta - x)^2 = b^2 + x^2 - 2bx\cos\theta$. Notice that the image currents in all the four quadrants contribute to H_y in the same direction. This is expected because the image current just forms a loop. We can therefore write

$$H_y(x) = -\frac{I_b a}{\pi^2 b} \int_0^{\pi} \frac{(b\cos\theta - x)\cos\theta}{b^2 + x^2 - 2bx\cos\theta} d\theta = -\frac{I_b a}{2\pi b^2} \ , \tag{2.104}$$

which is independent of x as expected from a dipole source. The magnetic flux density is $B_y = \mu_0 H_y$ and the flux per longitudinal length linking the x-axis is

$$\Phi_y = \int_{-b}^{b} B_y dx = 2bB_y = -\frac{\mu_0 I_b a}{\pi b} = -\frac{\mu_0}{2} I_d \ . \tag{2.105}$$

Thus the inductance per longitudinal length facing the loop of differential currents (I_d at one side and $-I_d$ at the other side) is

$$\mathcal{L} = \frac{\mu_0}{2} \ , \tag{2.106}$$

which, in fact, is the result of the geometry of the system. We can therefore consider that the image current I_b and the differential current I_d are related through a mutual inductance

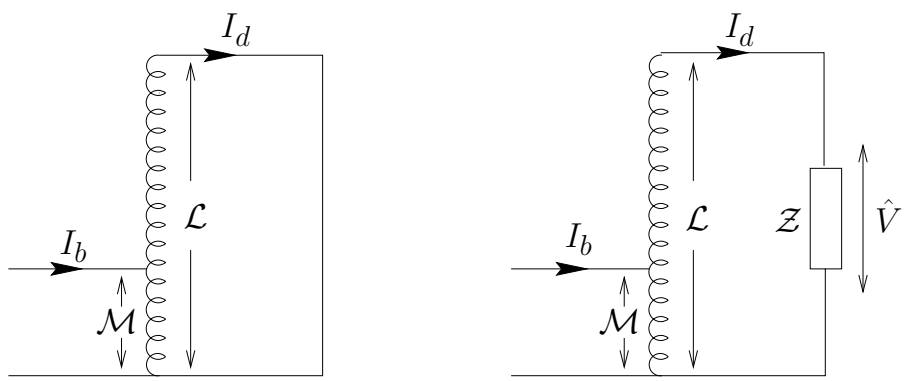

Figure 7: Left: Representing by an equivalent circuit, by offsetting the beam, the image current I_b generates, through a mutual inductance $\mathcal{M}$, a differential current I_d, which sees a inductance $\mathcal{L} = \mu_0/2$. Right: When the wall of the beam pipe is not perfectly conducting, the different current sees, in addition to the inductance $\mathcal{L}$, also an impedance $\mathcal{Z}$.

$\mathcal{M}$ as illustrated in the left equivalent circuit of Fig. 7. From

$$j\omega\mathcal{M}(I_b - I_d) = j\omega(\mathcal{L} - \mathcal{M})I_d \ , \tag{2.107}$$

it is easy to solve for the mutual inductance

$$\frac{\mathcal{M}}{\mathcal{L}} = \frac{I_d}{I_b} \ . \tag{2.108}$$

The horizontal force due to the image current acting on a charge in the beam is

$$F_x = e(E_x - \beta c B_y) \ , \tag{2.109}$$

where $v = \beta c$. The horizontal dipole impedance coming from this magnetic image is

$$\frac{Z_1^\perp}{L} = -\frac{(F_x/e)_{\text{mag}}}{jIa\beta} = \frac{cB_y}{jIa} = -j\frac{Z_0}{2\pi b^2} \ , \tag{2.110}$$

recalling that $I = -I_b$. This represents the familiar contribution from the magnetic image. The contribution of the electric image is just the same but is of opposite sign and is multiplied by the factor β^{-2}. The contribution of the self-force can also be included, because a beam of radius a_0 offset infinitesimally will have the dipole-mode current flowing along the edge of the beam in exactly the same distribution as Eq. (2.100) with I_b replaced by I and b replaced by a_0. Combining the electric- and magnetic-image contributions as well as the self-force contribution, one obtains

$$\frac{Z_1^H}{L} = -j\frac{Z_0}{2\pi\gamma^2\beta^2}\left(\frac{1}{a_0^2} - \frac{1}{b^2}\right) \ , \tag{2.111}$$

which is usually referred to as the transverse dipole *space-charge impedance*, where γ is the ratio of total energy to rest energy of the beam particles.

In the presence of wall resistivity, the differential currents, I_d and $-I_d$, see in addition to the inductance per length $\mathcal{L}$, an additional impedance per length $\mathcal{Z}$. Now Eq. (2.102) no longer holds because it is derived from the method of images into a perfectly conducting circular metallic wall. Nevertheless, Eq. (2.108), the relation between the inductance $\mathcal{L}$ and the mutual inductance $\mathcal{M}$ is still valid. Since we are still after the dipole mode,

$$\Delta K_z(\theta) = \frac{I_d}{2b}\cos\theta \quad \text{and} \quad \int_{-\pi/2}^{\pi/2} \Delta K_z(\theta) b d\theta = I_d \tag{2.112}$$

must hold. For a transverse width w and a longitudinal length L, the wall current is $w\Delta K_z(\theta)$, and the impedance is $\mathcal{R}L/w$. For a length L in the z-direction, the voltage difference created is given by

$$V(\theta) = 2\frac{\mathcal{R}L}{w} w\Delta K_z(\theta) \ , \tag{2.113}$$

or

$$V(\theta) = \frac{\mathcal{R}LI_d}{b}\cos\theta \ , \tag{2.114}$$

where the factor of 2 comes about because there is a negative surface current flowing on one side of the beam pipe and a negative surface current current flowing on the other side. The peak value occurs at $\theta = 0$, giving

$$\frac{\hat{V}}{L} = \frac{\mathcal{R}I_d}{b} = 2\pi\frac{Z_0^{\parallel}}{L} I_d \ , \tag{2.115}$$

where the expression for the longitudinal monopole impedance per unit length

$$\frac{Z_0^{\parallel}}{L} = \frac{\mathcal{R}}{2\pi b} \tag{2.116}$$

up to the lowest order in $\mathcal{R}$ has been used. In the equivalent circuit on the right plot of Fig 7, this peak voltage per unit length is just equal to the differential current I_d multiplied by the impedance $\mathcal{Z}$ represented in the circuit, thus giving a relation between $\mathcal{Z}$ and $Z_0^{\parallel}$, or

$$\mathcal{Z} = 2\pi\frac{Z_0^{\parallel}}{L} \ . \tag{2.117}$$

On the other hand, the peak electric field at the wall of the beam pipe is

$$\hat{E}_z = -\mathcal{R}H_\theta = \mathcal{R}\Delta K_z(0) = \frac{\mathcal{R}I_d}{2b} \ , \tag{2.118}$$

according to the definition of surface impedance per square, where H_θ is the azimuthal component of the magnetic field at the wall of the beam pipe. The horizontal Lorentz force per unit charge acting on the beam particle is

$$\frac{F_x}{e} = E_x - vB_y = -\frac{v}{j\omega}\frac{\partial E_z}{\partial x} \ . \tag{2.119}$$

For the dipole mode, E_z is linear[§] in x at $\theta = 0$; we therefore have

$$\frac{F_x}{e} = -\frac{v\mathcal{R}I_d}{2j\omega b^2} \ . \tag{2.120}$$

The horizontal dipole impedance is

$$\frac{Z_1^H}{L} = -\frac{F_x/e}{jIa\beta} = -\frac{c\mathcal{R}I_d}{2\omega b^2 Ia} = -\frac{c\pi}{\omega b}\frac{I_d}{Ia}\frac{Z_0^\parallel}{L} \ . \tag{2.121}$$

We need to derive the differential current I_d as related to I in the presence of wall resistivity. From the equivalent circuit depicted in the right plot of Fig. 7, it is easy to get

$$j\omega\mathcal{M}(I_b - I_d) = \left[j\omega(\mathcal{L} - \mathcal{M}) + \mathcal{Z}\right] I_d \ . \tag{2.122}$$

Using the inductance per length $\mathcal{L}$ and mutual inductance per length $\mathcal{M}$ derived in Eqs. (2.106) and (2.108), we obtain

$$\frac{I_d}{I_b} = \frac{2a}{\pi b}\frac{j\omega\mathcal{L}}{j\omega\mathcal{L} + \mathcal{Z}} \ , \tag{2.123}$$

and the ratio approaches the perfectly-conducting-wall limit when the wall resistivity $\mathcal{Z} \to 0$. Noting that $I_b = -I$, the horizontal dipole impedance is finally written as

$$\frac{Z_1^H}{L} = \frac{2c}{\omega b^2}\frac{\frac{j\omega\mathcal{L}}{2\pi}\frac{Z_0^\parallel}{L}}{\frac{j\omega\mathcal{L}}{2\pi} + \frac{Z_0^\parallel}{L}} = \frac{2c}{\omega b^2}\frac{\frac{j\omega\mu_0}{4\pi}\frac{Z_0^\parallel}{L}}{\frac{j\omega\mu_0}{4\pi} + \frac{Z_0^\parallel}{L}} \ , \tag{2.124}$$

where Eq. (2.117), the relation between $\mathcal{Z}$ and $Z_0^\parallel$, has been used. We see that when the frequency is not too small, we recover the usual Panofsky-Wenzel-like relation

$$Z_1^H \approx \frac{2c}{\omega b^2} Z_0^\parallel \ . \tag{2.125}$$

However, when the frequency is small, the horizontal dipole impedance approaches

$$\frac{Z_1^H}{L} \approx j\frac{Z_0}{2\pi b^2} \ , \tag{2.126}$$

[§]we can see this linearity in Eq. (2.87). For the two parallel plate, Eq. (2.36) does not show this linearity. This explains why we are not able to derive the bypass inductance for the parallel plates using this method.

which agrees with our low-frequency result in the previous section. The critical frequency occurs when

$$\frac{\omega Z_0}{4\pi c} = \left| \frac{Z_0^{\parallel}}{L} \right| , \tag{2.127}$$

or

$$\omega = \frac{2c}{b} \frac{|\mathcal{R}|}{Z_0} . \tag{2.128}$$

Let us try to understand the expression for the transverse dipole impedance. The transverse dipole impedance is essentially the voltage across the wall impedance $\mathcal{Z}$ in the right plot of Fig. 7 per dipole beam current Ia. The voltage across the wall resistivity is just $\mathcal{Z} I_d$. But we need to transform I_d to I_b because the impedance is the voltage seen by the beam current $-I_b$ not the differential current I_d. All the essence of the bend-around frequency lies in the transformation from the differential current I_d to the dipole beam current, and the transformation is given by Eq. (2.123). However, at high frequencies, this ratio is just

$$\frac{I_d}{I_b} \approx \frac{2a}{\pi b} , \tag{2.129}$$

which is the same ratio in the absence of the wall resistivity, according to Eq. (2.102). This result is easy to understand because the differential current will be smaller if the beam offset is smaller. We see that the inductance $\mathcal{L}$ does not even show up because high-frequency current finds it difficult to flow through an inductance. The transverse impedance is therefore just $\mathcal{Z}$, the wall resistivity, multiplied by the factor $c/(\pi\omega b^2)$, exactly the same as the usual Panofsky-Wenzel-like relation, aside from a constant. The situation is quite different at low frequencies, the no-wall-resistivity transformation ratio of Eq. (2.129) needs modification, because low-frequency current finds it easier to flow through an inductance $\mathcal{L}$ rather than the wall impedance $\mathcal{Z}$. Equation (2.123) gives

$$\frac{I_d}{I_b} \approx \frac{2a}{\pi b} \frac{j\omega\mathcal{L}}{\mathcal{Z}} , \tag{2.130}$$

making the differential current very small. The voltage across the wall impedance $\mathcal{Z}$ is now independent of $\mathcal{Z}$, and becomes proportional to $j\omega\mathcal{L}$. In short, the transverse dipole impedance is given totally by the geometric effect.

The above picture can be simplified by avoiding the differential current I_d and referring to the beam current I or its image I_b directly. The second factor in Eq. (2.124) represents an inductance $\mathcal{L}/(2\pi)$ in parallel with the longitudinal monopole impedance $Z_0^{\parallel}/L$. The transverse dipole impedance per unit length is just this parallel impedance multiplied by the

factor $2c/(\omega b^2)$. Thus we can imagine the dipole current flowing through this parallel circuit instead, as is illustrated in Fig. 8. We call the inductance, $\mathcal{L}/(2\pi)$, an *inductive bypass*, because, at low frequencies, the image current flows through this bypass instead of the wall impedance $\mathcal{Z}$. On the other hand, at high frequencies, the inductive bypass exhibits high reactance and the image current flows through $Z_0^{\parallel}$ instead.

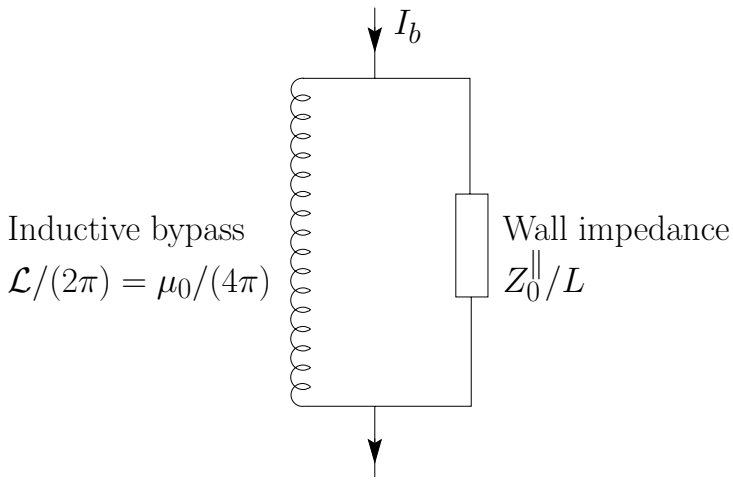

Figure 8: The image current sees an inductive bypass per unit length $\mathcal{L}/(2\pi) = \mu_0/(4\pi)$ in parallel with the longitudinal monopole wall impedance per unit length $Z_0^{\parallel}/L$. At low frequencies, the image current mostly flows through the bypass inductance, while at high frequencies, it mostly flows through the wall impedance.

2.2.3 OFF-AXIS BEAM

When the beam is at a large offset a from the center of the cylindrical beam pipe, the computation of the impedances experienced requires the knowledge of the longitudinal fields, which can be obtained by summing all the azimuthal modes, for example

$$E_z = \sum_{m=0}^{\infty} A_m r^m \cos m\theta \ ,$$
$$Z_0 H_z = -\sum_{m=0}^{\infty} A_m r^m \sin m\theta \ , \tag{2.131}$$

with the coefficients A_m given by Eq. (2.81) and (2.92). Since the offset can be comparable to the radius of the beam pipe, all azimuthal modes become important. Because the above

summations are nearly impossible, the expansion into azimuthal modes is not very helpful. We are going to solve for the fields experienced by the beam using the method of perturbation. The beam induces surface current on the surface of the beam pipe, which generates longitudinal electric field through wall resistivity. This resistivity-generated longitudinal electric field acts back on the particle beam, from which the impedances experienced can be computed. The only disadvantage of this method is that the result gives us only the lowest order in the surface impedance per square. Since only the lowest order of the perturbation is included, the results will not reflect the correct behavior at low frequencies. For example, the bend-around of the transverse impedance will be omitted.

The image current in the cylindrical wall of the beam pipe was given by Eq. (2.100) in the previous section using the method of images. Here we rewrite it as

$$K_z(\theta; a) = -\frac{I}{2\pi b}\frac{1-g^2}{1+g^2-2g\cos\theta} \ , \tag{2.132}$$

where $g = a/b$ represents the beam offset. The electric field generated at the wall surface is

$$E_z(\theta; a) = \mathcal{R} K_z(\theta; a) \tag{2.133}$$

where $\mathcal{R}$ is the surface impedance per square. Elsewhere, the longitudinal electric field $E_z(r, \theta; a)$ satisfies

$$\left[\nabla_\perp^2 + k^2 - k^2\beta^2\right] E_z(r, \theta; a) = 0 \ . \tag{2.134}$$

With the particle beam velocity equal to c, this is just the Laplace equation in two-dimension. The solution is

$$E_z(r, \theta; a) = \sum_{m=0}^{\infty} f_m r^m \cos m\theta \ . \tag{2.135}$$

When $r = b$, E_z must satisfy the boundary value of Eq. (2.133), from which coefficient f_m can be determined. The series can be summed easily to give

$$E_z(r, \theta; a) = -\frac{\mathcal{R} I}{2\pi b}\frac{1-(gr')^2}{1+(gr')^2-2(gr')\cos\theta} \ , \tag{2.136}$$

where the short-hand notion $r' = r/b$ has been used. At the beam position, $r' = g$ and $\theta = 0$,

$$E_z = -\frac{\mathcal{R} I}{2\pi b}\frac{1+g^2}{1-g^2} \ . \tag{2.137}$$

Therefore the longitudinal impedance for unit length due to the cylindrical resistive wall is

$$\frac{Z^\parallel}{L} = -\frac{\mathcal{R}}{2\pi b}\frac{1+g^2}{1-g^2} \ . \tag{2.138}$$

This expression can be checked by computing the average power consumed at the wall per unit length

$$\frac{P}{L} = \frac{1}{2}\int_0^{2\pi} \frac{1}{\sigma_c(b\delta_c d\theta)} |K_z b d\theta|^2 \ , \tag{2.139}$$

which equals $\frac{1}{2L}\mathcal{R}e\, Z^{\parallel}|I|^2$ as expected.

The horizontal impedance can be derived by generating a dipole current $I\Delta$ when the beam is shifted horizontally by a small amount Δ. The longitudinal electric field due to the resistivity of the wall by this dipole is obtained through differentiation of Eq. (2.136):

$$E_z'(r,\theta) = \frac{\partial E_z(r,\theta;a)}{\partial a}\Delta = \frac{\mathcal{R}I\Delta r'}{\pi b^2}\frac{2gr' - [1+(gr')^2]\cos\theta}{[1+(gr')^2 - 2(gr')\cos\theta]^2} \ . \tag{2.140}$$

The horizontal deflecting Lorentz force on a charge on the x-axis is

$$\frac{F_H}{e} = E_r' - Z_0 H_\theta' = -\frac{1}{jk}\frac{\partial E_z'}{\partial r} = \frac{\mathcal{R}I\Delta}{jk\pi b^3}\frac{1+gr'}{(1-gr')^3} \ , \tag{2.141}$$

where Faraday's law has been used. The horizontal impedance per unit length is therefore

$$\frac{Z^H}{L} = -\frac{F_H/e}{jI\Delta} = \frac{\mathcal{R}}{\pi k b^3}\frac{1+g^2}{(1-g^2)^3} \ . \tag{2.142}$$

This same Z^H can also be obtained by equating the average power consumed by the beam dipole per unit length

$$\frac{P}{L} = \frac{1}{2L}k|I\Delta|^2\,\mathcal{R}e\, Z^H \tag{2.143}$$

to the average power consumed at the wall per unit length

$$\frac{P}{L} = \frac{1}{2}\int_0^{2\pi} \frac{1}{\sigma_c(\delta_c b d\theta)} \left|K_z' b d\theta\right|^2 \ , \tag{2.144}$$

where $K_z'(\theta)$, the surface current density due to the horizontal dipole current, is obtained by differentiating Eq. (2.132) with respect to a, i.e.,

$$K_z'(\theta) = \frac{\partial K(\theta;a)}{\partial a}\Delta \ . \tag{2.145}$$

The vertical impedance experienced by the beam can be derived by shifting the beam vertically upward by the amount Δ, thus creating a vertical dipole current $I\Delta$. This can be accomplished by differentiating the resistivity-generated electric field in Eq. (2.136) with respect to θ. The longitudinal electric field due to the vertical dipole is then

$$E_z'(r,\theta) = \frac{\partial E_z(r,\theta;a)}{\partial\theta}\frac{\Delta}{r} = \frac{\mathcal{R}I\Delta g}{\pi b^2}\frac{\left[1-(gr')^2\right]\sin\theta}{\left[1+(gr')^2 - 2(gr')\cos\theta\right]^2} \ . \tag{2.146}$$

The vertical Lorentz force acting on a particle is

$$\frac{F_V}{e} = E'_\theta + Z_0 H'_r = -\frac{1}{jkr}\frac{\partial E'_z}{\partial \theta} = \frac{\mathcal{R} I \Delta g}{\pi b^3}\frac{\left[1-(gr')^2\right]\left\{\left[1+(gr')^2\right]\cos\theta - 2gr'\right\}}{\left[1+(gr')^2-2(gr')\cos\theta\right]^3} \ , \quad (2.147)$$

where Faraday's law has been used. With this force evaluated at the dipole, we obtain the vertical impedance per unit length

$$\frac{Z^V}{L} = -\frac{F_V/e}{jI\Delta} = \frac{\mathcal{R}}{\pi k b^3}\frac{1+g^2}{\left(1-g^2\right)^3} \ , \quad (2.148)$$

which is exactly the same as the horizontal impedance Z^H in Eq. (2.142). The same Z^V can be obtained by equating the average power consumed by the beam dipole per unit length

$$\frac{P}{L} = \frac{1}{2L}k|I\Delta|^2 \, \mathcal{R}e \, Z^V \quad (2.149)$$

to the average power consumed at the wall per unit length

$$\frac{P}{L} = \frac{1}{2}\int_0^{2\pi} \frac{1}{\sigma_c(\delta_c b d\theta)}\left[K'_z(\theta) b d\theta\right]^2 \ , \quad (2.150)$$

where $K'_z(\theta)$, the surface current density due to the vertical beam dipole, is obtained by differentiating Eq. (2.132) with respect to θ, i.e.,

$$K'_z(\theta) = \frac{\partial K_z(\theta; a)}{\partial \theta}\frac{\Delta}{a} \ . \quad (2.151)$$

3 CRACK IMPEDANCE

3.1 PARALLEL-FACE MAGNET

In former sections, we have derived the impedances experienced by the beam in terms of the surface impedance per square $\mathcal{R}$. Here, we are going to compute this surface impedance per square for the laminated surface. First let us consider the parallel-face laminated magnet, which consists of laminations from $y = \pm b$ to $y = \pm d$ extending to infinity in the x-direction. The beam is considered to be a sheet current flowing in the z-direction at $y = 0$. This simplifies the problem because it has been reduced to two-dimensional. We further assume the laminations to be shorted at the far ends at $y = \pm d$. The laminations are to have thickness τ (called region 2) and separated by cracks of width h (called region 1). One of

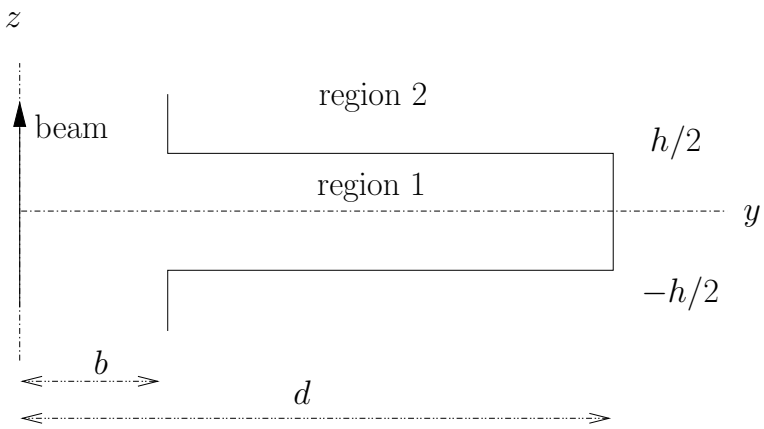

Figure 9: A sheet current ($-\infty < x < \infty$) flows in the z-direction at $y = 0$. The x-direction is pointing out of the paper. A crack with two adjacent laminations shorted at the $y = d$ is shown.

the cracks is shown in Fig. 9, where the x-axis is pointing out of the paper and the plane $z = 0$ is at the center of the crack. We wish to compute the longitudinal electric field across the crack. We will be using the typical properties of the laminations and cracks as listed in Table II.

Table II: Some typical properties of the laminations and cracks.

	crack	lamination
Width or thickness	$h = 0.000375''$	$\tau = 0.025''$
Relative magnetic permittivity	$\mu_{1r} = 1$	$\mu_{2r} = 100$
Relative dielectric	$\epsilon_{1r} = 4.75$	$\epsilon_{2r} = 1$
Conductivity	$\sigma_{c1} = 1.0 \times 10^{-3}$ $(\Omega\text{-m})^{-1}$	$\sigma_{c2} = 0.5 \times 10^{7}$ $(\Omega\text{-m})^{-1}$

Notice that the longitudinal electric field satisfies the Laplace equation

$$\left(\nabla^2 - \omega^2\mu\epsilon\right)E_z(y,z) = 0 \ , \tag{3.1}$$

where the electric permittivity ϵ should be replaced by

$$\epsilon \to \epsilon\left(1 + \frac{\sigma_c}{j\omega\epsilon}\right) \tag{3.2}$$

in order to include conductivity. Since electromagnetic fields have to decay inside the laminations, we choose

$$\frac{\partial^2\vec{E}}{\partial z^2} = g^2\vec{E} \ , \quad \frac{\partial^2\vec{H}}{\partial z^2} = g^2\vec{H} \ , \tag{3.3}$$

with g real and positive. Notice that we have the same g for both $\vec{E}$ and $\vec{H}$, because one can be obtained from the other through an application of curl. The Laplace equation now becomes

$$\left(\frac{\partial^2}{\partial y^2} + q^2\right) E_z = 0 \ . \tag{3.4}$$

with

$$q^2 = \omega^2 \mu\epsilon + g^2 \ . \tag{3.5}$$

Since q is now nonzero, the transverse field components can be obtained by

$$\begin{cases} E_y = \dfrac{1}{q^2}\dfrac{\partial^2 E_z}{\partial y \partial z} \ , \\ H_x = \dfrac{j\omega\epsilon}{q^2}\dfrac{\partial E_z}{\partial y} \ . \end{cases} \tag{3.6}$$

The fields in regions 1 and 2 are written as

$$\begin{array}{ll} \text{Region 1:} \\ |z| < h/2 \end{array} \quad \begin{cases} E_z = A\cosh(g_1 z)\Big[\sin(qy) + \alpha\cos(qy)\Big] \ , \\ E_y = \dfrac{g_1 A}{q}\sinh(g_1 z)\Big[\cos(qy) - \alpha\sin(qy)\Big] \ , \\ H_x = \dfrac{j\omega\epsilon_1 A}{q}\cosh(g_1 z)\Big[\cos(qy) - \alpha\sin(qy)\Big] \ , \end{cases}$$

$$\begin{array}{ll} \text{Region 2:} \\ |z| > h/2 \end{array} \quad \begin{cases} E_z = B\, e^{-g_2|z|}\Big[\sin(qy) + \alpha\cos(qy)\Big] \ , \\ E_y = -\dfrac{g_2 B}{q}\,\mathrm{sgn}(z)\, e^{-g_2|z|}\Big[\cos(qy) - \alpha\sin(qy)\Big] \ , \\ H_x = \dfrac{\sigma_{2c} B}{q}\, e^{-g_2|z|}\Big[\cos(qy) - \alpha\sin(qy)\Big] \ . \end{cases} \tag{3.7}$$

Some comments are in order:

1. Region 2 is the lamination with $\mu_{2r} = 100$, $\epsilon_{2r} = 1$, and $\sigma_{2c} = 0.5 \times 10^7$ $(\Omega\text{-m})^{-1}$. We have

$$\epsilon_2 \to \epsilon_2\left(1 + \frac{\sigma_{2c}}{j\omega\epsilon_2}\right) \ , \tag{3.8}$$

where the second term in the bracket decreases from unity only when $\omega/(2\pi)$ reaches 0.9×10^{17} Hz. Thus the first term can be neglected, which amounts to neglecting the displacement current. Hence we have H_x in the last line the substitution

$$\epsilon_2 \to \frac{\sigma_{2c}}{j\omega} \ . \tag{3.9}$$

2. Because E_y and H_x have to be continuous across the surfaces at $z = \pm h/2$, the y-dependency should be the same in the two regions. Thus we have the same arguments qy of sine and cosine in the two regions and the same constant α for their ratios.

3. Because the beam current is flowing in the z-direction, E_z is even in z. The image current is flowing into the crack along the upstream lamination wall at $z = -h/2$ in the positive y-direction, but flowing out of the crack along the downstream lamination wall at $z = h/2$ in the negative y-direction. Therefore E_y should be odd in z.

4. This field assignment assumes that the fields do not penetrate through the lamination. In other words, the skin-depth δ_{2c} is less than the the lamination thickness τ. As a result, the model is valid when the frequency

$$f \gtrsim \frac{c}{\pi Z_0 \sigma_{2c} \mu_{2r} \tau^2} = 1.26 \text{ kHz} , \tag{3.10}$$

which is only a small fraction of the revolution frequencies of the Fermilab machines as listed in Table III. Thus the approximation made so far should be valid in a very wide range of frequencies

$$1.26 \text{ kHz} \ll f \ll 10^6 \text{ GHz} . \tag{3.11}$$

Table III: Revolution frequencies of Fermilab machines.

	Rev. Freq. (kHz)
Booster at 400 MeV (K.E.)	450.796
Main Injector at 8 GeV (K.E.)	89.816
Tevatron at 150 GeV	47.713

Now let us give an estimate of the parameters q, $k_{1,2}$, and $g_{1,2}$. We have

$$\begin{aligned} q^2 &= k_1^2 + g_1^2 , \\ q^2 &= k_2^2 + g_2^2 , \\ k_1^2 &= \omega^2 \mu_1 \epsilon_1 , \\ k_2^2 &= \omega^2 \mu_2 \epsilon_2 = -\frac{2j}{\delta_{2c}^2} , \end{aligned} \tag{3.12}$$

where $\delta_{2c} = \sqrt{2/(\omega\mu_2\sigma_{2c})}$ is the skin-depth into the lamination. Notice that

$$\frac{k_1^2}{k_2^2} = -\frac{\omega}{jcZ_0\sigma_{2c}}\frac{\epsilon_{1r}}{\mu_{2r}} \to j\frac{2}{3}\times 10^{-9} \quad \text{when } \frac{\omega}{2\pi} = 1 \text{ GHz} . \tag{3.13}$$

If the lamination were perfectly conducting, we would expect $g_1 = 0$. We therefore expect $g_1 h \ll 1$. Since E_z must vanish when $y = d$, we can solve for

$$\alpha = -\tan qd . \tag{3.14}$$

Thus, $qd \sim \mathcal{O}(1)$. We have at 1 GHz with $\epsilon_{1r} = 4.75$,

$$k_1^2 = 2068 \text{ m}^{-2} , \quad k_2^2 = -\frac{2j}{\delta_{2c}^2} = 3.95\times 10^{12} \text{ m}^{-2} . \tag{3.15}$$

In addition, with the crack width $h = 0.000375''$,

$$g_1^2 \ll \frac{1}{h^2} = 10^{10} \text{ m}^{-2} , \quad q^2 \sim \mathcal{O}\left(\frac{1}{d^2}\right) \sim \mathcal{O}(100) \text{ m}^{-2} . \tag{3.16}$$

Since $|k_2|^2 \gg |q|^2$, we expect

$$g_2^2 \sim -k_2^2 = \frac{2j}{\delta_{2c}^2} \quad \text{or} \quad g_2 = \frac{1+j}{\delta_{2c}} . \tag{3.17}$$

This root is chosen to ensure decay inside the lamination. Continuities of E_y and H_x across $z = h/2$ give

$$\frac{A}{B} = -\frac{g_2 e^{-g_2 h/2}}{g_1 \sinh(g_1 h/2)} = \frac{\sigma_{2c} e^{-g_2 h/2}}{j\omega\epsilon_1 \cosh(g_1 h/2)} . \tag{3.18}$$

We get

$$g_1 \tanh(g_1 h/2) = -\frac{j\omega\epsilon_1 g_2}{\sigma_{2c}} , \tag{3.19}$$

or, for $g_1 h \ll 1$,

$$g_1^2 = -\frac{j2\omega\epsilon_1 g_2}{\sigma_{2c} h} = (1-j)k_1^2\frac{\mu_2}{\mu_1}\frac{\delta_{2c}}{h} . \tag{3.20}$$

We have evaluated up to 1 GeV, the parameters $|q^2|$, $|k_1^2|$, $|k_2^2|$, $|g_1^2|$, and $|g_2^2|$ according to the properties of the laminations and crack medium listed in Table II. The results are plotted in Fig. 10. Here, we see clearly how much $|k_2^2|$ and $|g_2^2|$ are larger than $|q^2|$ and $|g_1^2|$. The smallest is $|k_1^2|$.

We are now in the position to define the crack surface impedance $\mathcal{R}_c$ per square:

$$\frac{\mathcal{R}_c}{Z_0} = \frac{E_z(b)}{Z_0 H_x(b)} = -\frac{jq}{\epsilon_{1r}k}\frac{\sin qb\cos qd - \sin qd\cos qb}{\cos qb\cos qd + \sin qd\sin qb} = \frac{jq}{\epsilon_{1r}k}\tan q(d-b) . \tag{3.21}$$

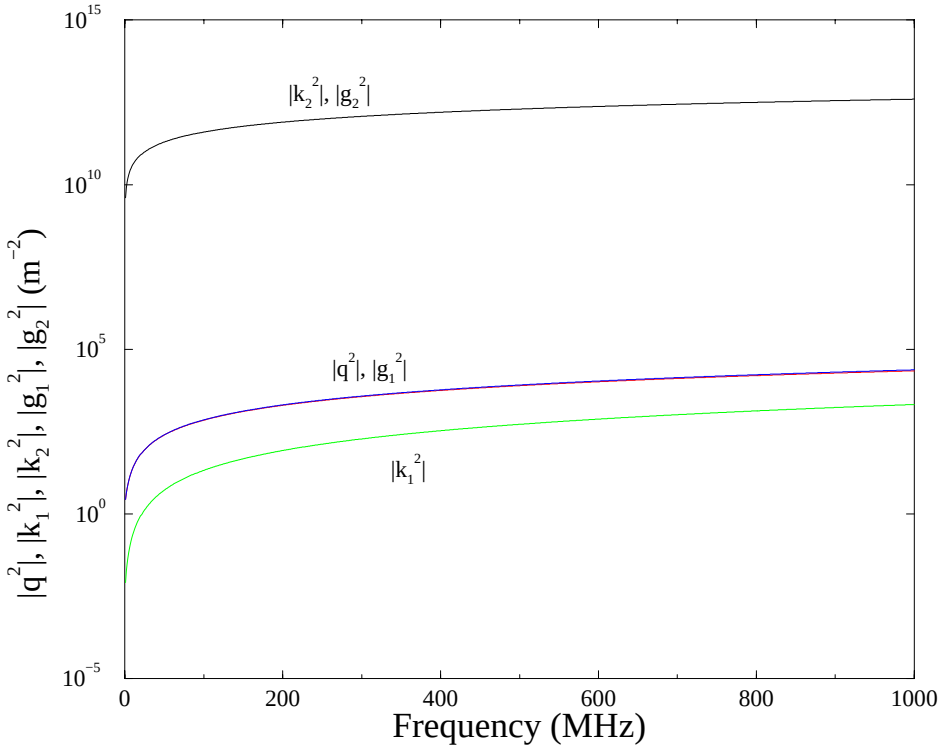

Figure 10: Plot of $|q^2|$, $|k_1^2|$, $|k_2^2|$, $|g_1^2|$, and $|g_2^2|$, showing that $|g_2^2| \sim |k_2^2| \gg |g_1^2| \sim |k^2| \gg |k_1^2|$.

This quantity has a physical meaning, because $H_x(b)$ is equal to the surface current per width flowing into the crack at $y = b$ while $hE_z(b)$ represents the potential produced across the crack at $y = b$. Part of the time the particle beam is seeing the cracks and part of the time seeing the edges of the laminations. The surface impedance per square for the latter is given by

$$\frac{\mathcal{R}_L}{Z_0} = \frac{1+j}{\sigma_{2c}\delta_{2c}Z_0} = (1+j)k\delta_{2c}\mu_{2r} \ , \tag{3.22}$$

where $k = \omega/c$. The surface impedance per square of the laminated wall in the z-direction is therefore obtained by the weighted average,

$$\mathcal{R}_z = \frac{\mathcal{R}_c\tau + \mathcal{R}_L h}{\tau + h} \ . \tag{3.23}$$

As will be shown below, the lamination part of the impedance is very much less than the crack part, and we can approximate

$$\mathcal{R}_z = \frac{\mathcal{R}_L h}{\tau + h} \ , \tag{3.24}$$

which is to be substituted in Eqs. (2.48), (2.58), (2.62), (2.64), (2.67), and (2.69) for the evaluation of the different impedances experienced by the beam. In the next subsections,

we are going to study the behavior of the crack surface impedance at different frequency regimes in order to have a better understanding of its physical meaning.

3.1.1 LOW-FREQUENCY BEHAVIOR

From Eqs. (3.12) and (3.20),

$$q^2 = k_1^2 \left[1 + (1-j)\frac{\mu_2 \delta_{2c}}{\mu_1 h}\right] = \frac{\omega^2}{c^2}\mu_{1r}\epsilon_{1r}\left[1 + (1-j)\frac{\mu_2 \delta_{2c}}{\mu_1 h}\right] \ . \tag{3.25}$$

As $\omega \to 0$, $\delta_{2c} \to \omega^{-1/2}$, $\epsilon_{1r} \to \omega^{-1}$. Thus $q^2 \to \sqrt{\omega}$. The crack impedance per square becomes

$$\frac{\mathcal{R}_c}{Z_0} \to \frac{jcq^2}{\omega\epsilon_{1r}}(d-b) = (1+j)\frac{\delta_{2c}\omega}{hc}\mu_{2r}(d-b) \ . \tag{3.26}$$

Note that ϵ_{1r} gets cancelled. In other words, $\mathcal{R}_c$ behaves as $(1+j)\sqrt{\omega}$ in exactly the same way as the impedance due to skin depth into the laminations. This result is not unexpected, because the impedance going in and out of a width w of a crack via the lamination skin-depth is

$$\frac{\text{Imp of 1 crack}}{Z_0} = \frac{2}{Z_0}\int_b^d \frac{(1+j)}{\delta_{2r}\sigma_{2r}}\frac{dy}{w} = (1+j)\frac{\omega\delta_{2c}\mu_{2r}}{wc}(d-b) \ , \tag{3.27}$$

where the factor 2 before the integral sign appears because the current flows into the crack along the surface of one lamination and flows out along the surface of the next lamination. The crack impedance per square is obtained by multiplying the above impedance by w and dividing by the crack width h, arriving at exactly the expression in Eq. (3.26).

We can use the low-frequency approximation of the crack impedance to estimate a bend-around frequency for the transverse dipole impedance of the laminated magnet. First, the surface impedance per square of the laminated wall in the z direction is, from Eq. (3.23), $\mathcal{R}_z \approx \mathcal{R}_c h/\tau$, where $\mathcal{R}_c$ is given by Eq. (3.26). Then, using Eq. (2.48), the criterion in Eq. (1.3) translates into

$$1 \approx |1+j|\frac{2\delta_{2c}\mu_{2r}}{\tau}\frac{d-b}{b} \ , \tag{3.28}$$

which is equivalence of Eq. (1.6) when the laminated magnet wall has parallel-face cross-section. With $b = 5$ cm and $d - b = 10$ cm, and the other parameters as given by Table II, the bend-around frequency is roughly 400 MHz. This estimation has been too high because we have used the low-frequency approximation of $\mathcal{R}_c$ in a situation where the frequency is not too low.

3.1.2 HIGH-FREQUENCY BEHAVIOR

From Eq. (3.25), we see that

$$\lim_{\omega\to\infty} q = \lim_{\omega\to\infty} k_1 = \frac{\omega}{c}\sqrt{\epsilon_{1r}} \ , \tag{3.29}$$

where $\epsilon_{1r} = 4.75$ is the dielectric constant[¶] of the medium filling the crack. Thus the crack impedance per square approaches

$$\frac{\mathcal{R}_c}{Z_0} \to \frac{j}{\sqrt{\epsilon_{1r}}} \tan q(d-b) \ . \tag{3.30}$$

One may be afraid of blowups at high frequencies when the tangent in Eq. (3.30) is equal to odd multiples of $\pi/2$, because the argument $q(d-b)$ becomes almost real. However, this does not happen because the imaginary part of q^2 in Eq. (3.25) decreases very slowly as $\omega^{-1/2}$. For example, when the frequency reaches 1×10^6 GHz, $\mathcal{I}m\, q$ still remains $\sim 0.5\%$ of $\mathcal{R}e\, q$. Since $\mathcal{R}e\, q \sim \sqrt{\epsilon_{1r}}\omega/c$, $\mathcal{I}m\, q(d-b)$ is a large negative number which damps out all the resonances. In fact,

$$\tan q(d-b) = \frac{\tan[\mathcal{R}e\, q(d-b)] + j\tanh[\mathcal{I}m\, q(d-b)]}{1 - j\tan[\mathcal{R}e\, q(d-b)]\tanh[\mathcal{I}m\, q(d-b)]} \to -j \ , \tag{3.31}$$

even when $\omega/(2\pi) \gtrsim 200$ MHz because $\tanh[\mathcal{I}m\, q(d-b)] \to -1$. As a result, the crack impedance per square approaches the limit $\epsilon_{1r}^{-1/2} Z_0 \sim 173\ \Omega$.

Since we are not interested in frequencies reaching tens or hundreds GHz's, we would like to study the behavior of the crack impedance per square when the second term (the δ_{2c} term) in Eq. (3.25) dominates or when $|g_1|^2 \gg |k_1|^2$. Numerically, this occurs when the frequency is $f \ll 100$ GHz. Substitution into Eq. (3.21) leads to

$$\frac{\mathcal{R}_c}{Z_0} = \sqrt{1+j}\sqrt{\frac{\mu_{2r}}{\epsilon_{1r}}}\sqrt{\frac{\delta_{2c}}{h}} \ , \tag{3.32}$$

where $\tan q(d-b) \approx -j$ has been used. Thus in this range of frequencies, the crack impedance per square rolls off as $\omega^{-1/4}$.

3.1.3 LAMINATIONS VERSUS CRACKS

The particle beam is seeing both the cracks and the edge of the laminations. As frequency increases, the crack surface impedance per square $\mathcal{R}_c$ decreases slowly as $\omega^{-1/4}$ (for

[¶]The conductivity dependent part rolls off as $f \gg 3.8$ MHz because the medium in the crack is almost an insulator.

$\omega/(2\pi) \ll 100$ GHz), while the lamination surface impedance per square $\mathcal{R}_L$ increases as $\omega^{1/2}$ because the skin-depth becomes smaller and smaller. At some frequency, the contribution of the lamination surface impedance will dominate over the crack surface impedance. This occurs when

$$\frac{1+j}{\delta_{2c}\sigma_{2c}}\tau > \sqrt{1+j}\sqrt{\frac{\mu_{2r}}{\epsilon_{1r}}}\sqrt{\frac{\delta_{2c}}{h}}h \ , \tag{3.33}$$

where the the left side is $\mathcal{R}_L$ weighted by the lamination thickness τ and the right side is $\mathcal{R}_c$ from Eq. (3.32) weighted by the crack width h. It is easy to re-express this as

$$\omega^{3/4} > \frac{2c}{\sqrt{1+j}}\sqrt{\frac{h}{\epsilon_{1r}\tau^2}}\left(\frac{Z_0\sigma_{2c}}{2c\mu_{2r}}\right)^{1/4} \ . \tag{3.34}$$

This critical frequency is $\omega/(2\pi) \approx 58.8$ GHz. Since we are not interested in such high frequencies, it is safe to neglect $\mathcal{R}_L$ and write the weighted surface impedance $\mathcal{R}_z$ as in Eq. (3.24).

The comparison with $\mathcal{R}_L$ raises another problem. Why would $\mathcal{R}_c$ not increase as frequency just as what happens with $\mathcal{R}_L$? Physically, the image current flows across a crack in two ways. One is to flow into the crack along the surface of one lamination and come back along the surface of the next lamination. The other way is to flow across the crack directly as *displacement current*. The process can be represented by a resistor plus an inductor in parallel with a capacitor. As frequency increases, it will become harder and harder to flow along the laminations because the skin-depth becomes thinner and thinner (or the equivalent resistor and inductor become larger and larger). Thus more and more current will flow across the crack as displacement current (or going through the equivalent capacitor). For this reason, the reactive impedance of the crack behaves capacitively at high frequencies.

The crack surface impedance per square $\mathcal{R}_c$ of a beam inside a Booster D-magnet is computed and its real and imaginary parts are shown in Fig. 11 as solid curves. The combined-function magnet is approximated as parallel-face, with a gap $2b = 2.25''$ and total height $2d = 12''$. Other properties of the laminations and cracks are listed in Table II. We see that both the real and imaginary parts of the crack surface impedance behave as $\sqrt{\omega}$ at low frequencies. There is a first broad resonance at $\omega/(2\pi) \approx 33$ MHz and a second one at 140 MHz. These resonances are heavily damped because of the resistive nature of the laminations. The imaginary part first starts out as inductive, but becomes capacitive after the first broad resonance, verifying that the image current crosses the crack as displacement current at high frequencies. The dashed curves represent the crack surface impedance per square for an annular laminated magnet discussed in the next section.

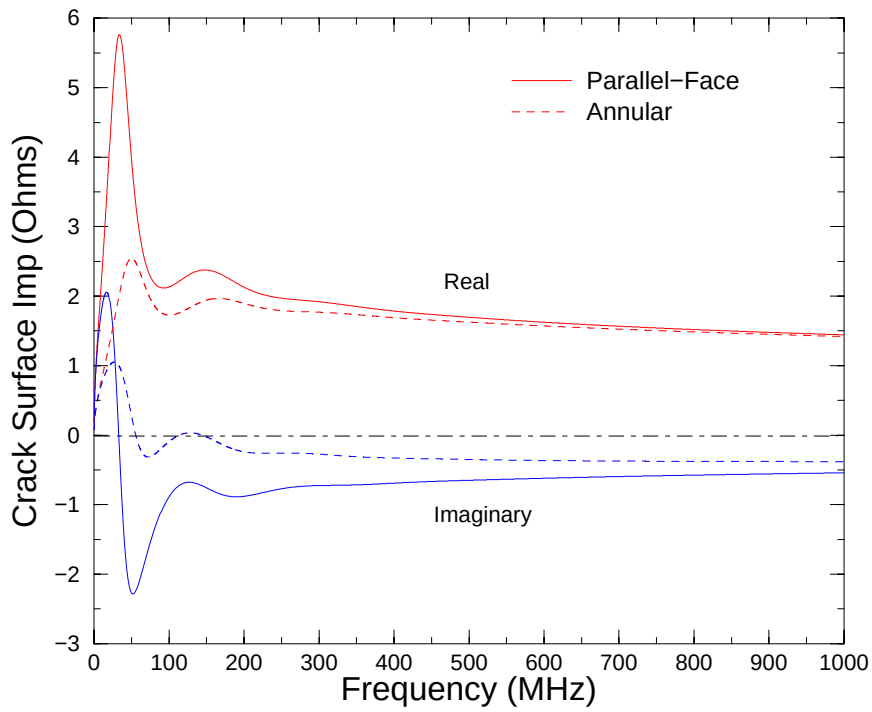

Figure 11: Crack surface impedances per square $\mathcal{R}_c$ for parallel-face magnet (solid) and annular magnet (dashed) with laminations shorted at $d = 6.0$ in from the beam and pole faces separated by $2b = 2.25$ in.

3.2 ANNULAR-RING MAGNET

A Lambertson magnet can be approximated by a laminated annular-ring magnet of inner radius b and outer radius d where the laminations are assumed to be shorted. The particle beam is at the center of the annular magnet during acceleration and storage, and will be shifted to near the laminated surface for injection and extraction. In the Sec. 2.2, we have computed the impedances experienced by the beam at the center axis and also at a large offset in terms of the surface impedance per square. In this section, we are going to derive the surface impedance per square. This surface impedance was first derived by Snowdon [6] and later by Gluckstern [7]. We merely include the derivation here with our comments for the sake of completeness. There are also derivations of this impedance by considering the crack as a radial transmission line. [8, 9] The results are comparable.

The sketch of the beam passing one crack of the laminated surface is shown in Fig. 12.

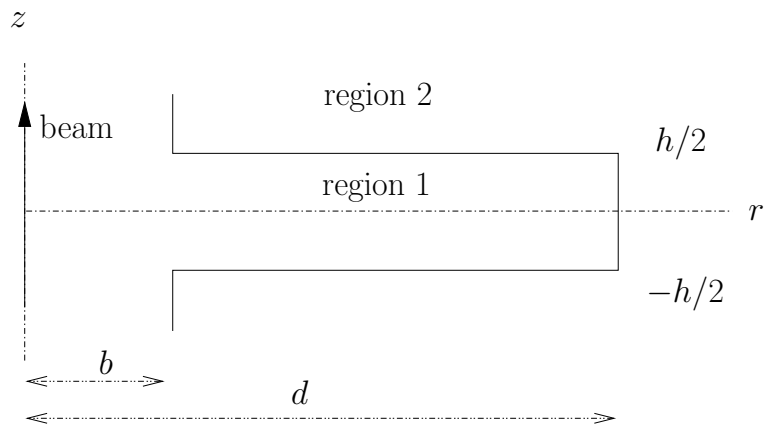

Figure 12: A pencil beam current flows in the z-direction along the axis of the annular magnet seeing one crack of the laminated surface at $r = b$ with adjacent laminations shorted at $r = d$. The θ-direction is out of the paper.

The beam flows along the axis of the annular magnet in the z-direction. The cylindrical symmetry of the problem results in azimuthal-angle-independent longitudinal electric field E_z and azimuthal magnetic field H_θ at the inner cylindrical surface of the laminated annular magnet, thus simplifying the derivation of the crack surface impedance per square. The crack is named region 1 while the adjacent laminations are named region 2. The derivation follows closely that for the parallel-face laminated surface, except that we are using the cylindrical coordinates. The equation satisfied by E_z is

$$\frac{1}{r}\frac{\partial}{\partial r}\left(r\frac{\partial E_z}{\partial r}\right) + q^2 E_z = 0 \ , \tag{3.35}$$

where $q^2 = k^2 + g^2$ with $k^2 = \omega^2\mu\epsilon$ and g defined by Eq. (3.3) as the decrement in the z-direction. The radial solution is Bessel functions of order zero with argument qr. We choose $H_0^{(2)}$ and $H_0^{(1)}$ to represent outgoing and incoming waves. Thus we can write the solution in

regions 1 and 2 as[‖]

$$\text{Region 1: } |z| < h/2 \quad \begin{cases} E_z = A\cosh(g_1 z)\left[H_0^{(2)}(qr) + \alpha H_0^{(1)}(qr)\right] , \\ E_r = -\dfrac{g_1 A}{q}\sinh(g_1 z)\left[H_1^{(2)}(qr) + \alpha H_1^{(1)}(qr)\right] , \\ H_\theta = \dfrac{j\omega\epsilon_1 A}{q}\cosh(g_1 z)\left[H_1^{(2)}(qr) + \alpha H_1^{(1)}(qr)\right] , \end{cases} \tag{3.36}$$

$$\text{Region 2: } |z| > h/2 \quad \begin{cases} E_z = B\, e^{-g_2|z|}\left[H_0^{(2)}(qr) + \alpha H_0^{(1)}(qr)\right] , \\ E_r = \dfrac{g_2 B}{q}\,\mathrm{sgn}(z)\, e^{-g_2|z|}\left[H_1^{(2)}(qr) + \alpha H_1^{(1)}(qr)\right] , \\ H_\theta = \dfrac{\sigma_{2c} B}{q}\, e^{-g_2|z|}\left[H_1^{(2)}(qr) + \alpha H_1^{(1)}(qr)\right] . \end{cases} \tag{3.37}$$

All comments for the field assignment for the parallel-face laminated surfaces apply here as well. Actually, all the parameters q, $k_{1,2}$, $g_{1,2}$, A, and B are exactly the same in the two situations. However, the parameter α, determined by $E_z = 0$ at $r = d$, is

$$\alpha = -\frac{H_0^{(2)}(qd)}{H_0^{(1)}(qd)} . \tag{3.38}$$

The crack surface impedance per square $\mathcal{R}_c$ becomes

$$\begin{aligned} \frac{\mathcal{R}_c}{Z_0} = -\frac{E_z(b)}{Z_0 H_\theta(b)} &= \frac{jqc}{\epsilon_{1r}\omega}\frac{H_0^{(2)}(qb)H_0^{(1)}(qd) - H_0^{(1)}(qb)H_0^{(2)}(qd)}{H_1^{(2)}(qb)H_0^{(1)}(qd) - H_1^{(1)}(qb)H_0^{(2)}(qd)} \\ &= \frac{jqc}{\epsilon_{1r}\omega}\frac{J_0(qb)N_0(qd) - N_0(qb)J_0(qd)}{J_1(qb)N_0(qd) - N_1(qb)J_0(qd)} , \end{aligned} \tag{3.39}$$

where $H_n^{(1),(2)} = J_n \pm jN_n$ has been used.

3.2.1 LOW-FREQUENCY BEHAVIOR

The only difference here from the parallel-face laminations is the factor containing Bessel functions. The small argument expansions of the Neumann functions are

$$N_0(x) \to \frac{2}{\pi}\ln\frac{x}{2} \quad \text{and} \quad N_1(x) \to -\frac{2}{\pi x} , \tag{3.40}$$

The numerator of the Bessel function part becomes $(2/\pi)\ln(d/b)$ while the denominator becomes $2/(\pi kb)$. Thus the crack impedance per square becomes

$$\frac{\mathcal{R}_c}{Z_0} \to (1+j)\frac{\omega\delta_{2c}b}{ch}\mu_{2r}\ln\frac{d}{b} . \tag{3.41}$$

[‖]With the time-varying convention $e^{j\omega}$, $H_m^{(2)}$ represents the outgoing wave and $H_m^{(1)}$ represents the incoming wave.

We get back the parallel-face result when the annular width of the lamination $(d-b)$ is much less than the inner radius b. Since $\ln(1+x) < x$, the crack surface impedance per square at low frequencies for an annular laminated magnet should be less than that for a parallel-face magnet. In most cases, however, $(d-b)/b > 1$. As an example, the Booster D-magnet has $x = (d-b)/b = 4.33$ ($b = 1.125''$, $d = 6''$), and $\ln(1+x)/x = 0.386$. In other words, if we approximate the Booster D-magnet as annular with radius b equal to the half-gap and d equal to the half-height, the crack surface impedance will be smaller than the parallel-face model by the factor 0.386 at low frequencies. This is verified in Fig. 11 where the real and imaginary parts of the crack impedance are plotted as dashed curves. Although we see in both cases the same $\omega^{1/2}$ behavior at low frequencies, the broad resonance peaks are much lower and occur at higher frequencies.

Using Eq. (3.41), the bend-around frequency can be estimated in exactly the same way as the parallel-face magnet. Instead of Eq. (3.28), we obtain

$$\left|(1+j)\frac{2\delta_{2c}\mu_{2r}}{\tau}\ln\frac{d}{b}\right| \sim 1 \ , \tag{3.42}$$

which reduces to Eq. (1.6). The Tevatron Lambertson magnet at location F0 can be approximated as annular in shape with $b = 1.25''$ and $d = 6''$. With the properties of the laminations listed in Table II, the bend-around frequency is estimated as ~ 250 MHz. The actual computation in Sec. 3 gives ~ 100 MHz.

3.2.2 HIGH-FREQUENCY BEHAVIOR

The large argument expansions of the Bessel functions are

$$H_0^{(1),(2)}(x) \to \sqrt{\frac{2}{\pi x}}e^{\pm j(x-\pi/4)} \quad \text{and} \quad H_1^{(1),(2)}(x) \to \sqrt{\frac{2}{\pi x}}e^{\pm j(x-3\pi/4)} \ . \tag{3.43}$$

Thus the crack impedance per square becomes

$$\frac{\mathcal{R}_c}{Z_0} = \frac{jkc}{\epsilon_{1r}\omega}\frac{e^{-jk(b-d)} - e^{jk(b-d)}}{e^{-j[k(b-d)-\pi/2]} - e^{j[k(b-d)-\pi/2]}} = \frac{jkc}{\epsilon_{1r}\omega}\tan k(d-b) \ . \tag{3.44}$$

which is exactly the general result for parallel-face laminated surfaces We therefore expect the crack surface impedances to differ somewhat at low frequencies but agree exactly at high frequencies. We see such similar high-frequency behavior in Fig. 11.

4 APPLICATIONS

4.1 FERMILAB BOOSTER

The Fermilab Booster consists of 48 F-magnets and 48 D-magnets. Each magnet has a length $\ell = 113.741''$. We approximate the magnets as parallel-face, having a vertical gap of $2b = 1.64''$ for the F's and $2b = 2.25''$ for the D's. Total height of each magnet is $2d = 12''$. The total longitudinal impedance seen by a centered beam is shown in the top plot of Fig. 13 in solid curves, where the contribution of all the 96 magnets are included. Besides the first broad resonance of $\sim$ 45 kΩ, the real part is roughly $\sim$ 25 kΩ rolling off slowly. At low frequencies, we see that its increase deviates from the square root of frequency. The imaginary part first starts off inductively because the image current goes around each lamination. However, it becomes capacitive above $\sim$ 50 MHz because the cracks behave as capacitance and displacement current just jumps across the cracks. We also approximate the magnets as annular rings with inner and outer radii $b = 1.125''$ and $d = 6''$. The results are shown in the same plot as dashed curves. They tend to be smaller in value than the parallel-faced approximation. For example, the first resonance peak is not so pronounced. This tendency is expected because the image current spreads out more uniformly in the annular-ring approximation.

The longitudinal impedance of the booster laminated magnets has been measured by Crisp and Fellenz [11] by stretching a wire through the magnet with the ends matched to 50 Ω via L-pads. The attenuation of transmission, S_{21}, was measured. The derivation of the longitudinal impedance depends on the model used. A transmission-line model gives $\mathcal{R}e\, Z_0^{\|}$ reaching an asymptotic value of $\sim$ 37 kΩ, whereas we obtain 18 to 20 kΩ in the computed results of Fig. 13. The rise at low frequencies is similar, with the exception that the measurement does not show the broad peak near 50 MHz; it only shows a smaller peak around 200 MHz. The measured $\mathcal{I}m\, Z_0^{\|}$ appears to be always inductive, without a transition into capacitive as demonstrated by the field-theoretical computation. In any case, we are still glad to see the extent of agreement between theory and measurement, because we need to understand that there are discrepancies in the both methods. The annular-ring approximation of the laminations is far from reality. Even the parallel-face approximation is arguable because the Booster magnets are gradient magnets. On the other hand, the wire in the experimental measurement disturbs the electromagnetic fields in the system. [12] For example, the longitudinal electric field in the monopole mode is a constant A inside the

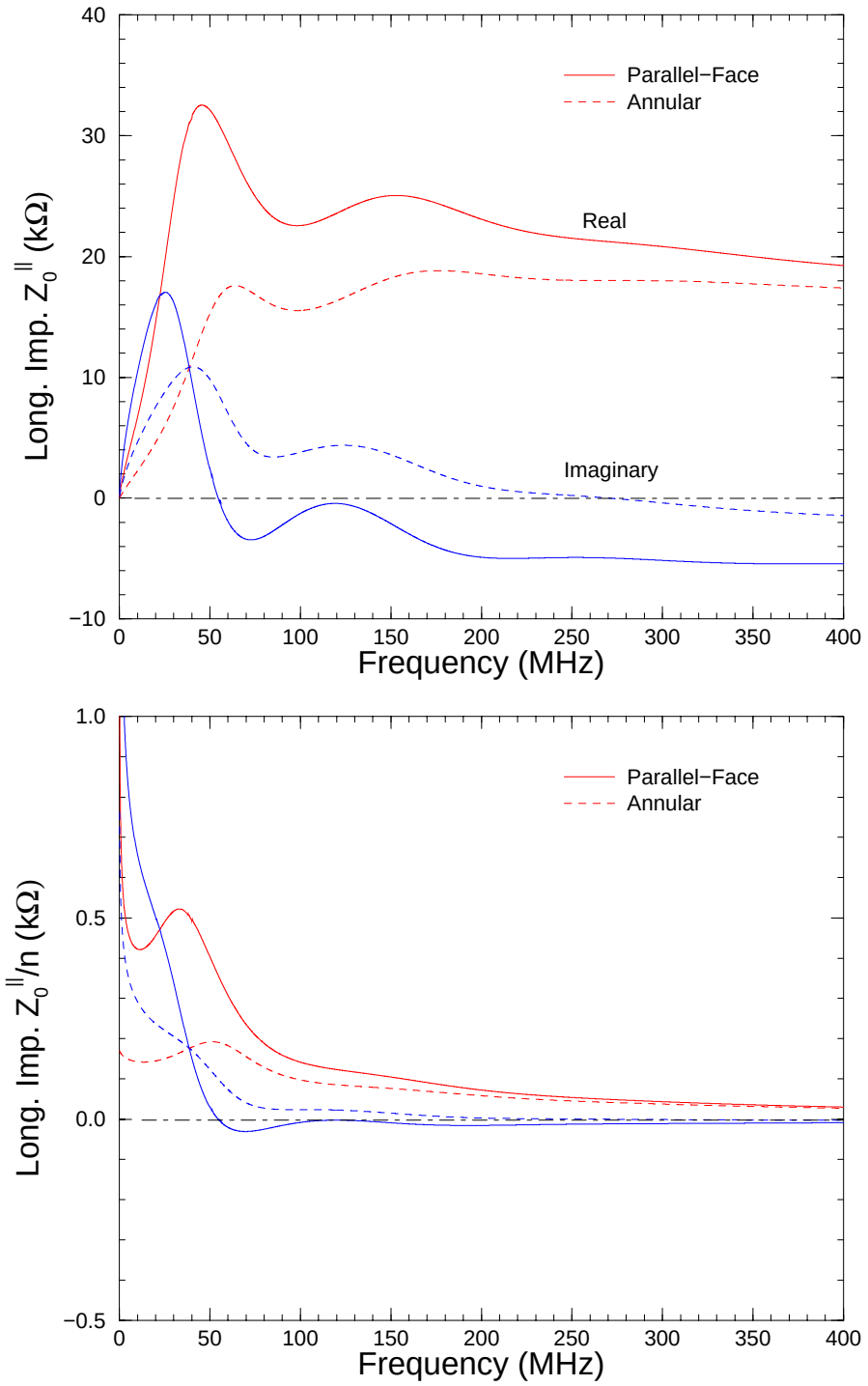

Figure 13: Top: Longitudinal monopole impedance $Z_0^{\parallel}$ of the 96 laminated magnets of the Fermilab Booster experienced by a centered beam. Bottom: The corresponding $Z_0^{\parallel}/n$.

annular-ring system. With a wire of radius r_0, the longitudinal electric field is modified to

$$\tilde{E}_z(r) = A\left[1 - \frac{\ln(r/b)}{\ln(r_0/b)}\right] \qquad r_0 < r < b \ , \tag{4.1}$$

where b is the inner radius of the annular ring. For the higher-order azimuthal modes, the r^m behavior of the longitudinal electric field is modified to

$$\tilde{E}_z(r) = A\left[r^m - \frac{r_0^{2m}}{r^m}\right] \qquad r_0 < r < b \ , \tag{4.2}$$

Thus the wire seems to perturb the wake-field pattern profoundly. In conclusion, we are content in getting the theory and measurement to agree.

4.1.1 Microwave Instability

The revolution frequency of the Fermilab Booster at the injection kinetic energy of 400 MeV is 450.8 kHz and increases to 628.7 KHz at the extraction kinetic energy of 8 GeV. In the lower plot of Fig. 13, we show $Z_0^{\parallel}/n$ of the 96 laminated Booster magnets at the booster extraction energy. Here we see the $\omega^{-1/2}$ behaviors of the impedances at low frequencies. The first broad resonance of the real part in the top plot translates into $\mathcal{R}e\, Z_0^{\parallel}/n \sim 0.55$ kΩ around 40 kHz, but it rolls off to less than $\sim 140\ \Omega$ above 100 MHz. Let us estimate the single-bunch microwave stability of the Booster with a bi-parabolic distribution. The bunch area is around $A = 0.1$ eV-s. If $\widehat{\Delta E}$ is the half energy spread, the half time spread is $\hat{\tau} = A/(\pi\widehat{\Delta E})$ and the peak current is

$$I_{\rm pk} = \frac{3eN_b}{4\hat{\tau}} \ , \tag{4.3}$$

with N_b representing the number of protons in the bunch. The maximum allowable impedance for stability is given by the Keil-Schnell criterion [10]

$$\left|\frac{Z_0^{\parallel}}{n}\right| \lesssim \frac{|\eta|E}{eI_{\rm pk}\beta^2}\left(\frac{\Delta E}{E}\right)^2_{\rm FWHM} = \frac{8|\eta|(A/e)\widehat{\Delta E}}{3\pi e N_b \beta E} \ . \tag{4.4}$$

In above, we have used the fact the $(\Delta E)_{\rm FWHM} = \sqrt{2}\widehat{\Delta E}$ for the bi-parabolic distribution. The transition gamma for the Booster is $\gamma_t = 5.446$. We try to evaluate this limit at extraction when the total particle energy is $E = 8.938$ GeV at the bunch intensity of $N_b = 6 \times 10^{10}$. With a half energy spread of $\widehat{\Delta E} = 8$ MeV, the half bunch length is $\hat{\tau} = 3.98$ ns and the peak current is $I_{\rm pk} = 1.81$ A. The slip factor is $\eta = 0.0227$. This gives the stability threshold budget of $|Z_0^{\parallel}/n| = 181\ \Omega$. In order to drive microwave instability, the perturbing

ripples must have wavelengths much shorter than the total length of the bunch $2\hat{\tau} \sim 8$ ns, or the perturbing frequencies $f \gg 1/(2\hat{\tau}) = 125$ MHz. We see in the figure that $\mathcal{R}e\, Z_0^{\parallel}/n < 120\ \Omega$ and $\left|\mathcal{I}m\, Z_0^{\parallel}/n\right| < 5\ \Omega$ in this frequency range, indicating that the Booster single bunch should be stable. At the injection kinetic energy of 400 MeV, the slip factor is $\eta = -0.4578$. At the same bunch area and half energy spread, the stability threshold increases to $|Z_0^{\parallel}/n| = 47500\ \Omega$. Actually, the bunch length is much longer at injection. However, the stability near transition is still questionable because the slip factor will be very much smaller.

4.1.2 Transverse Coupled-Bunch Instabilities

The vertical dipole impedance of the booster laminated magnets is shown in Fig. 14. We see that, as expected, the imaginary part approaches the bypass inductive reactance

$$Z_1^V \to \frac{\pi Z_0}{16}\left(\frac{L_F}{b_F^2} + \frac{L_D}{b_D^2}\right) = 36.2\ \mathrm{M\Omega/m} \tag{4.5}$$

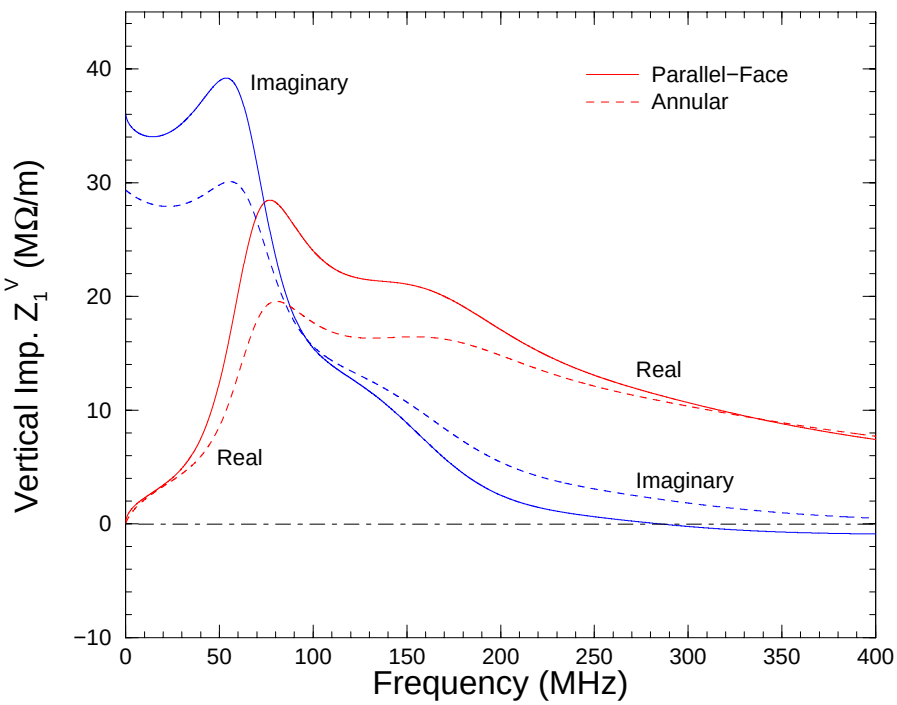

Figure 14: Real and imaginary parts of the vertical dipole impedance Z_1^V of the booster laminated magnets are shown as solid curves in the parallel-plate approximation with plate. Also plotted in dashes are the real and imaginary parts of the transverse dipole impedance $Z_1^{\perp}$ in the annular ring approximation. The radii have been taken as half the plate-separation.

at low frequencies independent of the properties of the laminations, where $2b_{F,D}$ and $L_{F,D}$ represent the pole-face gap and total length of 48 F or D magnets. The real part rolls off to zero at zero frequencies. Unlike the situation of a smooth beam-pipe wall, the bend-around occurs at the much higher frequency around 80 MHz. This reflects the fact that the surface impedance per square is very much larger than that for a smooth beam-pipe wall. This agrees approximately with the prediction of Eq. (1.6). The bend-around of $\mathcal{R}e\, Z_1^V$ leads to a very different contribution to the transverse coupled-bunch instabilities. If it were not for this bend-around, $\mathcal{R}e\, Z_1^V$ would reach, according to the $\omega^{-1/2}$ behavior, 4056 MΩ/m at the most dangerous betatron line at the $n \approx -1/2$ harmonic or $f = -313.9$ kHz, where we have chosen the vertical betatron tune to be $\nu_\beta \approx 6.5$. At an intensity of $N_b = 6 \times 10^{10}$ per bunch and $M = 84$ bunches, the growth rate given by

$$\frac{1}{\tau} = \frac{eMI_b c}{4\pi\nu_\beta E}\, \mathcal{R}e\, Z_1^V F' \ , \tag{4.6}$$

where the form factor is $F' = 0.811$ for Sacherer's sinusoidal distribution, would lead to a growth rate of $\tau^{-1} = 7.42 \times 10^5$ s^{-1} or a growth time of 1.36 μs or 0.846 revolution turns (about 6.7 times faster at injection). Now $\mathcal{R}e\, Z_1^V$ is bounded by its peak of 28.5 MΩ/m at 77 MHz. When this value is substituted into Eq. (4.6) instead, the growth rate drops to $\tau^{-1} = 5400$ s^{-1} or a growth time of 0.19 ms or 120 revolution turns. The actual growth rates will be much less than this because unlike the narrow peak-like contribution of the $\omega^{-1/2}$ contribution near zero frequency, this peak of $\mathcal{R}e\, Z_1^V$ is very broad so that the damping contribution at positive frequency will nearly cancel the growing contribution at negative frequency. In short, $\mathcal{R}e\, Z_1^V$ of a laminated magnet will not contribute to transverse coupled-bunch instabilities because of the high bend-around frequency of $\mathcal{R}e\, Z_1^V$. In this sense, transverse coupled-bunch growths will become less in unshielded laminated magnets than if the laminated surface is shielded by a smooth metallic beam pipe. The main reason is that the image current flows through the bypass inductance at low frequencies rather than around each lamination.

However transverse coupled-bunch instabilities have been reported in the Fermilab booster although they have never been a serious problem. This is because the laminated magnets cover only about 60% of the ring. In between the magnets there are beam pipes. The booster is 24-fold symmetric. In each period, the beam pipe in the 6-m long straight section between the D-magnets is of diameter 2.25″, the beam pipe in the 1.2-m short straight section between the F-magnets is of diameter 4.25″, and the two 0.5-m straights joining a D-magnet to a F-magnet is of radius 2.25″. Assuming these beam pipes are made of stainless

steel with conductivity $\sigma_c = 0.5 \times 10^7\ (\Omega\mathrm{m})^{-1}$, they contribute to the longitudinal impedance

$$Z_0^{\parallel} = (1+j)0.609\sqrt{n}\ \Omega\ , \tag{4.7}$$

according to Eq. (2.48) and vertical transverse impedance

$$Z_1^V = (1+j)\frac{0.122}{\sqrt{n}}\ \mathrm{M}\Omega/\mathrm{m}\ , \tag{4.8}$$

according to Eq. (2.58). Since $Z_0^{\parallel}/n$ rolls off with frequency, the longitudinal impedance of the beam pipe will not lead to any beam instability. The transverse impedance, however, will contribute to transverse coupled-bunch instabilities. According to Eq. (4.6), the worst vertical instability at the present vertical betatron tune 6.8 will have a growth rate of 221 s^{-1} (growth time 4.53 ms) at the injection kinetic energy of 400 MeV. The growth rate decreases in the ramp and becomes 39.1 s^{-1} (growth time 25.6 ms) when reaching the extraction kinetic energy of 8 GeV. The growth time of the worst mode during the ramp is shown in Fig. 15. The integrated total growth during the ramp is 3.25, or a total growth in amplitude $e^{3.25} = 25.8$. Because of the short ramp period, the growth is not too large. Landau

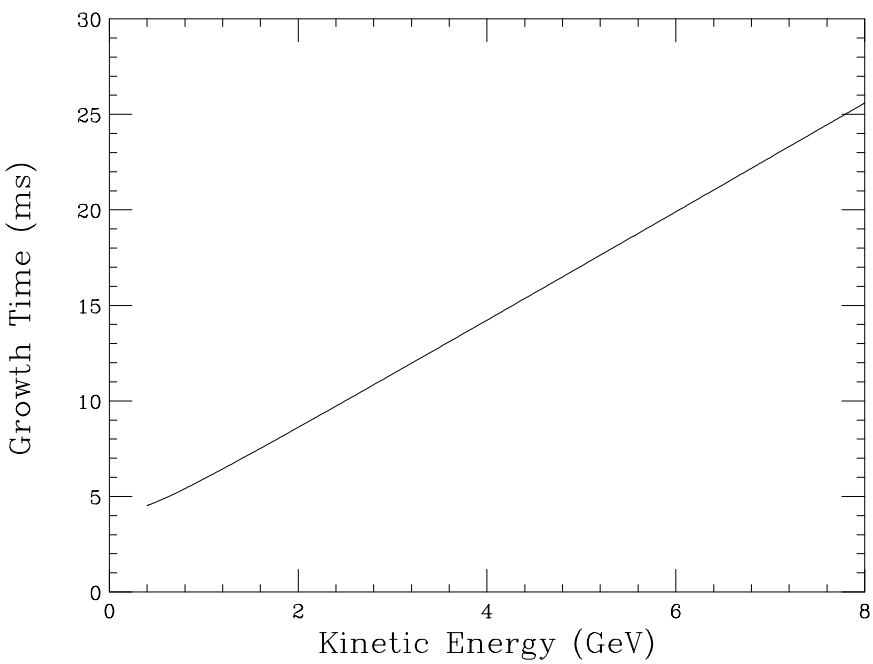

Figure 15: Growth time of the worst vertical coupled-bunch instability of the Booster driven by the resistive-wall impedence of the beam pipe is shown increasing nearly linearly with the kinetic energy of the beam. The vertical betatron tune is assumed to be 6.8.

damping of the instability is possible by the introduction of a betatron angular frequency spread using octupoles or sextupoles, with the spread larger than the growth rate. Damping by chromaticity is not efficient, because of the large slip factor at injection when the growth rate is fastest. Another way to reduce the growth is to change the vertical betatron tune to one with a smaller residual tune. For example, with the vertical tune of 6.4, the growth rate at any moment will be reduced by $\sqrt{0.6/0.2} = 1.73$ times.

4.1.3 Transverse Head-Tail Instabilities

Although laminated magnets will not drive transverse coupled-bunch instabilities, the large broad real part of the transverse impedance can drive transverse head-tail instabilities. This will be a single-bunch effect and the mth head-tail mode corresponds to transverse oscillation of the bunch with $|m|$ nodes along its longitudinal length, not including the ends.[†] Without any damping mechanism included, the growth rate of mode m is

$$\begin{aligned}\frac{1}{\tau_m} &= -\frac{1}{1+m}\frac{ecI_b}{4\pi E\omega_0\nu_\beta}\int_{-\infty}^{\infty} d\omega\ \mathcal{R}e\, Z_1^{\perp}(\omega)h_m(\omega-\omega_\xi) \\ &= -\frac{1}{1+m}\frac{ecI_b}{4\pi E\omega_0\nu_\beta}\int_{0}^{\infty} d\omega\ \mathcal{R}e\, Z_1^{\perp}(\omega)\big[h_m(\omega-\omega_\xi)-h_m(\omega+\omega_\xi)\big]\ ,\end{aligned} \tag{4.9}$$

where $h_m(\omega)$ is the power spectrum of the bunch normalized according to

$$\frac{\tau_L}{2\pi}\int_{-\infty}^{\infty} d\omega\, h_m(\omega) = 1\ . \tag{4.10}$$

The chromatic shift in angular betatron frequency ω_ξ is defined as

$$\omega_\xi = \frac{\xi\omega_0}{\eta}\ , \tag{4.11}$$

with ξ being the chromaticity. It is so defined that $\omega_\xi\tau_L$ amounts to the betatron phase difference in betatron oscillation between the head and tail of the bunch. It is clear that there will not be any excitation when the chromaticity is equal to zero. The growth rate will be proportional to chromaticity when chromaticity is small. Mode $m = 0$ is called the rigid dipole mode where the whole bunch is oscillating transversely as a whole. Modes $m = \pm 1$ are called the π-modes or dipole modes, where the head and tail are 180° out of betatron phase.

[†]Here we use m to classify the head-tail modes. However, this is different from the m used earlier, which denotes the azimuthal configuration of the cylindrical beam pipe.

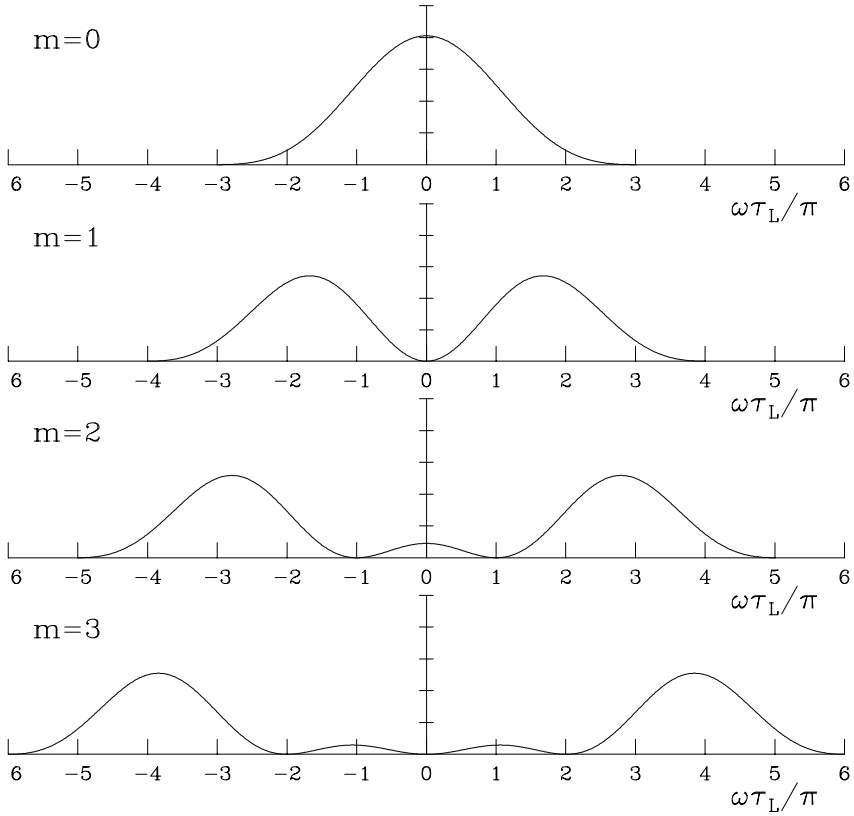

Figure 16: Power spectra $h_m(\omega)$ for modes $m = 0$ to 3 at zero chromaticity. The power spectra of modes $m = -1$, -2, and -3 are exactly the same as those of $m = 1$, 2, and 3.

For an illustration, let us use Sacherer's sinusoidal modes with eigen-longitudinal linear density

$$\rho_m(\tau) \propto \begin{cases} \cos \dfrac{(|m|+1)\pi\tau}{\tau_L} & m = 0, \ \pm 2, \ \cdots , \\ \sin \dfrac{(|m|+1)\pi\tau}{\tau_L} & m = \pm 1, \ \pm 3, \ \cdots , \end{cases} \tag{4.12}$$

The power spectrum turns out to be

$$h_m(\omega) = \frac{4(|m|+1)^2}{\pi^2} \frac{1 + (-1)^m \cos \pi y}{[y^2 - (|m|+1)^2]^2} , \tag{4.13}$$

with $y = \omega\tau_L/\pi$, and the 4 lower modes are shown in Fig. 16 at zero chromaticity. In the presence of a positive/negative chromaticity, the power spectrum just shifts to higher/lower frequencies when the slip factor $\eta > 0$. Notice that modes m and $-m$ are positive and negative sidebands of a betatron line. Although their power spectra appear exactly the

same, both of them must be considered because they do not have symmetry property with respect to zero frequency.

Let us use the transverse impedance of the Booster laminated magnets in the annular model computed in Fig. 14. At the extraction kinetic energy of 8 GeV, the full bunch length is roughly $\tau_L = 7.96$ ns. The growth rates for the bunch intensity of $N_b = 6 \times 10^{10}$ are computed as functions of chromaticity for modes $m = 0, \ \pm 1, \ \pm 2$, and ± 3, and the results are shown in the top plot of Fig. 17. In order to have the maximum growth rate for mode $m = 0$, we need to shift the center of the $m = 0$ power distribution in Fig. 16 to ~ -150 MHz, where the center of the the broad peak of $\mathcal{R}e\, Z_1^{\perp}$ resides (Fig. 14). This requires a chromaticity of $\xi \sim -5.5$ with $\eta = 0.0227$, and is exactly what we see in Fig. 17. Notice that, unlike the head-tail instabilities driven by the $\omega^{-1/2}$ transverse resistive-wall impedance near zero frequencies, where we have either mode $m = 0$ very unstable and the modes $m = \pm 1$ very stable or vice versa depending on the sign of the chromaticity, here the $\mathcal{R}e\, Z_1^{\perp}$ that drives the head-tail oscillations is at a much higher frequency. As a result, we can have both the $m = 0$ and $m = \pm 1$ stable or unstable. The maximum growth rate for this rigid dipole mode is $1/\tau_0 = 7.55 \times 10^3$ s^{-1} or minimum growth time 0.132 ms. To avoid the instabilities of this mode and also modes $m = \pm 1$, the chromaticity is set to positive above transition. Now the higher modes $m = \pm 2, \ \pm 3, \ \cdots$ become unstable. The maximum growth rates without damping are, respectively, 0.346×10^3 s^{-1} (or growth time 2.89 ms) for $m = \pm 2$ and 0.162×10^3 s^{-1} (or growth time 6.17 ms) for $m = \pm 3$. The stabilities of these modes can be understood as follows. Consider modes $m = \pm 2$ and place the power spectra of Fig. 16 on top of the real part of the transverse impedance in Fig. 14. At full bunch length $\tau_L = 7.96$ ns, we find the positive- and negative-frequency power spectra just lie *outside* the broad resonance of $\mathcal{R}e\, Z_1^V$ centered around 150 MHz. We now increase the chromaticity from zero to positive. The power spectra move to the right with the negative-frequency power spectrum moving into the resonance at negative frequency and the positive-frequency power spectrum moving out of the resonance at positive frequency, resulting in more contribution from $\mathcal{R}e\, Z_1^V$ at negative frequency. This mode is therefore unstable. The positive- and negative-frequency power spectra of modes $m = \pm 3$ are further apart than modes $m = \pm 2$. To have these modes unstable, larger shift of the power spectra to the right or higher chromaticity is required. On the other hand, when the power spectra of modes $m = \pm 1$ are overlayed onto $\mathcal{R}e\, Z_1^V$, the positive- and negative-power spectra lie *inside* the broad resonances of $\mathcal{R}e\, Z_1^V$ at positive and negative frequencies. An increase of chromaticity to positive will move the negative-frequency power spectrum more out of

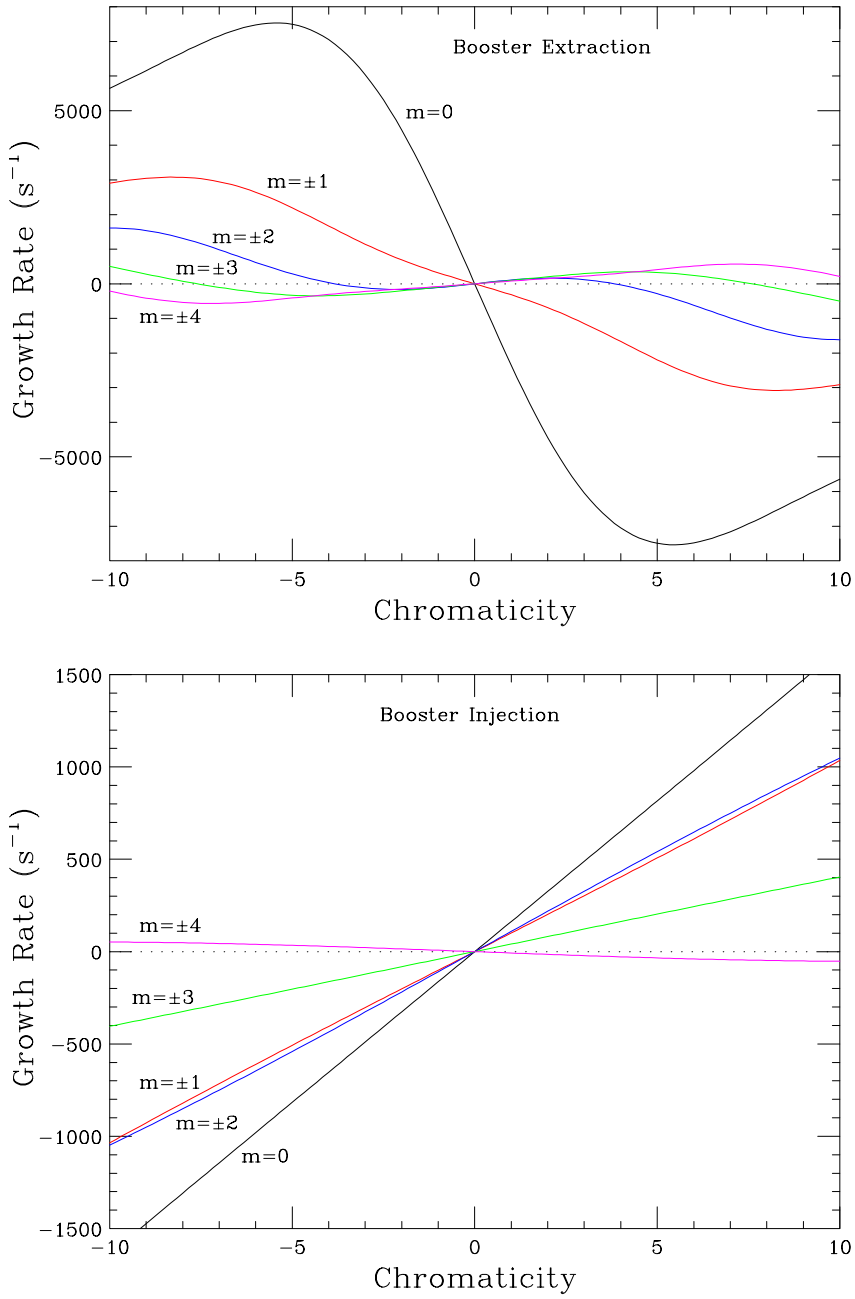

Figure 17: Top: Vertical head-tail growth rates are shown for the lower head-tail azimuthal modes $m = 0,\ \pm 1,\ \pm 2,\ ,\pm 3$ of the Fermilab Booster bunches at the extraction kinetic energy of 8 GeV as functions of chromaticity ξ, with full bunch length $\tau_L = 7.96$ ns. The driving force comes from the laminated magnets in the annular-ring approximation. $m = 0$ is the rigid dipole mode and $m = \pm 1$ is the π mode. Bottom: The same are shown at the injection kinetic energy of 400 MeV. The full bunch length is assumed to be $\tau_L = 25.4$ ns.

the broad resonance of $\mathcal{R}e\, Z_1^Y$ at negative frequency and move the positive-frequency power spectrum into the broad resonance at positive frequency, resulting in more contribution from the positive-frequency broad resonance, making these modes stable.

So far we have assumed that the azimuthal head-tail modes are valid eigenmodes describing the various ways the bunch is oscillating. These modes are separated by the synchrotron frequency at zero beam intensity. The driving force which is proportional to the beam intensity, however, leads to a coherent frequency shift for each mode. If the shifts are large enough, two modes will merge into a new mode that is stable and another that is unstable. This is called the transverse mode-coupling instability. When this happens, we can no longer employ azimuthal mode number to identify the modes.

In exactly the same way that the growth rates are derived in Eq. (4.9), the frequency shift of the azimuthal head-tail mode m is

$$\Delta\omega_m = -\frac{1}{1+|m|}\frac{ecI_b}{4\pi E\omega_0\nu_\beta}\int_0^\infty d\omega\; \mathcal{I}m\, Z_1^\perp(\omega)\big[h_m(\omega-\omega_\xi)+h_m(\omega+\omega_\xi)\big]\ . \tag{4.14}$$

The results are shown as tune shifts in Fig. 18. The synchrotron tune near extraction is 0.005 when the rf voltage is 500 kV and will be smaller at lower rf voltage. We see that the head-tail mode $m = 0$ is shifted by very much, although the higher modes are not much

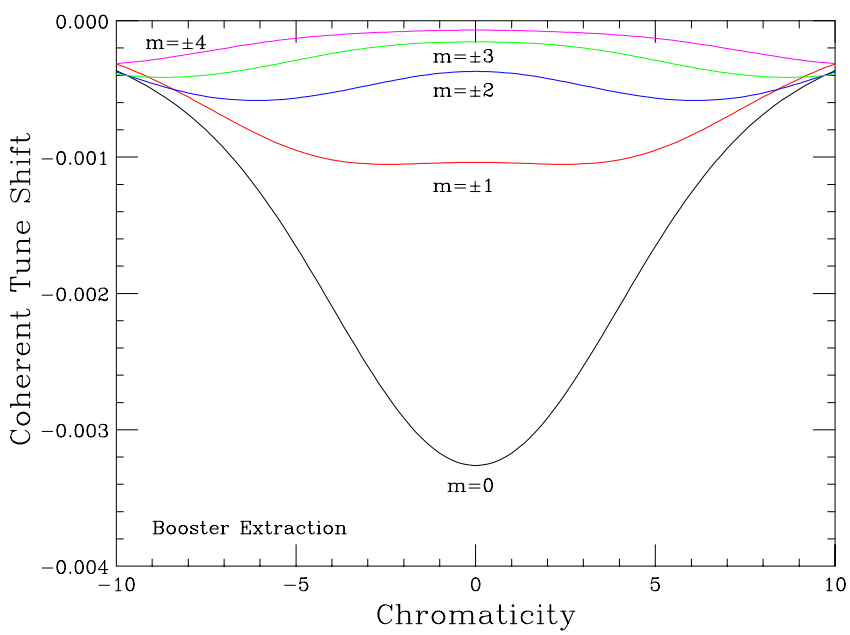

Figure 18: Coherent tune shifts of the vertical head-tail azimuthal modes $m = 0,\ \pm 1,\ \pm 2,\ \pm 3$ as functions of chromaticity of the Fermilab Booster at the extraction kinetic energy of 8 GeV.

shifted. One may wonder whether the $m = 0$ mode will be shifted downward by so much that it may collide with mode $m = -1$ starting an instability. However, we must also notice that the incoherent space-charge tune shift is large, according to the formula for a bi-Gaussian transverse distribution,

$$\Delta\nu_{\rm spch}^{\rm max} = \frac{3N_t r_p}{2\gamma^2\beta\epsilon_{_N} B} \tag{4.15}$$

can be large also, where $\epsilon_{_N} = 2.7 \times 10^{-12} N_t$ πmm-mr is the 95% normalized emittance of the Booster as measured by Ankenbrandt and Holmes, [14] N_t is the total number of protons in the Booster, and B is the single-bunch bunching factor. Assuming a Gaussian longitudinal profile at extraction, the Booster bunch that we considered above has a rms length $\sigma_\tau = \tau_{_L}/(2\sqrt{6}) = 1.62$ ns, and the bunching factor is $B = \sqrt{2\pi}\sigma_\tau h f_0 = 0.215$, where $h = 84$ is the rf harmonic. The maximum tune shift is $\Delta\nu_{\rm spch}^{\rm max} = -0.0140$ near extraction. While the transverse space-charge force shifts every mode downward coherently, it will not shift mode $m = 0$ at all, because this mode is rigid and the wake-field pattern of the space-charge force moves with the bunch. The coherent space-charge tune shifts of the other modes are roughly of the same order of the incoherent space-charge tune shift. Thus both modes $m = 0$ and -1 are shifted downward but by different forces, the former by the impedance of the vacuum chamber while the latter by the space-charge force. For this reason, these two modes will not collide with each other so easily. [13] This justifies why the azimuthal head-tail modes are good eigenmodes in this study.[‡]

The incoherent space-charge tune shift is important also when Landau damping is addressed. The distribution density of incoherent space-charge tune shift is depicted in Fig. 19. It shows that [15, 17] the average shift is $\langle\Delta\nu_{\rm spch}\rangle = 0.633\Delta\nu_{\rm spch}^{\rm max} = -0.0089$ and the rms shift is $\Delta\nu_{\rm spch}^{\rm rms} = 0.168\Delta\nu_{\rm spch}^{\rm max} = 0.0019$. Thus the tune spread due to space-charge will not cover the coherent lines of the unstable azimuthal modes and, as a result, will not provide any Landau damping. The instabilities of these modes can be damped, however, by a tune spread driven by either sextupoles or octupole. The required spread for damping should be at least $|\langle\Delta\nu_{\rm spch}\rangle| - \Delta\nu_{\rm spch}^{\rm rms} = 0.0065$.

We see in Eq. (4.12) that the head-tail growth rates are inversely proportional to the beam energy. One may expect the head-tail growths would be very much larger at the Booster injection energy of 400 MeV. However, the revolution frequency is $f_0 = 392$ kHz

[‡]This conclusion holds for the Booster also at the injection energy of 400 MeV. The coherent tune shifts are -0.0454, -0.00773, -0.00199, and -0.00056 for the azimuthal head-tail modes $m = 0$, ± 1, ± 2, and ± 3, and are almost constant in the chromaticity between -10 and 10. On the other hand, the maximum incoherent space-charge tune shift is $\Delta\nu_{\rm spch}^{\rm max} = -0.068$.

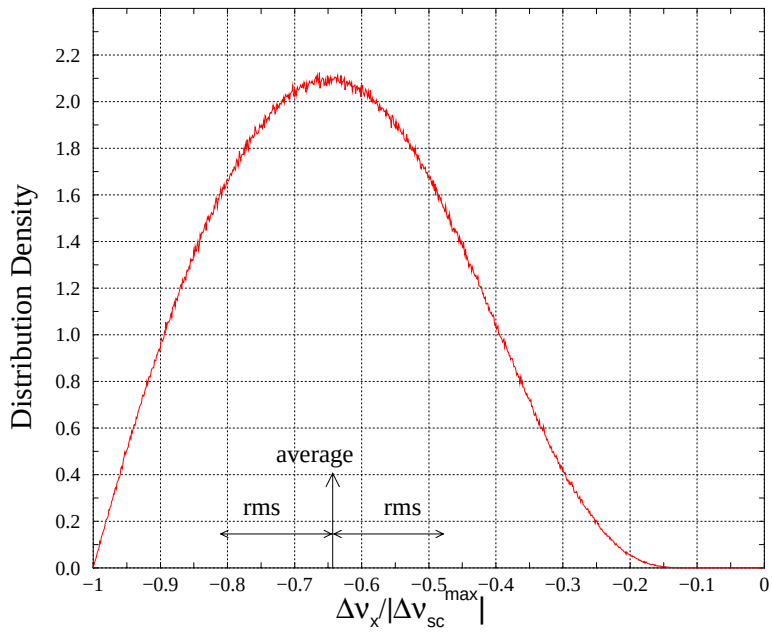

Figure 19: Distribution density of particles in a coasting beam with bi-Gaussian transverse distribution with incoherent space-charge tune shift $\Delta\nu_{\rm spch}$, in units of the maximum $|\Delta\nu_{\rm spch}^{\rm max}|$, where $\Delta\nu_{\rm spch}^{\rm max}$ is the maximum space-charge tune shift or that of a particle at the center of the beam center with infinitesimal betatron oscillation amplitude. The average space-charge tune shift is $\langle\Delta\nu_{\rm spch}\rangle = 0.633\Delta\nu_{\rm spch}^{\rm max}$, and the rms space-charge tune spread is $\Delta\nu_{\rm spch}^{\rm rms} = 0.168\Delta\nu_{\rm spch}^{\rm max}$.

and the slip factor is $\eta = -0.3919$ at injection (versus $f_0 = 629$ kHz and $\eta = 0.0227$ at extraction). To shift the center of the power spectrum to the broad peak of $\mathcal{R}e\, Z_1^{\perp}$ near -150 MHz will require a chromaticity of $\xi = 132$. As a result, the growth rates at injection in Fig. 17 only show the parts linear in chromaticity and do not become very high at reasonable chromaticities of $|\xi| < 10$.

At injection, the bunching factor is $B \approx 0.49$ corresponding to a full bunch length of $\tau_L \approx 25.4$ ns. The maximum space-charge tune shift is, according to Eq. (4.15), $\Delta\nu_{\rm spch}^{\rm max} = 0.38$. On the other hand, the coherent tune shift for the head-tail modes are roughly -0.052, -0.034, -0.021, and -0.013, respectively, for modes $m = 0,\ \pm 1,\ \pm 2,\ \pm 3$, and are nearly independent of chromaticity. Since the incoherent tune shift is so far away from the coherent tune shifts, it is nearly impossible to rely on sextupole or octupole tune spread to damp the head-tail instabilities. Luckily, because of the long bunch length, the power spectra for modes $|m| \leq 3$ are of lower frequency than the broadband resonance of the impedance of the lamination magnets. Thus, with a negative chromaticity, the only unstable head-tail modes

are $|m| \geq 4$. If the chromaticity is small enough negatively, the growth rates of these modes will be small also. For example, with $\xi = -2$, the growth rate of modes $m = \pm 4$ are only ~ 15 s^{-1} (or growth time 67 ms), which is quite tolerable.

The energy region where head-tail instabilities might become more severe is near transition crossing, when the slip factor is small. To circumvent this, the chromaticity must be kept negative below transition and controlled to be less and less negative as transition crossing is approached. Right at transition, the chromaticity is made positive but small and can be increased gradually afterwards. Small chromaticity near transition will lead to smaller instability growth rates. Theoretically, all head-tail modes are stable at zero chromaticity.

4.2 FERMILAB TEVATRON

4.2.1 Lambertson Magnets

Lambertson magnets are employed for injection into and extraction out of an accelerator ring. There are three Lambertson magnets at location F0 of the Tevatron, and the cross-section of one is shown in Fig. 20. During injection, the beam is at first in the rectangular region, where it moves vertically in the presence of the horizontal magnetic field. The beam later enters into and circulates inside the $2.5''$ high by $4''$ wide field-free region. Each of these F0 Lambertson magnets is of length $L = 126''$. Lambertson magnets do not have conventional vacuum pipes. They are constructed of laminations, which are electrically connected at their outer edge, by welding them to index bars or rods. Since the particle beam is in the field-free region, during ramping and storage, we simulate the laminations as annular rings having inner radius $b = 1.25''$ and outer radius $d = 6''$. The thickness of each lamination is $0.0375''$. For all other properties, such as crack width, electric permittivity, conductivity, and magnetic permeability, those tabulated in Table II will be used. The transverse dipole impedance for one such F0 Lambertson magnet is computed and the result is shown in Fig. 21. The vertical dipole impedance of the F0 Lambertson magnet has been measured by Crisp and Fellenz [16]. The impedance was determined directly from the attenuation measured along two parallel wires driven differentially. The wires, separated by $\Delta = 1.0$ cm, form a TEM balanced transmission line. Each end was matched to 100 Ω with resistive L-pads and driven with a 100 Ω broadband 180° hybrid splitter. A network analyzer was used to measure the transmission coefficient S_{21} through the device. The transverse impedance is determined

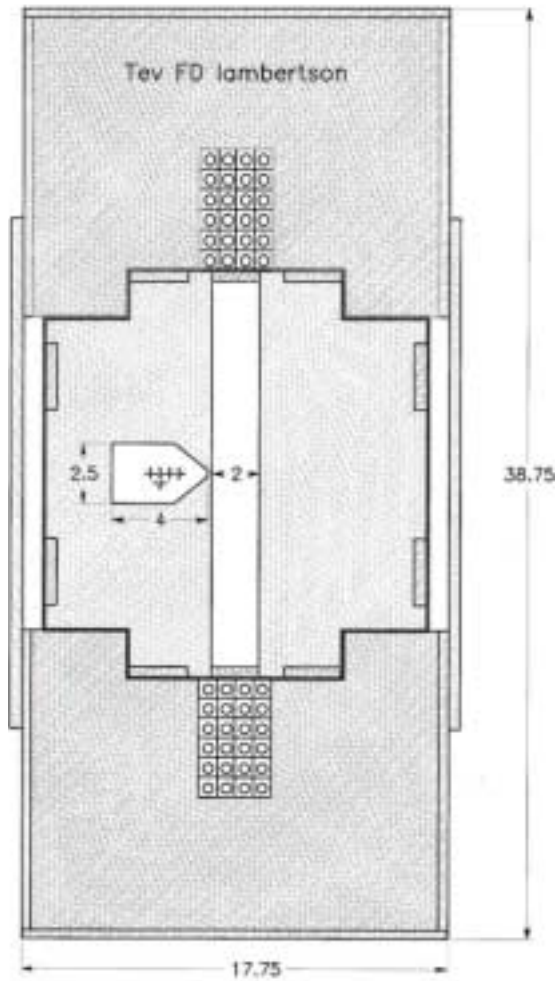

Figure 20: A cross-sectional drawing of the Lambertson magnet at Tevatron F0. The measurements are in inches.

from

$$Z_1^V = -\frac{c}{\omega\Delta^2} 2 Z_c \ln S_{21} \ , \tag{4.16}$$

where the characteristic impedance was $Z_c = 518\,\Omega$. There are agreements and disagreements between the theory-computed and the measured results. The imaginary part of S_{21} is roughly $\pi\omega/(8\omega_c)$ with $\omega_c/(2\pi) = 1$ GHz. This gives $\mathcal{I}m\, Z_1^V \approx 0.19$ MΩ/m at zero frequency, agreeing very well with the theoretical $\pi Z_0 L/(16b^2)$ in Eq. (2.56). The computed value of $\mathcal{R}e\, Z_1^V \approx 0.01$ MΩ/m at 1 GHz also agrees with measurement. In fact, these two values depend critically on the inner radius of the field-free region. The agreement between theory and measurement just indicates that $b = \frac{1}{2}''$ is the correct choice of the inner radius in the annular-ring model. The broadband region of $\mathcal{R}e\, Z_1^V$ does not agree so well. Figure 21 shows $\mathcal{R}e\, Z_1^V$ close to 0.1 MΩ/m at 50 to 150 MHz. However, the measurement shows only about

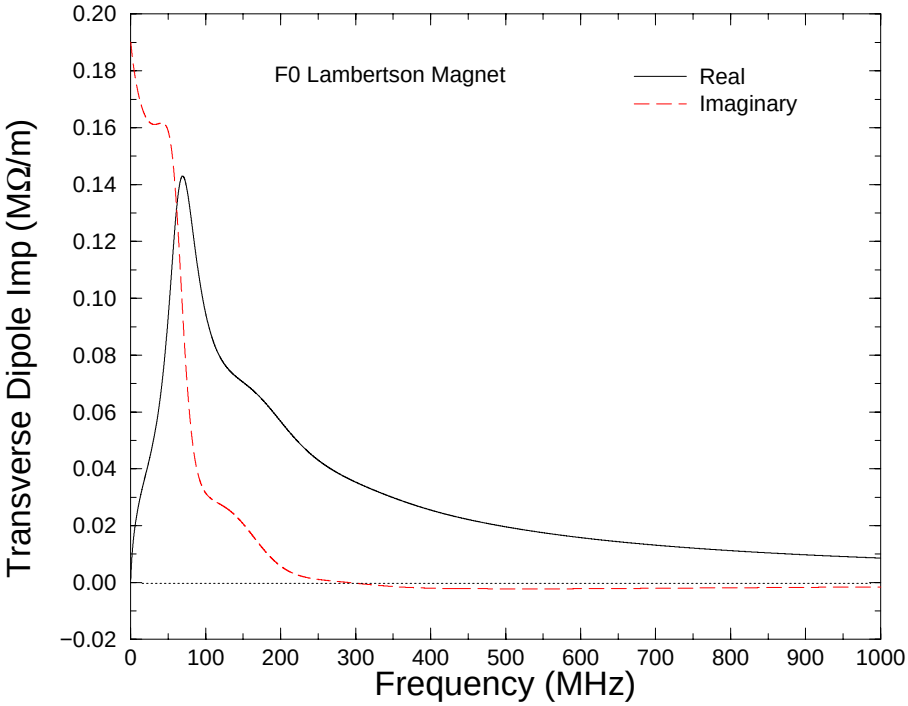

Figure 21: Vertical dipole impedance of a Tevatron F0 Lambertson magnet with the particle beam centered inside the field-free region.

0.02 MΩ/m, and we do not understand the discrepancy.

There had been also an older type of Lambertson magnets at the Tevatron location C0, for extracting the beam for fixed-target experiment. Since the fixed-target operation has been terminated, three such magnets at C0 had been removed. The cross-section of one such magnet is shown in Fig. 22. When these Lambertson magnets were first installed, some Tevatron bending dipoles had been removed because of space limitation. To compensate the loss of bending, the Lambertson magnets had been operating in the reverse order. In normal beam circulation, the Tevatron beam must pass through the $1''$ high rectangular field region. The beam is kicked into the $2''$ by $3.5''$ free-free region during an extraction. We model this magnet as parallel-face with a vertical gap of $2b = 1''$ and assume that the laminations are shorted at a distance of $d = 6''$ above and below the center line of the $1''$ rectangular field region. The length of this C0 magnet is $L = 218''$ consisting of 5812 laminations each of thickness $0.0375''$. Other properties are taken from Table II. The computed vertical impedance is shown in Fig. 23. Comparing with Fig. 21 for the F0 Lambertson magnet, the vertical impedance is roughly 15 times larger. This is due mainly to the smaller half gap b and the longer magnet length L. Notice that the transverse impedance scales as L/b^3. The

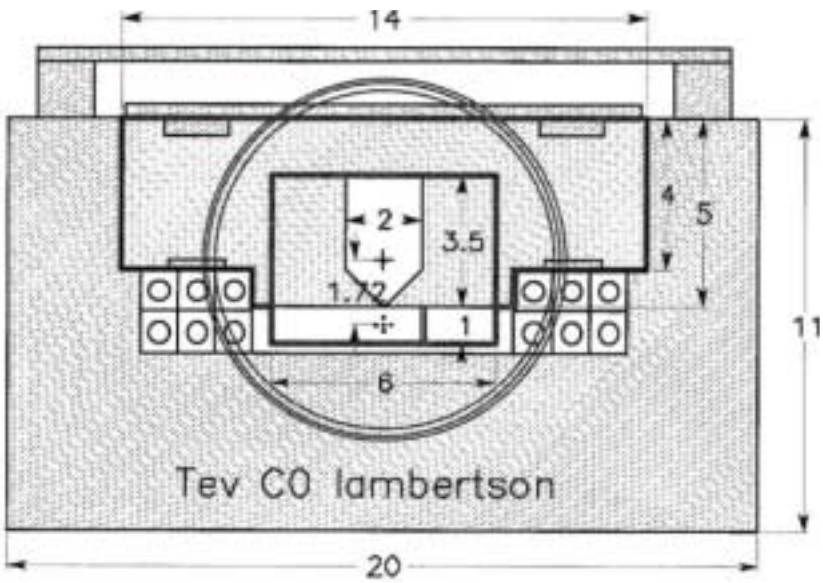

Figure 22: A cross-sectional drawing of the Lambertson magnet at Tevatron C0. The measurements are in inches.

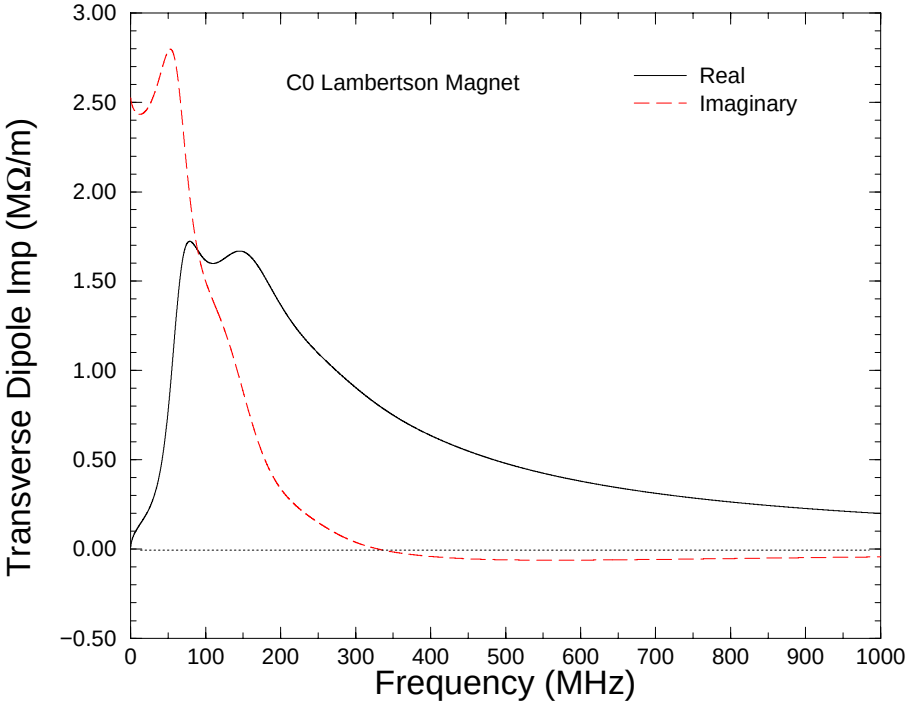

Figure 23: Vertical dipole impedance of a C0 Lambertson magnet with the particle beam circulating inside the 1″ high rectangular field region (see Fig. 22).

measured result of Crisp and Fellenz agrees with $\mathcal{I}m\, Z_1^V$ at zero frequency and $\mathcal{R}e\, Z_1^V$ at high frequencies. Again the computed $\mathcal{R}e\, Z_1^V$ of the broad peak near 100 and 200 MHz is about two times larger than the corresponding measurement.

4.2.2 Transverse Head-Tail Instabilities

Before the Fermilab shutdown in January of 2003, there were three C0 Lambertson magnets and 4 F0 Lambertson magnets. In addition the vacuum chamber, which is 6 cm by 6 cm square with rounded corner, also contributes a sizable amount of transverse impedance at low frequencies. Assuming the vacuum chamber to be made of stainless steel with resistivity 7.4×10^{-7} Ω-m, the wall impedance is found to be [18]

$$Z_1^V = [\mathrm{sgn}(\omega) + j]27.66|n + \nu_\beta|^{-1/2}\ \mathrm{M}\Omega/\mathrm{m}. \tag{4.17}$$

Including the resistive wall and the Lambertson magnets, the total vertical dipole impedance seen by the Tevatron beam is computed and its real and imaginary parts are shown in Fig. 24. Using the power spectra depicted in Fig. 16, the growth and damping rates for the head-tail modes $m = 0$, ±1, ±2, ±3, ±4, and ±5 in a Tevatron bunch of intensity $N_b = 2.6 \times 10^{11}$ at 150 GeV are computed as functions of chromaticity. The results are shown in Fig. 25, for rms bunch length $\sigma_\ell = 90$, 80, 70, and 60 cm. Only positive chromaticity is shown. The stability of the head-tail modes can be incurred in exactly the same way explained in the previous subsection. At the rms bunch length $\sigma_\ell = 90$ cm, mode $m = 0$ just has its positive- and negative-frequency parts of the power spectrum lying exactly on top of the broad resonances of $\mathcal{R}e\, Z_1^V$ at both positive and negative frequencies when the chromaticity is zero. Thus this mode remains stable when the chromaticity is increased or decreased slightly. However, modes $m = \pm4$ and ±5 have their positive- and negative-frequency parts of the power spectra farther apart and therefore become unstable when the chromaticity is shifted to positive. On the other hand, modes $m = \pm1$ and ±2 have their positive- and negative-frequency parts of the power spectra closer together and therefore become stable when the chromaticity is shifted to positive. When the bunch length becomes shorter, the bunch spectrum spreads out to higher frequencies. Thus positive- and negative-frequency parts of the power spectrum becomes relatively farther apart. Thus at $\sigma_\ell = 80$ cm, all modes $|m| \geq 3$ are unstable, while the lower modes are stable. When $\sigma_\ell = 60$ cm, modes $m = \pm2$ have their positive- and negative-frequency parts of the power spectrum lying exactly on top of the broad resonances of $\mathcal{R}e\, Z_1^V$ at both positive and negative frequencies when the chromaticity is zero. The mode is therefore just stable when the chromaticity changes slightly. The higher modes are unstable at positive chromaticity and the lower modes are stable.

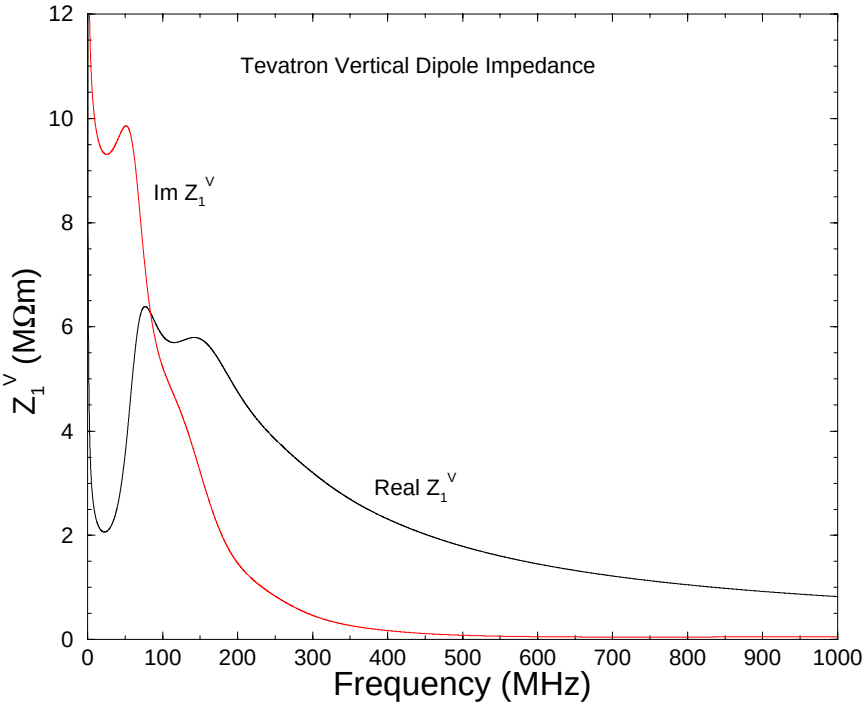

Figure 24: The real and imaginary parts of vertical dipole impedance experienced by a Tevatron beam before the shutdown in January 2003. Only the contributions of the resistive wall and the Lambertson magnets have been included. Here we see both the broadband contribution of the C0 magnets near 100 to 200 MHz and the the $\omega^{-1/2}$ contribution of the resistive wall at lower frequencies. Notice that the inductive behavior of the smooth vacuum chamber cancels the capacitive behavior of the Lambertson cracks at high frequencies.

At the bunch intensity of 2.6×10^{11}, the normalized rms emittance is $\epsilon_N = 3 \times 10^{-6}$ πm at the injection energy of 150 GeV and the rms bunch length has been $\sigma_\ell = 0.90$ cm. The linearized incoherent space-charge tune shift for a bunch with tri-Gaussian distribution is

$$\Delta\nu_{\rm spch}^{\rm max} = \frac{N_b r_p R}{2\sqrt{2\pi}\gamma^2\beta\epsilon_N\sigma_\ell} = -0.001158 \ . \tag{4.18}$$

On the other hand, the coherent tune shift of the head-tail mode $m = 0$ driven by the Lambertson magnets and the resistive-wall impedance is -0.73×10^{-3} at zero chromaticity and is much smaller for the higher-order head-tail modes, especially at large chromaticity. Thus the space-charge tune spread cannot supply any Landau damping to the growth of these modes. Tune spread for Landau damping must be supplied by sextupoles or octupoles, and must be of the order of the space-charge tune shift. The synchrotron tune is 0.0018 at the rf voltage of 1 kV. However, the azimuthal head-tail modes remain as good eigenmodes because modes $m = 0$ and -1 will not merge because while the wall impedance shifts the

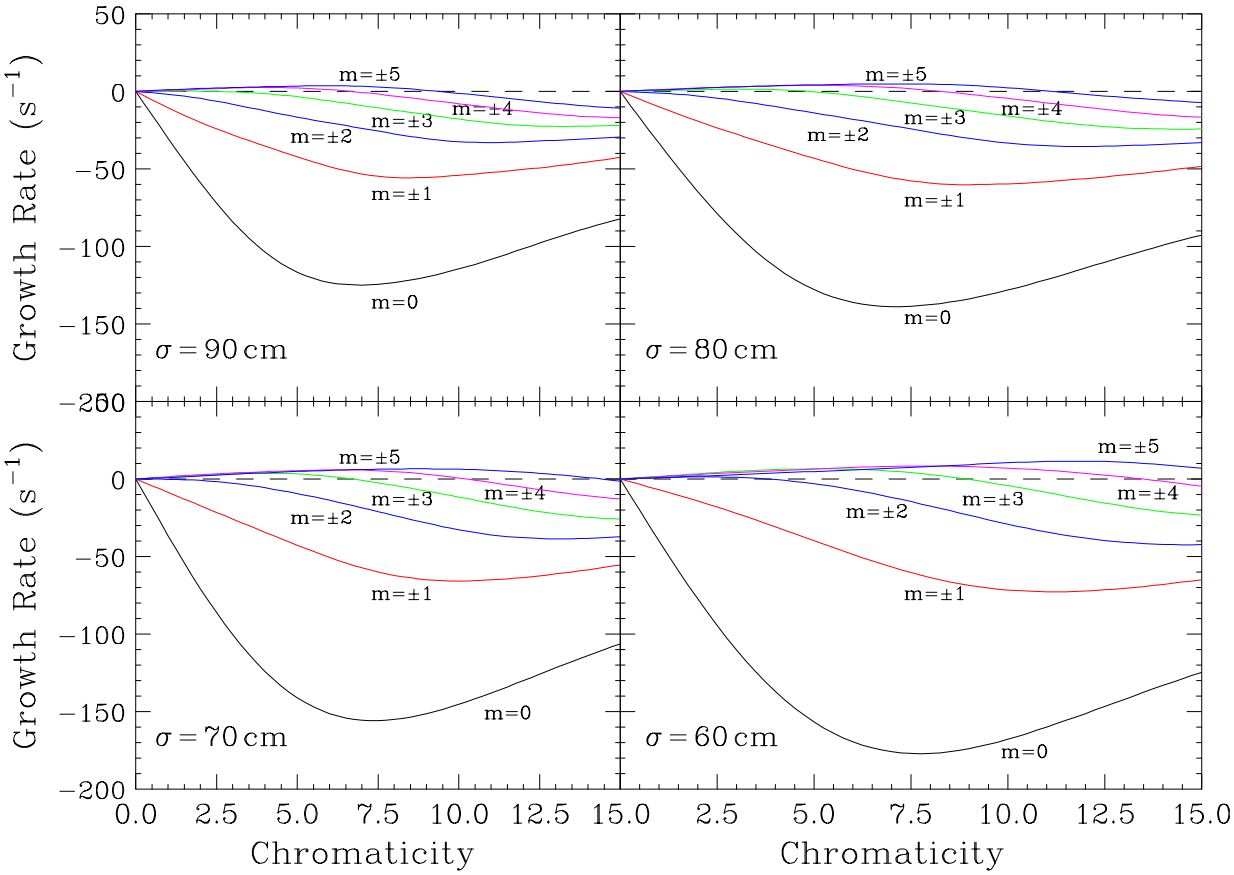

Figure 25: The growth and damping rates of head-tail modes $m = 0$, 1, 2, 3, 4, and 5 are shown as functions of chromaticity. The Tevatron bunch has an intensity of $N_b = 2.6 \times 10^{11}$ at the injection energy of 150 GeV. Various rms bunch lengths, 90, 80, 70, and 60 cm, have been assumed.

$m = 0$ mode downward, the transverse space-charge force shifts $m = -1$ mode downwards also. In fact, no transverse coupled-mode instability has ever been reported in the Tevatron.

4.2.3 Measurements by Invanov, Burov, and Tan

Before the January shutdown in 2003, the Tevatron did suffer from transverse single bunch instabilities, resulting in beam loss. Ivanov and Scarpine [21] made systematic measurement of the instabilities at various values of the vertical and horizontal chromaticities. The measurement data had been analyzed by Crisp [20], Alexahin et al [17], and Ivanov [19]. In one of the data, the vertical chromaticity was reduced to $\xi_y = -2$ to induce instability. The transverse displacement of the beam was monitored by a wideband 1-m long stripline beam-position monitor (BPM) in the Tevatron during proton injection for store 1841. Fig-

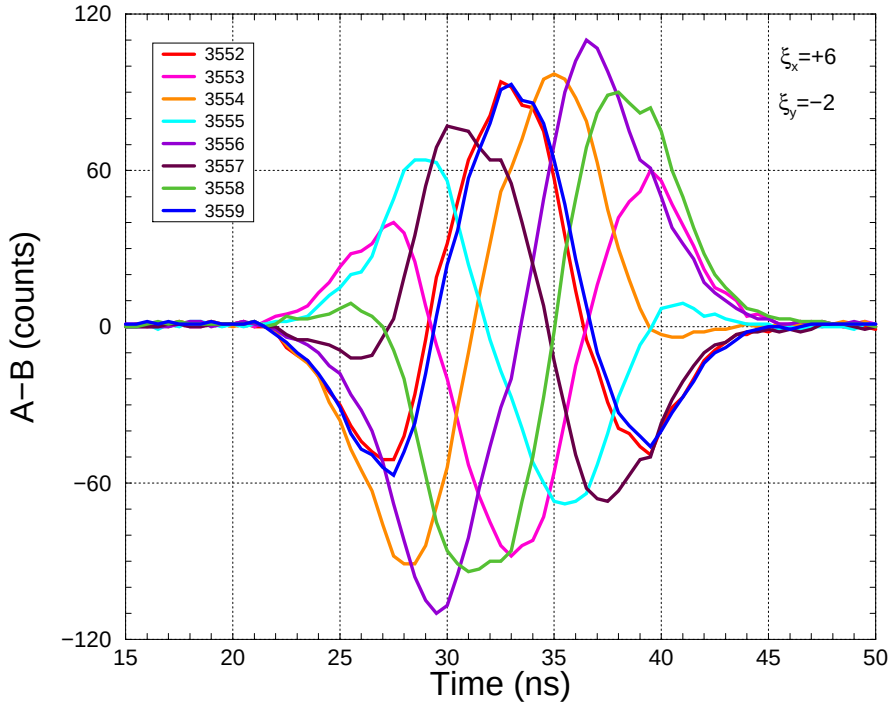

Figure 26: Difference signals registered at the Tevatron 1-m stripline beam-position monitors in 8 consecutive revolution turns. The signals reveal an unstable $m = 0$ head-tail mode. A contamination of the $m = \pm 1$ modes may also be present because of the left-right asymmetry of the signal envelope.

ure 26 shows 8 $A - B$ difference-signal traces in 8 consecutive turns. The striplines first register at the upstream termination the difference signal of the bunch as it crosses the upstream gap and then register the negative signal of the beam after it is reflected back from the downstream end. The time lag between the positive and negative signals is 6.7 ns. In other words, for a long beam ($\tau_L \gg 6.7$ ns), the stripline termination registers the derivative of the transverse beam displacement. Thus it is not easy to interpret the difference signal, especially when there is present a nonzero chromaticity. Viewed in a wideband capacitive pickup, the envelope of the difference signals exhibits m nodes for the head-tail mode m, independent of the chromaticity. This is illustrated in Fig. 27. Because of the differential nature of the stripline BPM, we should see no node for mode $m = 0$, 2 nodes for $m = \pm 1$, 3 nodes for $m = \pm 2$, etc. Thus definitely, the difference signals in Fig. 26 reveal the $m = 0$ mode. A closer examination reveals that the envelope is not exactly left-right antisymmetric,[§] with the right side going to zero less slowly than the left side. The asymmetry appears to

[§]The envelope of the signals is not left-right symmetric because the beam is not exactly equidistant from

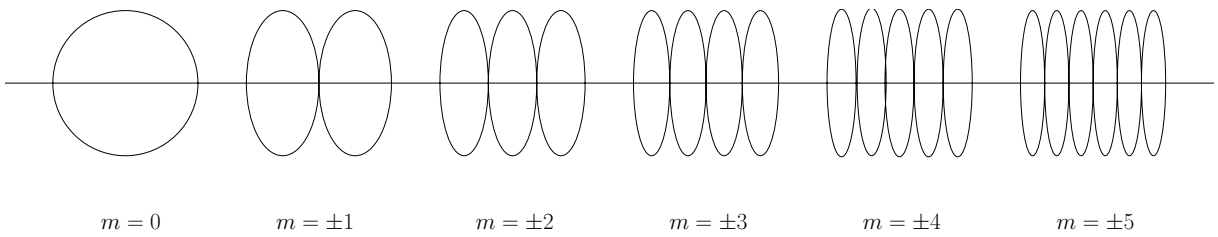

Figure 27: Plot showing the envelopes of vertical oscillation of head-tail modes $m = 0$ to ± 5 of a bunch, as registered in difference signals in a wideband capacitive pickup. We see that mode m has $|m|$ nodes along the longitudinal length.

be real, because the sum signals during these 8 consecutive turns do show an antisymmetry. An explanation will be the presence of more than one head-tail mode, because two head-tail modes evolve differently and they add up differently at different times. According to our analysis in Fig. 25, modes $m = \pm 1$ should be excited also. However, their growth rates are only about $\frac{1}{3}$ the growth rate of the $m = 0$ mode at chromaticity $\xi_y = -2$. Simulation shows that a 5 to 10% of the $m = \pm 1$ modes will produce the asymmetric signals in Fig. 26.

In the experiment of Ivanov, Burov, and Tan [21], the vertical chromaticity was lowered gradually to induce vertical instability. When the chromaticities were reduced from $\xi_x = 7.9$ and $\xi_y = 7.6$ to $\xi_x \sim \xi_y \sim 6$, the beam with an intensity of 2.6×10^{11} went unstable with about half the particles lost. The final beam with the intensity of 1.03×10^{11} had a stable longitudinal beam profile as depicted in the top-left plot of Fig. 28. The result is interpreted as follows. When the bunch became unstable, it oscillated vertically as head-tail modes $m = \pm 2$. As shown in Fig. 27, the envelope of this mode has 3 peaks, which got scraped as the instability developed. Because of the particles lost at the peaks, the final stable bunch exhibits 3 rings in the longitudinal phase space with deficient particle density, and this is the beam profile observed. The vertical chromaticity was further reduced to $\xi_y = -4.7$, the bunch was again unstable with a sizable beam loss. The beam intensity was reduced to 0.34×10^{11} before stability was established again. The new stable beam profile is shown in the top-right plot of Fig. 28. We can see particle density missing at the middle, implying that the instability excited belongs to the $m = 0$ mode. Similar experiment was repeated with a stable beam of intensity 2.65×10^{11}. When the chromaticities were reduced to $\xi_x \sim 6$ and $\xi_y \sim 3$, vertical instability occurred with very large amount of beam loss. The bunch regained stability when its intensity was reduced to 0.7×10^{11}. The beam profile, shown in the bottom plot of Fig. 28 exhibits particle deficiency at 4 locations, implying that the mode

the top and bottom striplines.

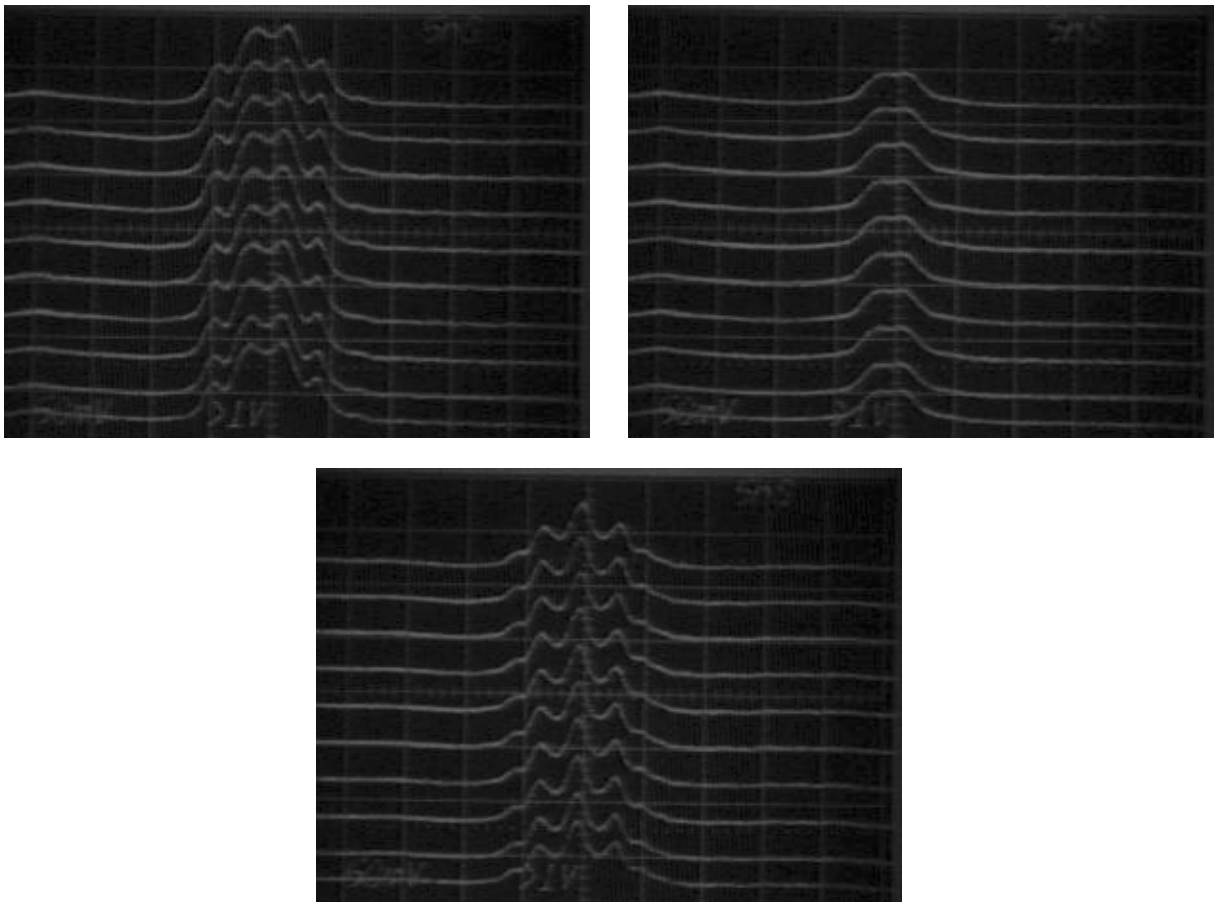

Figure 28: Longitudinal beam profiles of Tevatron bunch after undergoing a vertical instability accompanied by beam loss. Top-left: Chromaticities reduced to $\xi_x \sim \xi_y \sim 6$, and intensity reduced from 2.6×10^{11} to 1.03×10^{11}. Particle deficiency at the beam center and also at both sides indicates an excitation with 3 peaks or the $m = \pm 2$ modes. Top-right: Chromaticities reduced to $\xi_x = 5.8$, $\xi_y - 4.7$, and intensity reduced from 0.75×10^{11} to 0.34×10^{11}. Particle deficiency at the beam center only indicates an excitation with one peak or the $m = 0$ mode. Bottom: Chromaticities reduced to $\xi_x \sim 6, \xi_y \sim 2$ to 3, and intensity reduced from 2.65×10^{11} to 0.7×10^{11}. Particle deficiency at 4 locations along the beam but not at the center indicates an excitation of 4 peaks or the $m = \pm 3$ modes.

of excitation has 4 peaks. According to Fig. 27, this corresponds to the head-tail mode¶ $m = \pm 3$.

The C0 Lambertson magnets are no longer of any use because the Tevatron will not be operated in the fixed-target mode anymore. They were removed during the January 2003 shutdown. As was mentioned before, the transverse impedance dropped by a factor of ten. The transverse impedance was further reduced in the summer of 2003, when shielding liners were installed inside the F0 Lambertson magnets so that the beam would only be seeing the laminations partially. Now the Tevatron can be operated at rather low chromaticities without encountering the transverse head-tail instabilities.

4.3 FERMILAB MAIN INJECTOR

The Fermilab Main Injector does many jobs. It receives proton beams from the booster, accelerates them to 150 GeV, coalesces about 7 to 11 bunches into a super bunch to be injected into the Tevatron. Another job is to accelerate proton beams to 120 GeV to be extracted to hit a target for antiproton production. It also receives antiprotons from the Fermilab Antiproton Accumulator and accelerates them to 150 GeV, coalesces them into super bunches to be injected into the Tevatron. With the introduction of the Recycler Ring, antiprotons are transferred into the Recycler Ring for storage, accumulation, and cooling. When required, these antiprotons are transferred back into the Main Injector to be accelerated and to be injected into the Tevatron for collision. To accomplish all these jobs, there are many Lambertson magnets in the Main Injector. They are listed in Table IV. The Lambertson magnets at locations MI22 and MI32 that communicate with the Recycler Ring are made of permanent magnets and have a 3″ beam pipe through the field-free region. Since the beam does not see any laminations, they can be neglected in our discussion here. The old Main Ring Lambertson magnet at location MI20 is of length 2.4 m and we consider it as similar to the Tevatron F0 Lambertson magnet which is of length 2.8 m. Thus there are altogether 36.0 m of Tevatron F0 Lambertson magnets. The Main Injector beam pipe is of elliptical shape, 5.31 cm full height by 12.3 cm full width under vacuum, and made of stainless steel. The transverse dipole impedances are [22]

$$\begin{aligned} Z_1^V &= (1+j)17.3/\sqrt{n}\ \mathrm{M\Omega/m}\ , \\ Z_1^H &= (1+j)8.55/\sqrt{n}\ \mathrm{M\Omega/m}\ , \end{aligned} \tag{4.19}$$

Table IV: The Lambertson magnets in the Main Injector.

Location	Number	Type	Function
MI10	1	Old Main Ring	Injection of 8 GeV p from Booster
MI22	2	Permanent magnet	Extraction of 8 GeV $\bar{p}$ from MI to Recycler
MI32	2	Permanent magnet	Injection of 8 GeV $\bar{p}$ from Recycler to MI
MI40	3	Tevatron F0	p abort
MI52	3	Tevatron F0	120 GeV p to $\bar{p}$ production
			120 GeV p to switch yard
			150 GeV p to Tevatron
			Injection of 8 GeV $\bar{p}$ from Accumulator
			Injection of 150 GeV $\bar{p}$ from Tevatron
MI60	3	Tevatron F0	Extraction of 120 GeV p TO NuMI
MI62	3	Tevatron F0	Extraction of 150 GeV $\bar{p}$ to Tevatron

Notice that the Main Injector transverse impedance is only about one third that of the Tevatron. This is because the Main Injector contains only F0 Lambertson magnets but not C0 Lambertson magnet. We recall that the transverse impedance of a F0 Lambertson magnet is less than one tenth the transverse impedance of a C0 Lambertson magnet.

At injection, a 6×10^{10} proton bunch has a bunch area typically 0.1 eV-s. With a rf voltage of 1 MV, the synchrotron tune is $\nu_s = 5.47 \times 10^{-3}$. This gives a 95% half bunch length of 2.42 ns and a 95% half energy spread 13.2 MeV. Thus the spectra of the $m = \pm 1$ modes peak roughly at

$$f \sim \pm \frac{2}{2\tau_L} = \pm 206 \text{ MHz} , \tag{4.20}$$

according to the illustration in shown in Fig. 16. Thus all the higher modes $m = \pm 1, \ \pm 2, \ \pm 3, \ \cdots$ lie at frequencies higher than the broad resonance of the Main Injector vertical dipole impedance depicted in Fig. 29. A negative chromaticity shifts the rigid mode $m = 0$ to stability but leaves all the other modes unstable. For example the growth rates of the head-tail modes $m = \pm 1$ have the maxima of 31.7 s^{-1} when the chromaticity is near -7.0, as depicted in the top plot of Fig. 30

Assuming a tri-Gaussian distribution and a normalized 95% emittance of 20 πmm-mr, the maximum incoherent space-charge tune shift is, according to Eq. (4.18), $\Delta\nu_{\text{spch}}^{\text{max}} = -0.109$.

¶We do not understand why Ref. [21] addresses this mode as $m = \pm 1$.

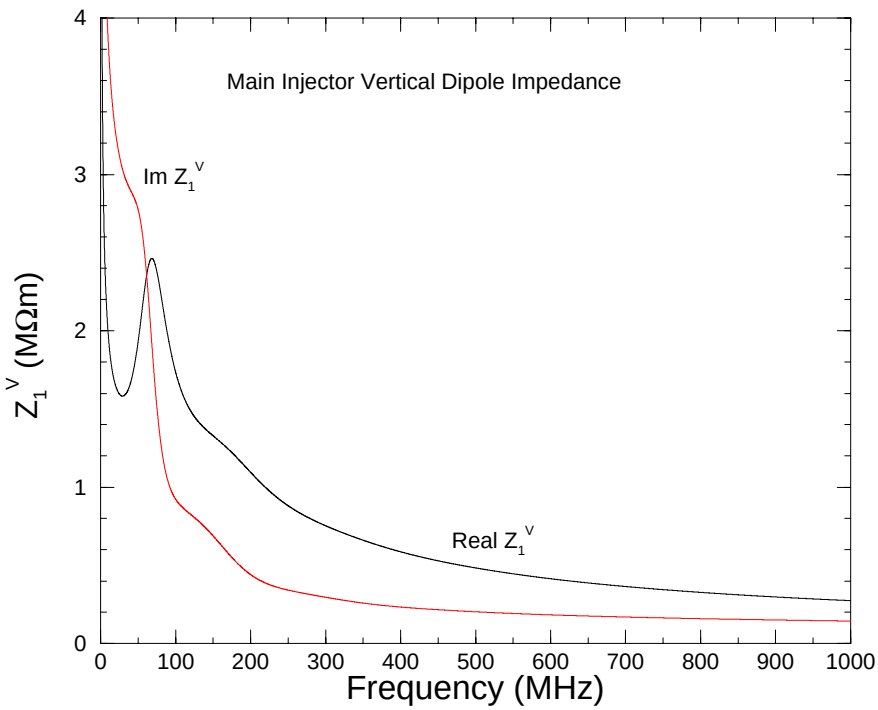

Figure 29: The real and imaginary parts of vertical dipole impedance experienced by a Main Injector beam. Only the contribution of the resistive wall and the Lambertson magnets have been included. Here we see both the broadband contribution of the Lambertson magnets near 100 to 200 MHz and the the $\omega^{-1/2}$ contribution of the resistive wall at lower frequencies.

The mean value is $\langle \Delta\nu_{\rm spch} \rangle = -0.069$ and the rms value is $\Delta\nu_{\rm spch}^{\rm rms} = 0.018$. On the other hand, the coherent tune shifts of modes $m = \pm 1$ are -0.0002. Thus, one needs a tune spread from sextupoles or octupoles of the order of 0.05 for Landau damping. Such large tune spreads are impractical. Luckily, the growth rates are small. If the negative chromaticity is further reduced to -2, the growth rates become only 13.3 $\rm s^{-1}$. The growth rates of the higher azimuthal modes are much smaller.

Slip-stacking is under study hoping to double the intensity of the proton bunches destined for antiproton production. [23] In order for two Booster bunches to fit within the momentum aperture of the Main Injector, the lowest rf voltage is desired. Experimental investigation has been performed with the rf voltage of 62 kV. At the bunch area of 0.1 eV-s, one bunch has a total width of $\tau_L = 10.54$ ns and half energy spread $\Delta E = 6.27$ MeV. At the time when two bunches slip-stack, the intensity becomes doubled at 12×10^{10} and the maximum incoherent space-charge tune shift is $\Delta\nu_{\rm spch}^{\rm max} = -0.168$. Again, it is impractical to compensate such large space-charge tune shift by sextupole- or octupole-generated tune

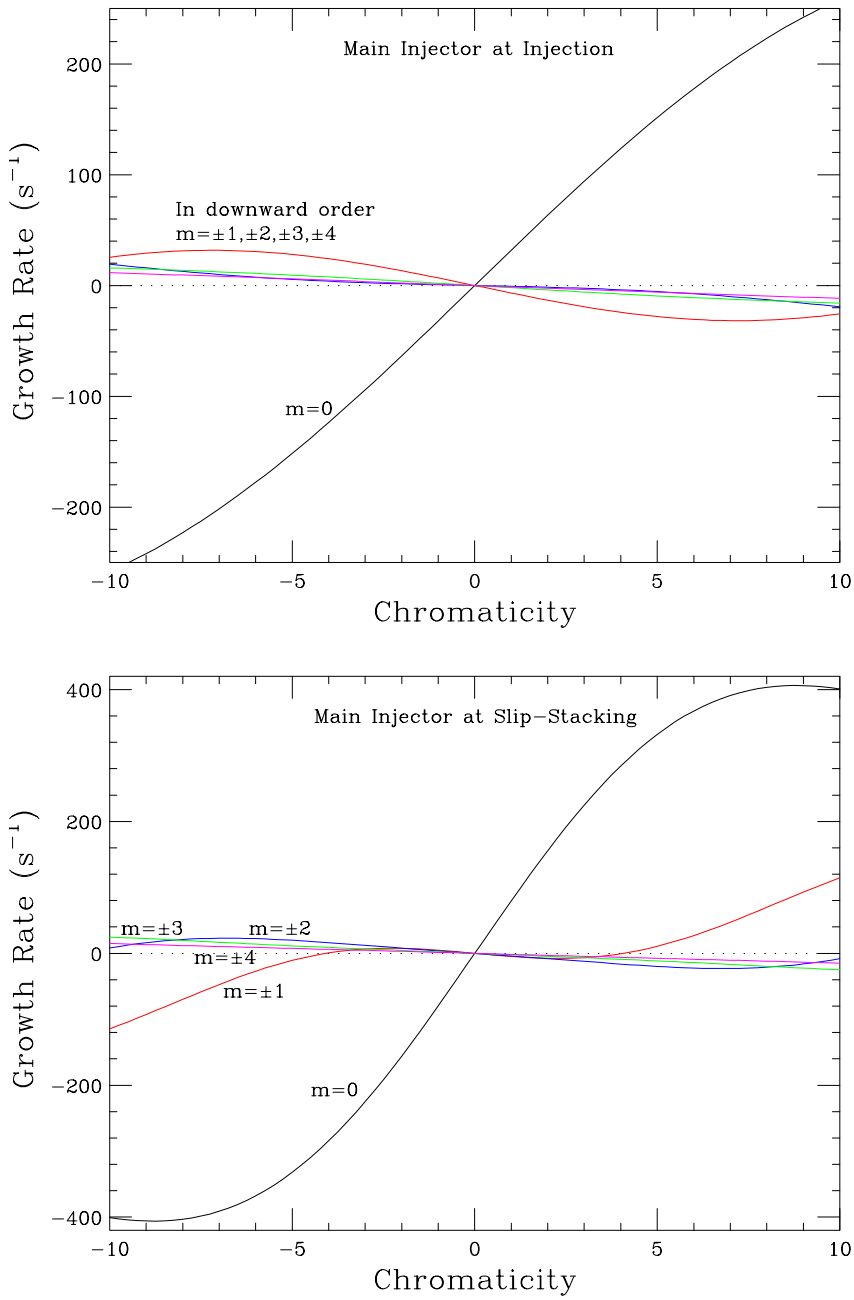

Figure 30: Top: Vertical head-tail growth rates are shown for the lower head-tail azimuthal modes $m = 0, \ \pm 1, \ \pm 2, \ , \pm 3$ of the Fermilab Main Injector bunches at the injection kinetic energy of 8 GeV as functions of chromaticity ξ, with 95% bunch area of 0.1 eV-s and rf voltage 1 MV. The driving force comes from the Lambertson magnets and the resistive wall impedance of the beam pipe. Bottom: The same for slip-stacking operation at rf voltage 62 kV.

spread in order to achieve Landau damping. Luckily, because of the long bunch length, mode $m = 0$ will be stable at negative chromaticity as depicted in the lower plot of Fig. 30, and, at the same time, the growth rates of the higher head-tail modes are slow. For example, modes $m = \pm 1$ have maximum growth rates of 7.6 s^{-1} at chromaticity $\xi = -2.5$, modes $m = \pm 2$ have maximum growth rates of 22.9 s^{-1} at chromaticity $\xi = -7.0$, modes $m = \pm 3$ have maximum growth rates of 25.9 s^{-1} at chromaticity $\xi = -11.5$, and modes $m = \pm 4$ have growth rates of 24.2 s^{-1} at chromaticity $\xi = -15.0$. If the negative chromaticity is set at a low value, say $\xi = -2$, the growth rates of modes $m = \pm 1$, $m = \pm 2$, $m = \pm 3$, and ± 4 are, respectively, 7.6, 7.9, 4.4, and 3.1 s^{-1}, which are quite tolerable.

5 CONCLUSIONS

We have derived the monopole and dipole impedances experienced by a beam inside a laminated magnet. The method consists of first deriving the resistive-wall impedances in terms of the surface impedance per square $\mathcal{R}$, which we define as the ratio of the longitudinal electric field to the transverse magnetic field at the surface. The surface impedance $\mathcal{R}$ is then derived by a weighted average of the surface impedance of the edges of the laminations and the impedance across the cracks between two adjacent laminations. We have considered two types of laminated magnets: the parallel-face magnets, which approximate the combined-function magnets of fast-ramping boosters, and the annular-ring magnets which approximate the Lambertson magnets. We are going to list some general properties of the impedance of a laminated magnet.

1. The crack surface impedance can be viewed as a capacitor in parallel with the series combination of a resistor plus an inductor. The impedance seen by the image current going up and down the laminations flanking a crack is represented by the resistor and the inductor. On the other hand, the image current can also jump across the crack as displacement current in just the same way as an ac current flowing across a capacitor. Thus the resistor and inductor dominate at low frequencies while the capacitor dominates at high frequencies. In between there are resonances when the depth of the crack, $(d - b)$, becomes an integral number of half-wavelengths. However, they are heavily damped by the conductivity of the laminations and the conductivity of the medium in the crack, so that usually only the first one or two are visible.

2. The dipole impedance of laminated magnet is very different from the monopole impedance. The beam current drives a differential dipole image current which sees an

inductive impedance because of the geometry of the system and is called the bypass inductance. In the presence of wall resistivity in the beam pipe or laminations of a magnet, what the beam sees is the bypass inductance in parallel with the surface impedance per square of the laminated magnet. At high frequencies, the beam, being difficult to flow through the bypass inductance, sees only the wall impedance. However, when the frequency is low enough, the beam is seeing the bypass inductance only and no real resistive part at all. The frequency at which the real part of the dipole impedance turns around to go to zero is important. For the smooth walls of a beam pipe, the bend-around frequency is usually much less than the revolution frequency and will not have any effect on the beam. For the large surface impedance per square of the laminated magnet, the bend-around frequency can be around 100 MHz. First, the laminated magnet will not contribute to the $\omega^{-1/2}$ behavior of the transverse dipole impedance at low frequencies that drives transverse coupled-bunch instabilities. Second, there will be a broadband dipole impedance near 100 MHz that drives transverse head-tail instabilities.

3. The surface impedance per square of a laminated magnet consists of the weighted average of the crack surface impedance $\mathcal{R}_c$ and the surface impedance $\mathcal{R}_L$ of the edges of the laminations. At high frequencies $\mathcal{R}_L$ dominates because it increases as $\omega^{1/2}$ due to the smaller skin-depth and the $\omega^{-1/4}$-roll-off of $\mathcal{R}_c$. However, $\mathcal{R}_L$ usually takes over at so high a frequency (~ 60 GHz) that we do not have any interest.

4. The behavior of the impedance for a laminated parallel-face magnet is very similar to that for a laminated annular magnet. However, with the same magnet opening $2b$ and the same depth of the cracks $(d-b)$, the impedance at low frequencies is usually much larger for parallel-face magnet than annular-ring magnet. This is because the image current flowing along the laminations fans out radially in the annular laminations and is therefore seeing a lower impedance. At high frequencies, there is no difference between the two models.

5. The impedance of a laminated magnet is independent of the crack width h at low frequencies but is proportional to the crack width at high frequencies. This is because at low frequencies the image current flows up and down the laminations flanking the cracks and the impedance is just proportional to the number of laminations. At high frequencies, however, the capacitive effect of the cracks dominates. The wider the cracks the smaller the capacitance and therefore the higher the impedance. This domination starts becoming obvious even at the first broad peak.

6. The conductivity of the medium in the crack has damping effect on the resonant peak. There is not much change if the conductivity is reduced further from $\sigma_{1c} = 1 \times 10^{-3}$ $(\Omega\text{-m})^{-1}$. However, if it is increased to 1×10^{-2} $(\Omega\text{-m})^{-1}$, the first broad peak will be damped by a factor of two and the second peak will hardly be visible. Further increase in σ_{1c} will have the resonant peaks damped out completely. The influence in the impedance at high frequencies and the $\omega^{1/2}$-low-frequency region is small.

7. The dielectric constant ϵ_{1r} of the medium in the crack increases the capacitance of the crack and therefore lowers the impedance at high frequencies. It was determined in Eq. (3.32) that the impedance should behave like $\epsilon_{1r}^{-1/2}$ at high frequencies. As expected, it does not affect the $\omega^{1/2}$-low-frequency region. However, its effect becomes important even at the first broad resonance.

8. The relative magnetic permeability μ_{2r} affects mostly the low-frequency behavior of the impedance because the image current goes around the laminations at a skin-depth. Thus $Z_0^{\parallel} \sim \mu_{1r}^{1/2}$ at low frequencies but does not perturb the high-frequency behavior by very much.

9. The higher the conductivity of the lamination σ_{2c}, the smaller the skin-depth and therefore the larger the impedance. Roughly speaking, $Z_0^{\parallel} \sim \sigma_{1c}^{1/2}$ at low frequencies but does not perturb the high-frequency behavior very much. As the conductivity increases, the resistivity of the laminations becomes less important and the cavity effect of the cracks dominates. For, example, when $\sigma_{2c} \gtrsim 10^{10}$ $(\Omega\text{-m})^{-1}$, the resonant effect of the cavity-like cracks becomes more evident according to $\tan q(d-b)$ when its argument is equal to odd multiples of $\pi/2$ for the parallel-face case or the zeroes of combination of Bessel function for the annular-ring case. The impedances will be small except at the resonances.

Applications have been made to the laminated magnets in Fermilab Booster, and the Lambertson magnets of the Tevatron and the Main Injector. Let us list some important features of the laminated magnets on the particle beam.

1. For a ring like the Fermilab Booster which consists of only laminated magnets, there will not be any $\omega^{-1/2}$-behaved transverse dipole impedance at low frequencies, because the bend-around frequency of $\mathcal{R}e\, Z_1^{\perp}$ is of the order of 100 MHz. In other words, there will not be any transverse coupled-bunch instabilities driven by the resistivity of

the laminated magnets. This explains why transverse coupled-bunch instabilities have never recorded in the Fermilab Booster, although they exist in nearly all accelerator rings.

2. The broadband transverse dipole impedance which occurs near 100 MHz is responsible for the transverse head-tail instabilities. Depending on how close the beam is from the laminations, this driving broadband impedance can be very large. An example is the former C0 Lambertson magnets of the Fermilab Tevatron.

3. The excitation of the transverse head-tail modes driven by the smooth resistive walls of a beam pipe is different from that driven by lamination magnets. In the former, if the rigid mode $m = 0$ is stable, all the higher modes will be unstable, if the chromaticity is slightly positive/negative above/below transition. For laminated magnets, whether the higher modes are stable or not depends on the length of the particle bunch. For example, if the bunch is long enough so that the power spectra of the $m = \pm 1$ modes are at lower frequency than the $\sim$ 100 MHz broadband impedance, these $m = \pm 1$ modes will be stable also. However, if the bunch is so short that the power spectrum is at higher frequency than the broadband impedance, these modes will be unstable.

References

[1] King-Yuen Ng, *Longitudinal and Transverse Coupling Impedances of the Extraction Lambertsons*, Fermilab Report UPC-149, 1980.

[2] A.W. Chao, *Physics of Collective Beam Instabilities in High Energy Accelerators*, John Wiley & Sons, 1993.

[3] L. Vos, *The Transverse Impedance of a Cylindrical Pipe with Arbitrary Surface Impedance*, CERN-AB-2003-005 ABP, 2003.

[4] The VLHC Design Study Group, *Design Study for a Staged VLHC*, Fermilab Report TM-2149, 2001.

[5] V. Lebedev, *Control of Transverse Multibunch Instabilities in the First Stage of the VLHC*, VLHC Mini-Workshop, SLAC, March 21-23, 2001.

[6] S.C. Snowdon, *Wave Propagation between Booster Laminations Induced by Longitudinal Motion of Beam*, Fermilab Report TM-277, 1970.

[7] R. Gluckstern, *Coupling Impedance and Energy Loss with Magnet Laminations*, Fermilab Report TM-1374, 1985.

[8] A.G. Ruggiero, *Energy Loss due to the Resistive Magnet Lamination in the NAL Booster*, Fermilab Report FN-230, 1971.

[9] R.E. Shafer, *Coupling Impedance of Laminated Magnets in the Booster*, Fermilab Report TM-1408, 1986.

[10] E. Keil and W. Schnell, CERN/ISR-TH/69-48, 1969; D. Boussard. CERN/PS-BI, 1972.

[11] Jim Crisp and Brian Fellenz, *Measured Longitudinal Beam Impedance of Booster Gradient Magnets*, Fermilab Report, TM-2145, 2001.

[12] A. Chao, *Topics in Accelerator Physics*, presented at US Particle Accelerator School, sponsored by UCLA, January, 2002, published as SLAC Report SLAC-PUB-9574, 2002, see also `http://www.slac.stanford.edu/~achao/`.

[13] M. Blaskiewicz, *Fast Head-Tail Instability with Space Charge*, Phys. Rev. ST Accel. Beams, 1, 044201 (1998).

[14] C. Ankenbrandt and S.D. Holmes, *Limits on the Transverse Phase Space Density in the Fermilab Booster*, Fermilab Report TM-1471, 1987.

[15] K.Y. Ng, *Distribution of Incoherent Space-Charge Tune Shift of beam of a Bi-Gaussian Beam*, Fermilab Report, TM-2241, 2004.

[16] Jim Crisp and Brian Fellenz, *Comparison of Tevatron C0 and F0 Lambertson Beam Impedance*, Fermilab Report, TM-2205, 2003.

[17] Yu. Alexahin, J. Annala, A. Burov, P. Ivanov, V. Shiltsev, T. Sen, and C.Y. Tan, *Tevatron Transverse Instability Studies*, Talk presented by P. Ivanov at the First Mid-West Accelerator Physics Collaboration Meeting, October 4-5, 2002, Fermilab.

[18] K.Y. Ng, *Impedances and Collective Instabilities of the Tevatron at Run II*, Fermilab Report TM-2055, 1998. The dipole impedance estimated in this report does not take into account the bypass inductance and is therefore incorrect.

[19] P. Ivanov, J. Annala, A. Burov, V. Lebedev, E. E.Lorman, V. Ranijbar, V. Scarpine, and V. Shiltsev, *Head-Tail Instability at Tevatron*, Proceedings of the 2003 Particle Accelerator Conference, Portland, Washington, 2003.

[20] James L. Crisp, *Tevatron Stripline Turn by Turn Data Showing Differential Head-Tail Positions*, Fermilab Report TM-2195, 2002.

[21] P. Ivanov, A. Burov, and C.Y. Tan, *Transverse Instability Studies at Low Chromaticities*, Tevatron Electronic Log Book, Fri. August 23, 2002, 054248.log.

[22] M.A. Martens and K.Y. Ng, *Impedance and Instability Threshold Estimate in the Main Injector*, Fermilab Report TM-1880, 1994. The dipole impedance estimated in this report does not take into account the bypass inductance and is therefore incorrect.

[23] K. Koba, et al, *Slip Stacking Experiments at Fermilab Main Injector*, Proc. of 2003 Particle Accelerator Conference, May 12-16, Portland, Washington, 2003.